AD-A091 310 AIR FORCE INST OF TECH WRIGHT-PATTERSON AFB OH F/G 20/12
THE MOBILITY, RESISTIVITY AND CARRIER DENSITY IN P-TYPE SILICON--ETC(U)
AUG 79 L C LINARES
UNCLASSIFIED AFIT-CI-79-232D NL

1 OF 2
AD
A091310

4

AD A091310

UNCLASS
SECURITY CLASSIFICATION OF THIS PAGE (*When Data Entered*)

①

REPORT DOCUMENTATION PAGE

READ INSTRUCTIONS
BEFORE COMPLETING FORM

1. REPORT NUMBER
79-232D

2. GOVT ACCESSION NO.
AD-A091 310

3. RECIPIENT'S CATALOG NUMBER

4. TITLE (*and Subtitle*)
(6) The Mobility, Resistivity and Carrier Density in p-Type Silicon Doped with Boron, Gallium and Indium.

5. TYPE OF REPORT & PERIOD COVERED
Dissertation

6. PERFORMING ORG. REPORT NUMBER

7. AUTHOR(*s*)
(10) Luis Carlos/Linares (11) Aug 79

8. CONTRACT OR GRANT NUMBER(*s*)
(12) 177

9. PERFORMING ORGANIZATION NAME AND ADDRESS
AFIT STUDENT AT: University of Florida (9) Doctoral thesis

10. PROGRAM ELEMENT, PROJECT, TASK AREA & WORK UNIT NUMBERS

11. CONTROLLING OFFICE NAME AND ADDRESS
AFIT/NR (14) AFIT-CI-79-232D
WPAFB OH 45433

12. REPORT DATE
Aug 1979

13. NUMBER OF PAGES
148

14. MONITORING AGENCY NAME & ADDRESS (*if different from Controlling Office*)

LEVEL II

15. SECURITY CLASS. (*of this report*)
UNCLASS

15a. DECLASSIFICATION/DOWNGRADING SCHEDULE

16. DISTRIBUTION STATEMENT (*of this Report*)

APPROVED FOR PUBLIC RELEASE; DISTRIBUTION UNLIMITED

DTIC
ELECTE
NOV 6 1980
S C

17. DISTRIBUTION STATEMENT (*of the abstract entered in Block 20, if different from Report*)

18. SUPPLEMENTARY NOTES

APPROVED FOR PUBLIC RELEASE: IAW AFR 190-17
25 SEP 1980

Fredric C. Lynch
FREDRIC C. LYNCH, Major, USAF
Director of Public Affairs
Air Force Institute of Technology (ATC)
Wright-Patterson AFB, OH 45433

19. KEY WORDS (*Continue on reverse side if necessary and identify by block number*)

20. ABSTRACT (*Continue on reverse side if necessary and identify by block number*)

ATTACHED

DDC FILE COPY

DD FORM 1 JAN 73 1473 EDITION OF 1 NOV 65 IS OBSOLETE

UNCLASS 012200
SECURITY CLASSIFICATION OF THIS PAGE (*When Data Entered*)

Abstract of Dissertation Presented to the Graduate Council
of the University of Florida in Partial Fulfillment of the Requirements
for the Degree of Doctor of Philosophy

THE MOBILITY, RESISTIVITY AND CARRIER DENSITY IN p-TYPE SILICON DOPED WITH BORON, GALLIUM AND INDIUM

By

Luis Carlos Linares

August 1979

Chairman: Sheng-San Li
Major Department: Electrical Engineering

Using the relaxation time approximation and a three-band model (i.e., nonparabolic light-hole band, parabolic heavy-hole and split-off bands), a derivation involving the use of the Boltzmann transport theory was applied to obtain expressions for the valence band density-of-states effective mass, m_D^*, the valence band conductivity effective mass, m_C^*, and the valence band Hall effective mass, m_H^*, of holes in p-type silicon. Values of effective mass calculated from this model reveal the temperature and dopant density dependence of the effective mass due to the nonparabolic shape of the bands. With these values of effective mass and the three-band model, theoretical calculations of hole mobility, resistivity, Hall factor and Hall mobility were conducted for p-type silicon doped with boron, gallium and indium for dopant densities from 10^{14} to 10^{18} cm^{-3} and temperatures between 100 and 400 K. Scattering contributions from acoustical and optical phonons, and ionized and neutral impurities were considered. In addition, interband scattering

for the case of acoustical phonons, the effect of hole-hole scattering on the various scattering mechanisms, and the nonparabolicity of the valence band were also taken into account in the calculations. The valence band density-of-states effective mass, m_D^*, was found to vary from 0.6567 m_o at 100 K to 0.8265 m_o at 400 K, while the valence band conductivity effective mass, m_C^*, increased from a value of 0.3604 m_o at 100 K to a value of 0.4910 m_o at 400 K. The valence band Hall effective mass, m_H^*, varies from 0.2850 m_o at 100 K to 0.5273 m_o at 400 K. The masses m_D^* and m_C^* showed little change with dopant density, but m_H^* varied by as much as 63 percent at 100 K over the range of dopant densities considered. The Hall factor was expressed in terms of a mass anisotropy factor and a scattering factor. These two components of the Hall factor were separately evaluated to emphasize their individual contributions to the Hall factor. Theoretical values of the Hall factor vary between 1.73 and 0.77 over the dopant density and temperature ranges.

To verify our theoretical calculations, resistivity and Hall coefficient measurements were performed on silicon samples doped with boron, gallium and indium with dopant densities ranging from 4.25×10^{15} to 9.07×10^{17} cm^{-3}, for $100 \leq T \leq 400$ K, using planar square array test structures. Agreement between the calculated and measured resistivity values was within 10 percent over the range of temperatures and dopant density studied. Agreement between our calculated and experimental values of Hall mobility was within 15 percent for temperatures greater than 150 K. At 300 K, agreement between theoretical values of Hall factor and those deduced from experimental data of this work and that of other studies was within 15 percent for dopant densities greater than 5×10^{16} cm^{-3}. From the results of this study, we conclude that the theoretical model and expressions developed here can accurately describe the mobility and resistivity in p-type silicon. The omission of band anisotropy considerations, however, introduces considerable error in the evaluation of the Hall factor for low dopant densities.

79-232D

Abstract of Dissertation Presented to the Graduate Council
of the University of Florida in Partial Fulfillment of the Requirements
for the Degree of Doctor of Philosophy

THE MOBILITY, RESISTIVITY AND CARRIER DENSITY IN p-TYPE SILICON DOPED WITH BORON, GALLIUM AND INDIUM

By

Luis Carlos Linares

August 1979

Chairman: Sheng-San Li
Major Department: Electrical Engineering

Using the relaxation time approximation and a three-band model (i.e., nonparabolic light-hole band, parabolic heavy-hole and split-off bands), a derivation involving the use of the Boltzmann transport theory was applied to obtain expressions for the valence band density-of-states effective mass, m_D^*, the valence band conductivity effective mass, m_C^*, and the valence band Hall effective mass, m_H^*, of holes in p-type silicon. Values of effective mass calculated from this model reveal the temperature and dopant density dependence of the effective mass due to the nonparabolic shape of the bands. With these values of effective mass and the three-band model, theoretical calculations of hole mobility, resistivity, Hall factor and Hall mobility were conducted for p-type silicon doped with boron, gallium and indium for dopant densities from 10^{14} to 10^{18} cm^{-3} and temperatures between 100 and 400 K. Scattering contributions from acoustical and optical phonons, and ionized and neutral impurities were considered. In addition, interband scattering

for the case of acoustical phonons, the effect of hole-hole scattering on the various scattering mechanisms, and the nonparabolicity of the valence band were also taken into account in the calculations. The valence band density-of-states effective mass, m_D^*, was found to vary from 0.6567 m_o at 100 K to 0.8265 m_o at 400 K, while the valence band conductivity effective mass, m_C^*, increased from a value of 0.3604 m_o at 100 K to a value of 0.4910 m_o at 400 K. The valence band Hall effective mass, m_H^*, varies from 0.2850 m_o at 100 K to 0.5273 m_o at 400 K. The masses m_D^* and m_C^* showed little change with dopant density, but m_H^* varied by as much as 63 percent at 100 K over the range of dopant densities considered. The Hall factor was expressed in terms of a mass anisotropy factor and a scattering factor. These two components of the Hall factor were separately evaluated to emphasize their individual contributions to the Hall factor. Theoretical values of the Hall factor vary between 1.73 and 0.77 over the dopant density and temperature ranges.

To verify our theoretical calculations, resistivity and Hall coefficient measurements were performed on silicon samples doped with boron, gallium and indium with dopant densities ranging from 4.25×10^{15} to 9.07×10^{17} cm^{-3}, for $100 \le T \le 400$ K, using planar square array test structures. Agreement between the calculated and measured resistivity values was within 10 percent over the range of temperatures and dopant density studied. Agreement between our calculated and experimental values of Hall mobility was within 15 percent for temperatures greater than 150 K. At 300 K, agreement between theoretical values of Hall factor and those deduced from experimental data of this work and that of other studies was within 15 percent for dopant densities greater than 5×10^{16} cm^{-3}. From the results of this study, we conclude that the theoretical model and expressions developed here can accurately describe the mobility and resistivity in p-type silicon. The omission of band anisotropy considerations, however, introduces considerable error in the evaluation of the Hall factor for low dopant densities.

THE MOBILITY, RESISTIVITY AND CARRIER DENSITY IN p-TYPE SILICON DOPED WITH BORON, GALLIUM AND INDIUM

By

LUIS CARLOS LINARES

A DISSERTATION PRESENTED TO THE GRADUATE COUNCIL OF
THE UNIVERSITY OF FLORIDA
IN PARTIAL FULFILLMENT OF THE REQUIREMENTS FOR THE
DEGREE OF DOCTOR OF PHILOSOPHY

UNIVERSITY OF FLORIDA

1979

TO MY FAMILY

FOR THEIR PATIENT SUPPORT

ACKNOWLEDGMENTS

I gratefully express my appreciation to the members of my supervisory committee for their support and cooperation. In particular, I thank Dr. S. S. Li for his guidance, enthusiasm and professional example, and Dr. F. A. Lindholm for his continuing interest in the research. A special expression of appreciation is due Dr. A. D. Sutherland for his advice and support during the first year of my graduate work.

I am also indebted to D. Yuen for his help with measurements on the gallium- and indium-doped samples, to M. Riley for the fabrication and measurement of the boron samples, and to W. Axson and R. Wilfinger for their invaluable help with various laboratory procedures.

This investigation was made possible by the Air Force Institute of Technology. The research was jointly supported by the National Bureau of Standards Contract No. 7-35741 and the National Science Foundation Grant No. ENG 76-81828.

TABLE OF CONTENTS

APPENDIX

LIST OF FIGURES

KEY TO SYMBOLS

A	Inverse mass band parameter
A'	Area of the base-collector diode
a	Defformation potential constant (acoustic phonon scattering)
B	Inverse mass band parameter
b	Defformation potential constant (optical phonon scattering)
C	Inverse mass band parameter
C_ℓ	Longitudinal sound velocity in silicon
C_t	Transverse sound velocity in silicon
E	Energy of holes
e	Magnitude of the electronic charge
E_A	Acceptor impurity energy level
E_F	Fermi energy level
E_V	Valence band edge
E_1	Binding energy of neutral acceptors
f_o	The Fermi-Dirac function
$F_{½}$	Fermi-Dirac integral of order 1/2
g	Ground state degeneracy
$\hbar$	Plank's constant divided by 2π
I	Current
J	Current density
$\bar{k}$	Wave vector
k_o	Boltzmann's constant

m_1	Heavy-hole mass at 4.2 K
m_2	Light-hole mass at 4.2 K
m_C^*	Conductivity effective mass in the combined band
m_{Ci}^*	Conductivity effective mass in band i
m_D^*	Density-of-state effective mass in the combined band
m_{Di}^*	Density-of-state effective mass in band i
m_G^*	Geometric mean mass
m_H^*	Hall effective mass in the combined band
m_{Hi}^*	Hall effective mass in band i
N_A	Total acceptor impurity density
N_A^-	Ionized acceptor impurity density
N_N	Neutral impurity density
n_o	Phonon distribution function
N_V	Effective density of valence band states
p_i	Hole density in band i
p'	Effective screening hole density
r_{Ai}	Mass anisotropy factor in band i
R_H	Hall coefficient in the combined band
r_H	The Hall factor in the combined band
R_{Hi}	Hall coefficient in band i
r_{Hi}	The Hall factor in band i
r_{Si}	Scattering factor in band i
S	Probe spacing
T	Absolute temperature
V	Voltage
V_H	Hall voltage

w	Thickness of the chip
β	Ratio of defformation potential constants
γ	Function of band mass parameters
γ_{ij}	Ratio of density-of-state effective masses
γ_{hh}^{a}	Hole-hole reduction factor for acoustic phonon scattering
γ_{hh}^{i}	Hole-hole reduction factor for ionized impurity scattering
γ_{hh}^{o}	Hole-hole reduction factor for optical phonon scattering
Δ	Energy of spin orbit splitting
ε	Reduced energy (E/k_0T)
ε_1	Variable of integration
ε_2	Variable of integration
ε_s	Relative dielectric constant
ζ	Limit of integration
η	Reduced Fermi-energy
η_1	Scaling factor
θ	Spherical coordinate
θ_D	Debye temperature
μ_C	Conductivity mobility in the combined band
μ_{Ci}	Conductivity mobility in band i
μ_H	Hall mobility in the combined band
ξ	Limit of integration defined in Figure 2.1
ρ	Resistivity of holes
ρ_s	Density of silicon
σ_C	Electrical conductivity
σ_H	Hall conductivity
τ	Total scattering relaxation time
τ_{aci}	Acoustic phonon scattering relaxation time in band i

τ_{Ii}	Ionized impurity scattering relaxation time in band i
τ_{ij}	Total interband scattering relaxation time
τ_{ii}	Total intraband scattering relaxation time
τ_{Ni}	Neutral impurity scattering relaxation time in band i
τ_{oi}	Optical phonon scattering relaxation time in band i
τ_{x}	Adjustable scattering constant
ϕ	Spherical coordinate

Abstract of Dissertation Presented to the Graduate Council
of the University of Florida in Partial Fulfillment of the Requirements
for the Degree of Doctor of Philosophy

THE MOBILITY, RESISTIVITY AND CARRIER DENSITY IN p-TYPE SILICON DOPED WITH BORON, GALLIUM AND INDIUM

By

Luis Carlos Linares

August 1979

Chairman: Sheng-San Li
Major Department: Electrical Engineering

Using the relaxation time approximation and a three-band model (i.e., nonparabolic light-hole band, parabolic heavy-hole and split-off bands), a derivation involving the use of the Boltzmann transport theory was applied to obtain expressions for the valence band density-of-states effective mass, m_D^*, the valence band conductivity effective mass, m_C^*, and the valence band Hall effective mass, m_H^*, of holes in p-type silicon. Values of effective mass calculated from this model reveal the temperature and dopant density dependence of the effective mass due to the nonparabolic shape of the bands. With these values of effective mass and the three-band model, theoretical calculations of hole mobility, resistivity, Hall factor and Hall mobility were conducted for p-type silicon doped with boron, gallium and indium for dopant densities from 10^{14} to 10^{18} cm^{-3} and temperatures between 100 and 400 K. Scattering contributions from acoustical and optical phonons, and ionized and neutral impurities were considered. In addition, interband scattering

for the case of acoustical phonons, the effect of hole-hole scattering on the various scattering mechanisms, and the nonparabolicity of the valence band were also taken into account in the calculations. The valence band density-of-states effective mass, m_D^*, was found to vary from 0.6567 m_o at 100 K to 0.8265 m_o at 400 K, while the valence band conductivity effective mass, m_C^*, increased from a value of 0.3604 m_o at 100 K to a value of 0.4910 m_o at 400 K. The valence band Hall effective mass, m_H^*, varies from 0.2850 m_o at 100 K to 0.5273 m_o at 400 K. The masses m_D^* and m_C^* showed little change with dopant density, but m_H^* varied by as much as 63 percent at 100 K over the range of dopant densities considered. The Hall factor was expressed in terms of a mass anisotropy factor and a scattering factor. These two components of the Hall factor were separately evaluated to emphasize their individual contributions to the Hall factor. Theoretical values of the Hall factor vary between 1.73 and 0.77 over the dopant density and temperature ranges.

To verify our theoretical calculations, resistivity and Hall coefficient measurements were performed on silicon samples doped with boron, gallium and indium with dopant densities ranging from 4.25×10^{15} to 9.07×10^{17} cm^{-3}, for $100 \leq T \leq 400$ K, using planar square array test structures. Agreement between the calculated and measured resistivity values was within 10 percent over the range of temperatures and dopant density studied. Agreement between our calculated and experimental values of Hall mobility was within 15 percent for temperatures greater than 150 K. At 300 K, agreement between theoretical values of Hall factor and those deduced from experimental data of this work and that of other studies was within 15 percent for dopant densities greater than 5×10^{16} cm^{-3}. From the results of this study, we conclude that the theoretical model and expressions developed here can accurately describe the mobility and resistivity in p-type silicon. The omission of band anisotropy considerations, however, introduces considerable error in the evaluation of the Hall factor for low dopant densities.

CHAPTER I

INTRODUCTION

The goal of this study has been to measure and compare with theory the resistivity and Hall mobility of holes in silicon doped with gallium and indium as functions of temperature and dopant density. Data taken on boron-doped silicon was also included in order to further confirm the adequacy of the theoretical model. In order to determine theoretically the resistivity and Hall mobility, one must first calculate the conductivity mobility, the density of holes, and the Hall factor. This can only be done with a thorough understanding of the energy band structure, the scattering mechanisms involved, and the carrier statistics.

The application of an electric or a magnetic field to a crystal results in a variety of carrier transport phenomena. These phenomena are associated with the motion of current carriers in the conduction or valence bands. The free charge carriers in a semiconductor will acquire a drift velocity under the influence of an applied electric field. This velocity is the net result of the momentum gained from the externally applied field, and the momentum lost in collisions which tend to randomize the carrier momentum [1]. If the field is expressed in volts per centimeter, and the velocity in centimeters per second, a mobility is defined as the incremental average speed per unit electric field, and is expressed in squared centimeters per volt second. The velocity, and consequently the mobility, is determined by the different types of collisions which the carriers undergo. Collisions of carriers with lattice atoms which are out of their equilibrium positions because of thermal vibration, provide an upper limit to the mobility. Scattering of the carriers is also caused by impurities, both ionized and neutral. At high temperatures and low dopant densities, scattering by lattice phonons is more effective while at low temperatures and high impurity densities, scattering by ionized and neutral impurities predominates. In addition, the effects of hole-hole scattering on the lattice and ionized impurity scattering mechanisms need to be considered. Thus in calculating the mobility over a wide range of temperatures and dopant densities, all the different scattering mechanisms must be taken into account. Besides the mobility, the density of holes enters the problem of determining the electrical resistivity. The density of holes associated with dopant atoms is a function of the ionization energy of the dopant atom, the temperature, and the degeneracy factor. Calculation of the Hall mobility requires knowledge of the Hall factor which is a function of the scattering mechanisms and effective masses.

For purposes of device design it is necessary to know the correct relationship between the resistivity and dopant density at different temperatures. Evaluation of the characteristics of semiconductor devices and the study of transport phenomena in semiconductors requires an accurate knowledge of variations in the effective mass, mobility, and carrier density with changes in temperature and dopant density. Because of this, numerous studies of mobility, resistivity, and hole density in p-type silicon have been conducted [1-16]. However, due to the complexity of the valence band of silicon and the various scattering mechanisms involved, these studies, for the most part, have either been conducted in temperature and dopant density ranges designed to explore only a particular type of scattering mechanism, or have not advanced the theory necessary to describe the experimental result. For example, Costato and Reggiani [4] calculated the mobility of holes for pure p-type silicon in which lattice scattering dominates; Braggins [1] considered nonparabolicity and all the relevant scattering mechanisms with the exception of hole-hole scattering, but he limited his investigation to dopant densities below 5×10^{16} cm^{-3} and low temperatures; Morin and Maita [5] considered wide ranges of temperature and dopant densities, but did not provide a theoretical examination of the data. Recently, Li [17] developed a theoretical model capable of describing the mobility and resistivity of p-type silicon over a wide range of temperatures and dopant densities. This improved model was applied to the case of boron-doped silicon with great success [17]. The improvement in the theory consisted mainly of the inclusion of hole-hole scattering effects, and consideration of the nonparabolic nature of the bands. In this study, Li's model [17] has been improved by including consideration of interband scattering effects on the acoustic phonon scattering mechanism, and has been applied to the study of silicon doped with impurities other than boron.

With some exceptions [14-16], most of the research in p-type silicon has been conducted with boron as the doping impurity, since boron is the shallowest acceptor in silicon and this material is widely available. A very limited amount of data is available on silicon doped with deeper impurities such as gallium and indium. These dopants, especially indium, are of great interest to modern technology because of their application to photo-detector devices. Curves of resistivity and mobility as functions of dopant density [2,3] have been applied to characterizing boron-doped starting material and diffused boron layers in silicon, and have been found highly useful. Similar curves developed in this research may be expected to be equally useful for characterizing and integrating infrared detectors based on the deeper levels of indium and gallium with on-chip silicon electronics. Application of a more complete theory of mobility and resistivity [17] to the case of silicon doped with gallium and indium should provide an accurate description of the transport of holes in this material. These results may be of significant use in the study and design of infrared photo-detector devices.

In this research the mobility, resistivity, and hole density have been studied over a temperature range from 100 to 400 K and dopant densities from 4.25×10^{15} to 9.05×10^{17} cm^{-3}. Because of the complexity brought about by heavy doping effects and uncertainties in accounting for hole density and impurity density at high dopant densities, the theoretical analysis has been restricted to densities below 10^{18} cm^{-3} in which the use of Boltzmann statistics is justified. The nonparabolic nature of the valence band structure, and derivation of expressions for the temperature dependent effective masses are presented in Chapter II. Since effective mass is directly related to the shape of the valence bands, the result is an effective mass which varies with temperature and dopant density. The mobility formulation includes consideration of the relevant scattering mechanisms and how these are modified by hole-hole scattering effects. These scattering mechanisms are considered in detail in Chapter III. Since the different scattering mechanisms which contribute to the mobility have different temperature and energy dependences, the use of numerical methods and curve fitting has been applied in analyzing the data. The temperature and dopant density dependence of resistivity and hole density is analyzed in Chapter IV. In Chapter V, the Hall factor is discussed, and theoretical calculations of Hall mobility are presented. Fabrication techniques and experimental procedures are described in Chapter VI. Comparisons of experimental results with predictions based on the theory of Chapters III through V are made in Chapter VII; in this chapter the theoretical results are also compared with data published by other workers. Chapter VIII summarizes the research and states the main conclusions derived from this work.

CHAPTER II

BAND STRUCTURE AND EFFECTIVE MASS

2.1 Introduction

The interpretation of transport properties in silicon and the modeling of silicon junction devices depend on an accurate knowledge of values of effective mass. The complex valence band structure of silicon leads to difficulties in the study of transport properties of holes in this material. Thus the development of a model incorporating the nonparabolic nature of the band into a single parameter, the combined hole effective mass, would greatly simplify the study of mobility, resistivity, and the Hall effect in silicon. Including the band nonparabolicity in calculations of relaxation time via the effective mass formulation is a reasonable procedure and has been applied effectively by Radcliffe [18] to study acoustic phonon scattering, and by Barrie [19] to study optical phonon and impurity scattering in nonparabolic bands. In this chapter we will derive such a theoretical model for hole effective mass calculations in silicon.

Lax and Mavroides [20] have derived expressions for density-of-states effective masses m^*_{D1} and m^*_{D2} for the heavy-hole band and the light-hole band, respectively, which lead to the generally accepted and quoted value, $m^*_D = 0.591\ m_o$. This value, however, can only be considered applicable at 4.2 K, where $m^*_1 = 0.537\ m_o$ and $m^*_2 = 0.153\ m_o$. A number of experimental data has been published which indicates both electron and hole effective mass to be dependent both on temperature and dopant density [21,22]. Below 50 K, hole effective mass remains constant as indicated in high frequency magnetoconductivity experiments [23]. However, at higher temperatures and for higher acceptor impurity densities, two mechanisms are responsible for the temperature dependence of the effective mass: the thermal expansion of the lattice, and the explicit effect of temperature. The effect of the thermal expansion can be estimated from the stress dependence of the effective mass [24], and has been shown to be negligible [21,25]. The explicit temperature effect however, is of great importance. It consists of three parts: (a) the temperature variation of the Fermi distribution function in a nonparabolic band, (b) the temperature dependent distribution function of the split-off band, and (c) the temperature variation of the curvature at the band extremum due to the interaction between holes and lattice phonons.

Following the work of Lax and Mavroides [20], but using Fermi-Dirac statistics and a simplified model of the valence band structure for silicon, Barber [25] obtained an expression for the density-of-states effective mass, m_D^*, which is temperature and hole-density dependent. Barber, however, did not apply the nonparabolic model of the valence band to the study of conductivity or Hall effective mass in p-type silicon. Costato and Reggiani [26] also developed expressions for m_D^* and m_C^*, the band conductivity effective mass, which show a variation with temperature, but they neglected the effects of the split-off band and the temperature variation of the band curvature.

In this study, the expressions for density-of-states effective mass, conductivity effective mass, and Hall effective mass of holes are derived based on the following definitions. The density-of-states effective mass, m_D^*, enters in the normalization of the distribution function; the conductivity effective mass, m_C^*, is the mass of a mobile charge carrier under the influence of an external electric field; and the Hall effective mass, m_H^*, is the mass of a mobile charge carrier under the application of external electric and magnetic fields. The reason for these particular definitions of effective masses is that the primary application of this work is to generate improved theoretical calculations of Hall mobility, resistivity, and conductivity mobility [17]. The derived expressions were used to calculate hole effective masses in p-type silicon over a wide range of temperature and dopant density. Since the crystal structure of silicon has cubic symmetry, the ohmic mobility and the low-field Hall coefficient are isotropic. An angular average of the effective masses may be performed taking into account separately the warping of the individual bands so that expressions for m_D^*, m_C^*, and m_H^* of isotropic form can be derived. Values calculated from these expressions differ from one another because of the warping and nonparabolicity, and consequently effective mass in each band depends on temperature and dopant density in its own way. The valence band structure of silicon is presented in Section 2.2, and in Section 2.3 expressions for m_D^*, m_C^*, and m_H^* are derived.

2.2 The Valence Band Structure of Silicon

Theoretical calculations by Kane [27] have established some basic features of the valence band of silicon. It consists of heavy-hole and light-hole bands, degenerate at $\overline{k} = 0$, and a third band displaced down in energy at $\overline{k} = 0$ by spin orbit coupling.

The heavy-hole band is characterized by holes with an energy independent, but direction-dependent effective mass. The light-hole band is characterized by holes with an energy and direction-dependent effective mass. These two bands can be described by the E vs $\overline{k}$ relationship [28]

$$E(k) = \frac{-\hbar^2}{2m_0}\left\{ Ak^2 \pm \left[B^2k^4 + C^2(k_x^2k_y^2 + k_x^2k_z^2 + k_y^2k_z^2)\right]^{\frac{1}{2}} \right\} \qquad (2.1)$$

where A, B, and C are the experimentally determined inverse mass band parameters, $k = (k_x^2 + k_y^2 + k_z^2)^{\frac{1}{2}}$, and the upper sign is associated with the holes in the light-hole band, while the lower sign is associated with the holes in the heavy-hole band. Values of A, B, and C are obtained by cyclotron resonance measurements at 4 K [22,29].

Although warped, the bands are parabolic for small values of $\overline{k}$. However, for larger values of $\overline{k}$, the bands become nonparabolic, and along the <100> and <111> directions the heavy- and light-hole bands are parallel over most of the Brillouin zone. This situation, however, is not strictly valid for general directions [30]. The assumption of overall parallelism, while questionable in III-V compounds, is reasonable in the case of Ge and Si [27,31]. The split-off band is separated at $\overline{k} = 0$ by an energy $\Delta = 0.044$ eV. [32], and is characterized by an effective mass which is independent of energy and direction. If the anisotropy is small, the square root in equation (2.1) may be expanded [20] and the energy surfaces may be expressed by

$$E = E_v - \frac{\hbar^2k^2}{2m_0}(A \pm B')j(\theta,\phi) \qquad (2.2)$$

where

$$B' = (B^2 + C^2/6)^{\frac{1}{2}} \tag{2.3}$$

θ and ϕ are the spherical coordinates, E_V is the top of the valence band, and

$$j(\theta,\phi) = 1 + \frac{1}{2}\gamma[\sin^4\theta(\cos^4\phi + \sin^4\phi) + \cos^4\theta - 2/3] \tag{2.4}$$

with

$$\gamma = \mp C^2/2B'(A \pm B') \tag{2.5}$$

Following the work of Barber [25], we have used the simplified model of the band structure illustrated in Figure 2.1. In this model the heavy-hole band is considered parabolic and thus the mass m_1^* is a constant, equal to its value at 4.2 K. For energies within 0.02 eV the light-hole band is considered parabolic with a constant slope corresponding to the value of m_2^* at 4.2 K. For higher energies the light-hole band is assumed to take on approximately the same slope as that of the heavy-hole band, but remains separated from the heavy-hole band by $\Delta/3$ eV [27]. The extrapolation of these two constant slopes creates the kink in the light-hole band at 0.02 eV. Because of the change in slope, the light-hole band has an energy-varying effective mass and in general can only be described in terms of partial Fermi-Dirac integrals [25]. Although the split-off band is parabolically distributed, the apparent effective mass at the top of the valence band is a function of temperature due to the energy displacement at $\bar{k} = 0$. Theoretical and experimental studies [33,34] have shown that at high temperatures the heavy-hole band is not parabolic and thus m_1^* is not energy and temperature independent. However, within the range of

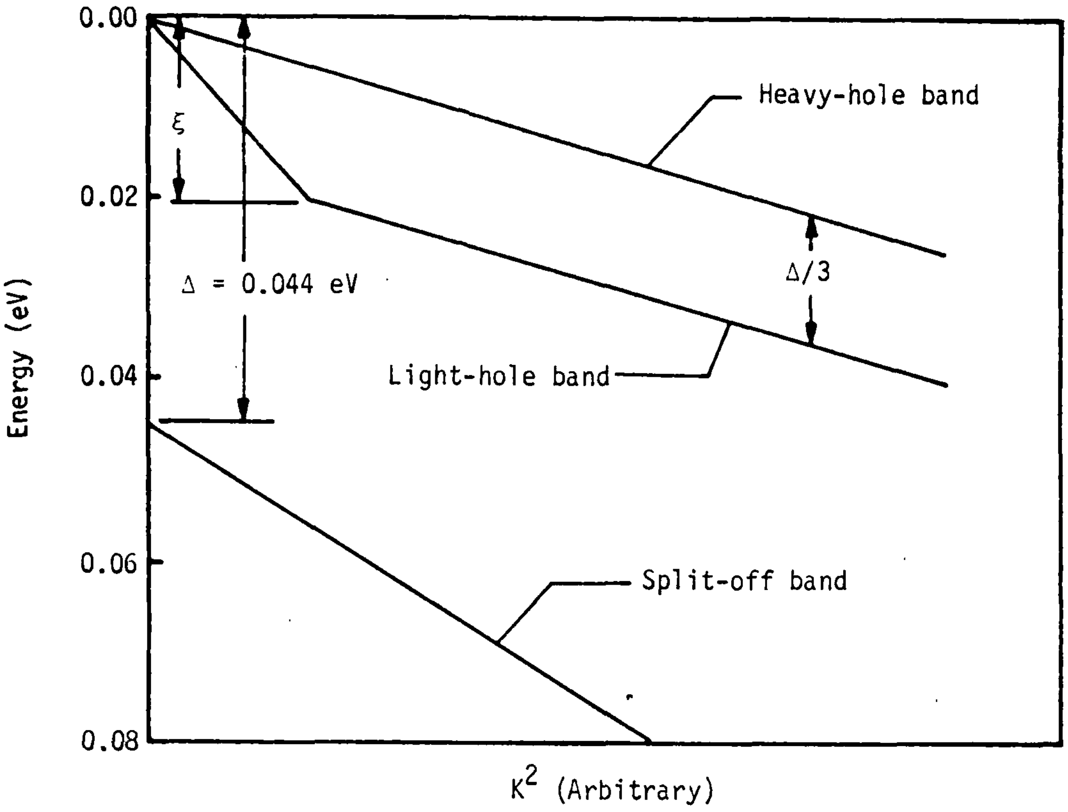

Figure 2.1. Simplified valence band structure of silicon based on Kane's [27] calculations and measured properties of the valence band.

temperatures considered here, the assumption of parabolicity for the heavy-hole band based on Kane's model [27] is reasonable. Other studies [35,36] support the validity of this model for the valence band of silicon.

2.3 Effective Mass Formulation

In the case of spherically symmetric energy surfaces all of the carriers respond in the same way to a given set of applied forces. The effective mass then acts as a scalar and thus has the same value for the Hall effect, conductivity, and density of states. For nonspherical energy surfaces, however, this is not the case. The mixed response of carriers to a set of applied forces is reflected in differences between the different kinds of effective masses. The density-of-states effective mass, m^*_{Di}, is defined from the relationship

$$p_i = \frac{4}{\sqrt{\pi}} \left[\frac{2\pi k_o T m^*_{Di}}{h^2} \right]^{3/2} F_{1/2}(\eta) \tag{2.6}$$

where

$$F_{1/2}(\eta) = \int_0^\infty \frac{\varepsilon^{\frac{1}{2}} d\varepsilon}{1 + \exp(\varepsilon - \eta)} \tag{2.7}$$

$\varepsilon = (E_V - E)/k_oT$, $\eta = (E_V - E_F)/k_oT$, k_o is the Boltzmann constant, E_V is the top of the valence band, and $i = 1, 2, 3$ refers to the heavy-hole, light-hole, and split-off bands, respectively.

The electric current density in the presence of electric and magnetic fields can be expressed by [20]

$$J_j = \sigma_{jk}\mathcal{E}_k + \sigma_{jk\ell}\mathcal{E}_k H_\ell + \sigma_{jk\ell m}\mathcal{E}_k H_\ell H_m + \cdots \tag{2.8}$$

where ε_k, H_ℓ, H_m are the electrical and magnetic field components and the σ's represent single-energy-surface conductivity coefficients. The first coefficient in equation (2.8) is the zero-magnetic field electrical conductivity, and the second coefficient is associated with the nondirectional Hall effect. In the limit of weak fields the expansion can be limited to the first two terms. We use the electrical conductivity coefficient, σ_C, to define the conductivity effective mass m^*_{Ci}, by the relationship

$$\sigma_{Ci} = \sigma_{11i} = p_i \frac{e^2 \langle \tau_i \rangle}{m^*_{Ci}} \tag{2.9}$$

and the Hall effect coefficient, σ_H, to define the Hall mobility effective mass by means of [37]

$$\sigma_{Hi} = \sigma_{123i} = p_i \frac{e^3 \langle \tau_i^2 \rangle}{(m^*_{Hi})^2} \tag{2.10}$$

To solve for m^*_{Di}, m^*_{Ci}, and m^*_{Hi}, equations (2.6), (2.9) and (2.10) are equated to the following expressions for p_i, σ_{jk}, and $\sigma_{jk\ell}$:

$$p_i = \frac{1}{4\pi^3} \int f_o(k) d^3k \tag{2.11}$$

$$\sigma_{jk} = - \frac{e^2}{4\pi^3 \hbar^2} \int \tau \frac{\partial f_o}{\partial E} \frac{\partial E}{\partial k_j} \frac{\partial E}{\partial k_k} d^3k \tag{2.12}$$

$$\sigma_{jk\ell} = \frac{e^3}{4\pi^3 \hbar^4} \int \tau \frac{\partial f_o}{\partial E} \frac{\partial E}{\partial k_j} \frac{\partial E}{\partial k_p} \frac{\partial}{\partial k_q} \left(\tau \frac{\partial E}{\partial k_k}\right) \varepsilon_{\ell pq} d^3k \tag{2.13}$$

where f_o is the Fermi-Dirac distribution function and $\varepsilon_{\ell pq}$ is the permutation tensor. Since equations (2.11) through (2.13) do not assume an effective mass, they are valid both for parabolic and nonparabolic band structures. These equations are then evaluated for the model described in Section 2.2.

This procedure yields single m^*_{Di}, m^*_{Ci}, and m^*_{Hi} for an equivalent model which is isotropic and parabolic. These values, in general, will be temperature and carrier-concentration dependent. Although equations (2.6) and (2.11) through (2.13) are expressed in terms of Fermi-Dirac statistics to stress their generality, conductivity and Hall effective masses were derived using Boltzmann statistics to simplify the form of the equation. To obtain values of m^*_{Ci} and m^*_{Hi} we also require a procedure for evaluating $<\tau_i>$ and $<\tau_i^2>$ in equations (2.9) and (2.10). This will be discussed in Chapter III. The following sections present the expressions for the effective masses in the individual bands.

2.3.1 The Heavy-Hole Band

In this band, the effective masses are given by

$$m^*_{D1} = \frac{m_o}{(A-B')} [f(-\gamma)]^{2/3} \tag{2.14}$$

$$m^*_{C1} = \frac{m_o}{(A-B')} \frac{f(-\gamma)}{f_1(-\gamma)} \tag{2.15}$$

and

$$m^*_{H1} = \frac{m_o}{(A-B')} \left[\frac{f(-\gamma)}{f_2(-\gamma)}\right]^{\frac{1}{2}} \tag{2.16}$$

where γ is defined in equation (2.5). In these equations

$$f(\gamma) = (1 + 0.05\gamma + 0.01635\gamma^2 + 0.000908\gamma^3 + \ldots)$$

$$f_1(\gamma) = (1 + 0.01667\gamma + 0.041369\gamma^2 + 0.00090679\gamma^3$$

$$+ 0.00091959\gamma^4 + \ldots)$$

and

$$f_2(\gamma) = (1 - 0.01667\gamma + 0.017956\gamma^2 - 0.0069857\gamma^3$$

$$+ 0.0012610\gamma^4 + \ldots)$$

Since the heavy-hole band was assumed parabolic, the integrals containing τ in equations (2.9) and (2.10) are identical to those in equations (2.12) and (2.13), and cancel out.

2.3.2 The Light-Hole Band

In the light-hole band, as modeled by Figure 2.1, the effective masses of holes are obtained in terms of partial Fermi-Dirac integrals [25]. Thus

$$(m^*_{D2})^{3/2} = \frac{2m_o^{3/2}}{\sqrt{\pi}} \left\{ \frac{f(+\gamma)}{(A+B')^{3/2}} \int_0^{\xi/k_oT} \frac{\varepsilon^{\frac{1}{2}} d\varepsilon}{\exp(\varepsilon)} + \right.$$

$$\left. \frac{f(-\gamma)\eta_1}{(A-B')^{3/2}} \int_{\zeta/k_oT}^{\infty} \frac{\varepsilon_1^{\frac{1}{2}} d\varepsilon_1}{\exp(\varepsilon_1)} \right\} \qquad (2.17)$$

$$m^*_{C2} = \frac{2m_0}{\sqrt{\pi}} \int_0^\infty \frac{\tau_2 \varepsilon^{3/2} d\varepsilon}{\exp(\varepsilon)} \times \left\{ \frac{ \frac{f(+\gamma)}{(A+B')^{3/2}} \int_0^{\xi/k_0T} \frac{\varepsilon^{1/2} d\varepsilon}{\exp(\varepsilon)} + \frac{f(-\gamma)\eta_1}{(A-B')^{3/2}} \int_{\zeta/k_0T}^\infty \frac{\varepsilon_1^{1/2} d\varepsilon_1}{\exp(\varepsilon_1)} }{ \frac{f_1(+\gamma)}{(A+B')^{1/2}} \int_0^{\xi/k_0T} \frac{\tau_2 \varepsilon^{3/2} d\varepsilon}{\exp(\varepsilon)} + \frac{f_1(-\gamma)\eta_1}{(A-B')^{1/2}} \int_{\zeta/k_0T}^\infty \frac{\tau_2 \varepsilon_1^{3/2} d\varepsilon_1}{\exp(\varepsilon_1)} } \right\} \tag{2.18}$$

$$m^*_{H2} = m_0 \frac{ \left\{ (A+B')^{1/2} f_2(+\gamma) \int_0^{\xi/k_0T} \tau_2^2 \varepsilon^{3/2} \exp(-\varepsilon) d\varepsilon + (A-B')^{1/2} f_2(-\gamma)\eta_1 \int_{\xi/k_0T}^\infty \tau_2^2 \varepsilon_1^{3/2} \exp(-\varepsilon_1) d\varepsilon_1 \right\}^{1/2} }{ \left\{ \frac{2}{\sqrt{\pi}} \int_0^\infty \frac{\tau \varepsilon^{3/2} d\varepsilon}{\exp(\varepsilon)} \left[\frac{f(+\gamma)}{(A+B')^{3/2}} \int_0^{\xi/k_0T} \frac{\varepsilon^{1/2} d\varepsilon}{\exp(\varepsilon)} + \frac{f(-\gamma)\eta_1}{(A-B')^{3/2}} \int_{\zeta/k_0T}^\infty \frac{\varepsilon_1^{1/2} d\varepsilon_1}{\exp(\varepsilon_1)} \right] \right\}^{1/2} } \tag{2.19}$$

where $\varepsilon_1 = \varepsilon - \Delta/3k_0T$, $\zeta = \xi - \Delta/3$, $\eta_1 = \exp(-\Delta/3k_0T)$ and Δ and ξ are defined in Figure 2.1.

In this case because equations (2.11) through (2.13) were expressed in terms of partial Fermi-Dirac integrals and equations (2.6), (2.9) and (2.10) were expressed in terms of complete Fermi-Dirac integrals, the dependence on τ does not cancel out. Thus the nonparabolicity of the light-hole band introduces a dependence on the scattering relaxation time. The scattering relaxation time is discussed in Chapter III.

2.3.3 The Split-Off Band

Although the split-off band is parabolic, the apparent effective mass in this band will also exhibit a temperature dependence due to the energy displacement at $\overline{k} = 0$. The energy of a hole in the third band is given by

$$E = E_v - \frac{\hbar^2 k^2}{2m_o} A - \Delta \tag{2.20}$$

where Δ is the split-off energy ($\simeq 0.044$eV), and A is one of the inverse mass band parameters. Substituting equation (2.20) into equations (2.11) through (2.13), and then equating to equations (2.6), (2.9) and (2.10) for the split-off band, we obtain

$$m^*_{D3} = \frac{m_o}{A} \exp\left(- \frac{2\Delta}{3k_oT}\right) \tag{2.21}$$

$$m^*_{C3} = \frac{m_o}{A} \frac{\int_0^\infty \tau_3 \varepsilon^{3/2} \exp(-\varepsilon) d\varepsilon}{\int_0^\infty \tau_3 \varepsilon_2^{3/2} \exp(-\varepsilon_2) d\varepsilon_2} \tag{2.22}$$

$$m^*_{H3} = \frac{m_o}{A} \left\{ \frac{\int_0^\infty \tau_3^2 \varepsilon^{3/2} \exp(-\varepsilon) d\varepsilon}{\int_0^\infty \tau_3 \varepsilon_2^{3/2} \exp(-\varepsilon_2) d\varepsilon_2} \right\}^{\frac{1}{2}} \tag{2.23}$$

where $\varepsilon_2 = \varepsilon - \Delta/k_oT$.

The combined hole density-of-state effective mass can be determined by assuming that the total number of holes in the valence band is equal to the sum of the holes in the individual bands

$$p = p_1 + p_2 + p_3 \tag{2.24}$$

thus

$$m_D^* = [(m_{D1}^*)^{3/2} + (m_{D2}^*)^{3/2} + (m_{D3}^*)^{3/2}]^{2/3} \tag{2.25}$$

This combined effective mass is the mass corresponding to the density-of-states of an effective single equivalent parabolic valence band. This concept is useful in calculations where the effective density-of-states at different temperatures can be calculated from one m_D^*.

The explicit temperature variation of the band curvature is included by assuming that the density-of-states near the band edges varies in a similar manner as the temperature dependence of the energy gap [25]. Thus $(m_D^*)^{3/2}$ is porportional to E_{Go}/E_G where E_{Go} is the energy gap at 0 K.

To evaluate the total band equivalent conductivity and Hall effective masses, we assume that in valence band conduction, the total number of holes in motion is equal to the sum of the holes moving on the separate energy surfaces, and that these holes can be modeled as moving on a single spherical energy surface. Thus, the ohmic and the Hall conductivities in the equivalent valence band are given by

$$\sigma_C = \sigma_{C1} + \sigma_{C2} + \sigma_{C3} \tag{2.26}$$

and

$$\sigma_H = \sigma_{H1} + \sigma_{H2} + \sigma_{H3} \tag{2.27}$$

respectively.

Substituting equations (2.9) and (2.10) into equations (2.26) and (2.27) it follows that

$$m_C^* = \left\{ \frac{\langle\tau_1\rangle}{\langle\tau\rangle} \left(\frac{m_{D1}^*}{m_D^*}\right)^{3/2} \frac{1}{m_{C1}^*} + \frac{\langle\tau_2\rangle}{\langle\tau\rangle} \left(\frac{m_{D2}^*}{m_D^*}\right)^{3/2} \frac{1}{m_{C2}^*} + \frac{\langle\tau_3\rangle}{\langle\tau\rangle} \left(\frac{m_{D3}^*}{m_D^*}\right)^{3/2} \frac{1}{m_{C3}^*} \right\}^{-1} \tag{2.28}$$

and

$$m_H^* = \left\{ \frac{\langle\tau_1^2\rangle}{\langle\tau^2\rangle} \left(\frac{m_{D1}^*}{m_D^*}\right)^{3/2} \frac{1}{m_{H1}^{*\,2}} + \frac{\langle\tau_2^2\rangle}{\langle\tau^2\rangle} \left(\frac{m_{D2}^*}{m_D^*}\right)^{3/2} \frac{1}{m_{H2}^{*\,2}} + \frac{\langle\tau_3^2\rangle}{\langle\tau^2\rangle} \left(\frac{m_{D3}^*}{m_D^*}\right)^{3/2} \frac{1}{m_{H3}^{*\,2}} \right\}^{-\frac{1}{2}} \tag{2.29}$$

Equations (2.25), (2.28) and (2.29) were evaluated numerically as functions of temperature and acceptor doping density for p-type silicon. Values of the band parameters, $|A| = 4.27$, $|B| = 0.63$ and $|C| = 4.93$, were determined at 4.2 K by Hensel and Feher [22] and Balslev and Lewaetz [29]. In order to simplify the calculations and maintain tractability, anisotropies in the relaxation time were ignored. A rigorous analysis of the conductivities for nonisotropic scattering would be extremely difficult to carry out because no relaxation time is expected to exist in the usual sense [38].

Figure 2.2 shows the dependence of m_D^* with temperature in the range from 100 to 400 K. The slight temperature dependence due to the explicit temperature variation of the curvature at the edge of the band results in an effective mass increase of about five percent in each band at 400 K. This can be seen in the slope of m_{D1}^*. The temperature dependence of m_{D3}^* is more pronounced since here we also have the effects of energy displacement at $\bar{k} = 0$. The temperature dependence due to nonparabolicity is very apparent in the shape of the m_{D2}^* curve.

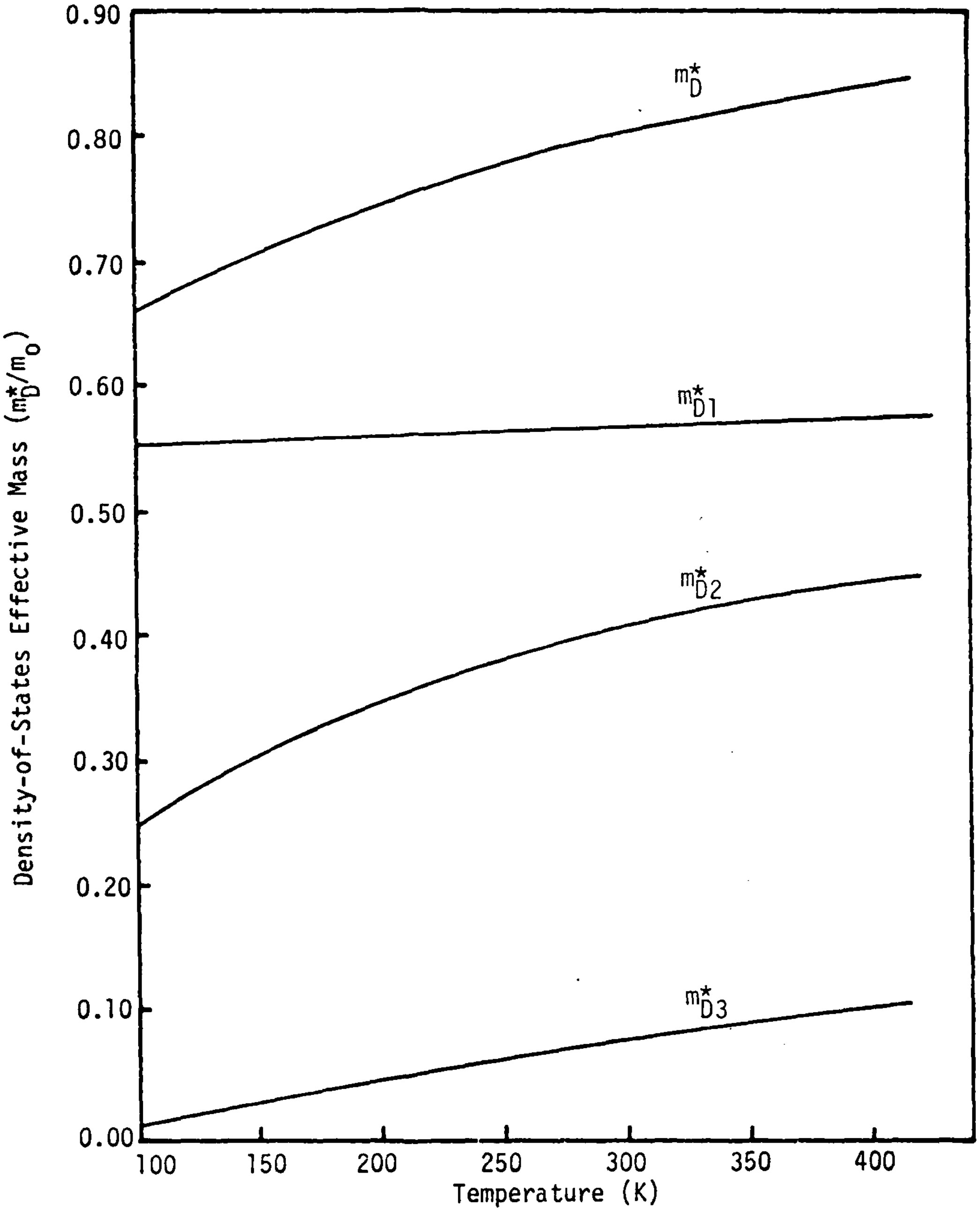

Figure 2.2. Temperature dependence of the density-of-state effective masses m_{D1}^*, m_{D2}^* and m_{D3}^*, in the individual bands, and the combined density-of-states mass m_D^* of holes in silicon. $N_A = 10^{14}$ cm^{-3}.

The temperature dependence of the conductivity effective mass and the Hall effective mass is shown in Figures 2.3 and 2.4, with the dopant density equal to 10^{14} cm^{-3}. One consequence of the nonparabolicity of the light-hole band is an increase in the valence band conductivity effective mass as temperature increases from 100 to 400 K. This happens because with increasing thermal energy k_oT, more holes reside in the less parabolic regions of the light-hole band. The results plotted in Figure 2.3 show an increase in m_C^* of about 36 percent in this temperature range. The temperature dependence of m_H^* can be attributed mainly to the non-parabolicity of the light-hole band. In the temperature range from 100 to 400 K, m_H^* increases from 0.2850 to 0.5273 m_o. The slight temperature dependence of m_{C1}^* and m_{H1}^* is due to the explicit temperature effect and results in increases of 7.7 percent and 3.76 percent in the m_{C1}^* and m_{H1}^* respectively. A larger temperature variation occurs in the case of the split-off band because of the additional effects of the energy displacement at $\overline{k} = 0$.

Figures 2.5 and 2.6 show the variation of m_C^* and m_H^* with dopant density and temperature. For $T \geq 100$ K, m_C^* varies less than 10 percent in the dopant density range from 10^{14} to 10^{18} cm^{-3}. Since the influence of nonparabolicity is reduced in degenerate material [25], it follows as shown in Figures 2.5 and 2.6 that the variation of effective mass with temperature is much stronger at low dopant densities. At lower temperatures there is a much greater change in effective mass due to variations in scattering relaxation time with percentage of ionized impurities.

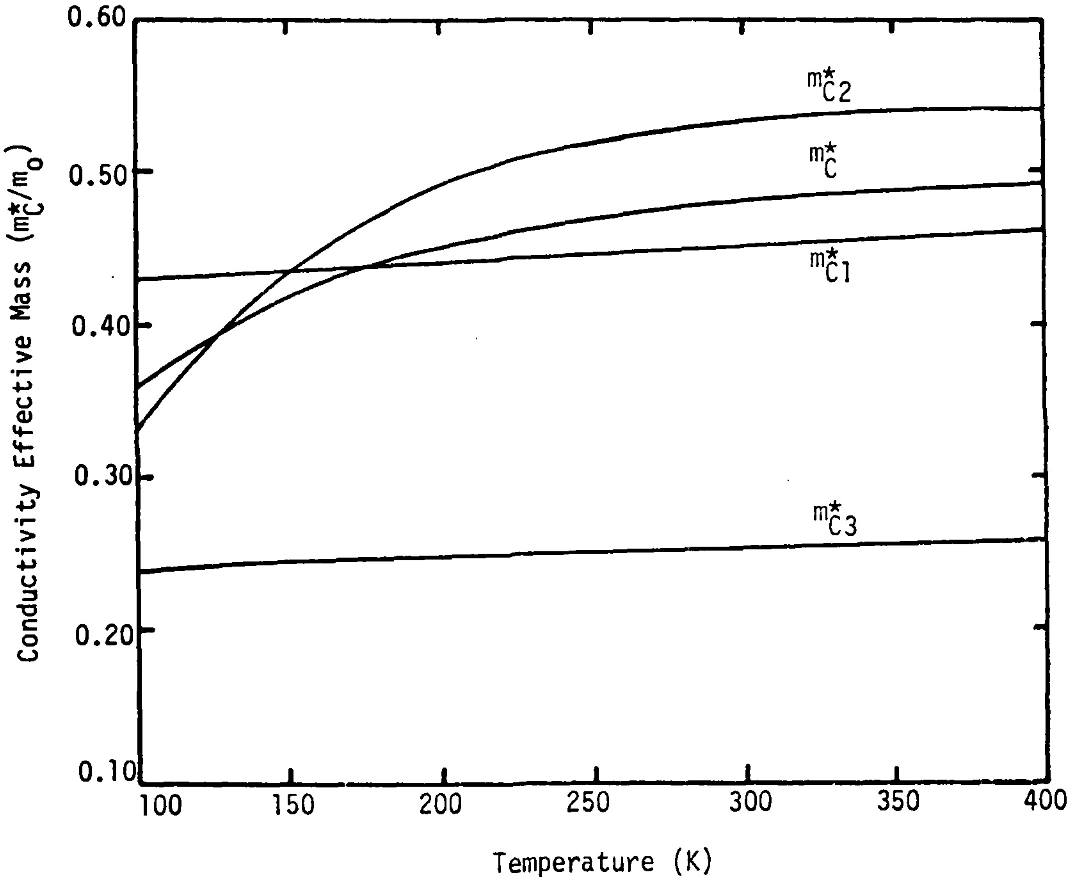

Figure 2.3. Temperature dependence of the conductivity effective masses m_{C1}^*, m_{C2}^* and m_{C3}^* in the individual bands, and the combined conductivity effective mass m_C^* of holes in silicon. $N_A = 10^{14}$ cm^{-3}.

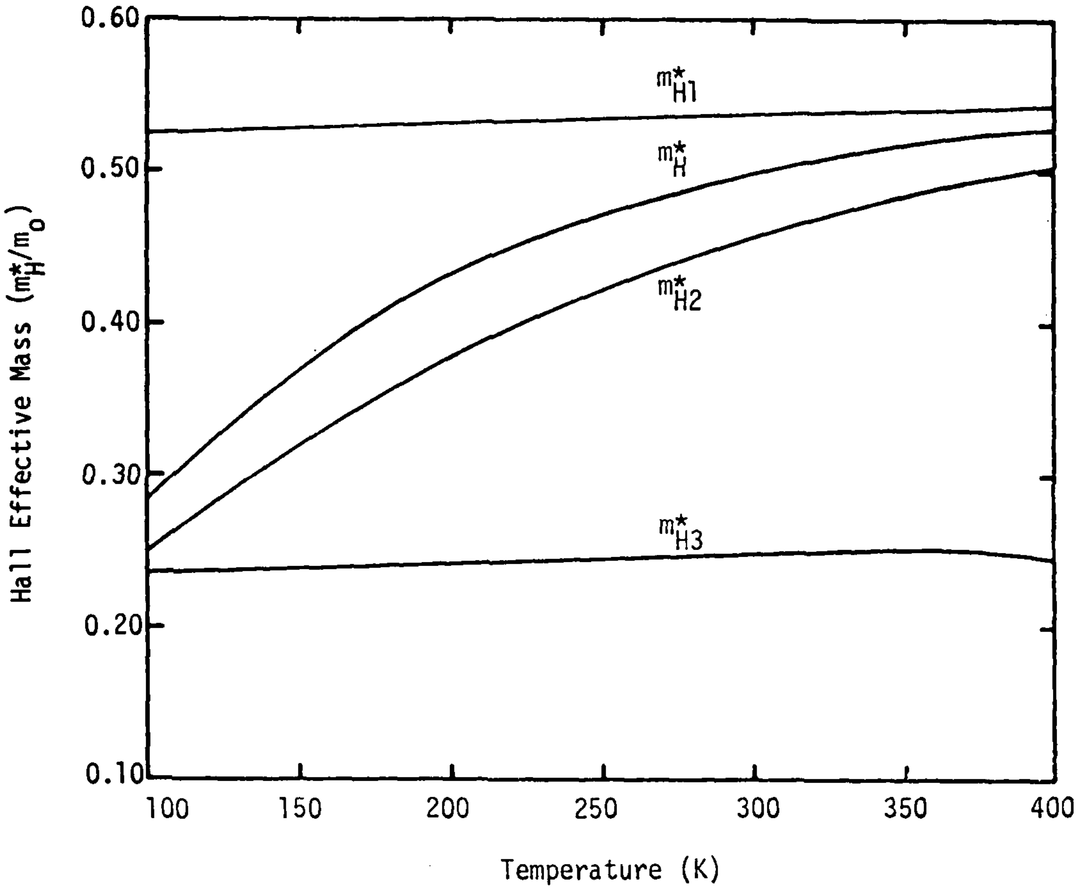

Figure 2.4. Temperature dependence of the Hall effective masses, m_{H1}^*, m_{H2}^* and m_{H3}^* in the individual bands, and the combined Hall effective mass m_H^* of holes in silicon. $N_A = 10^{14}$ cm^{-3}.

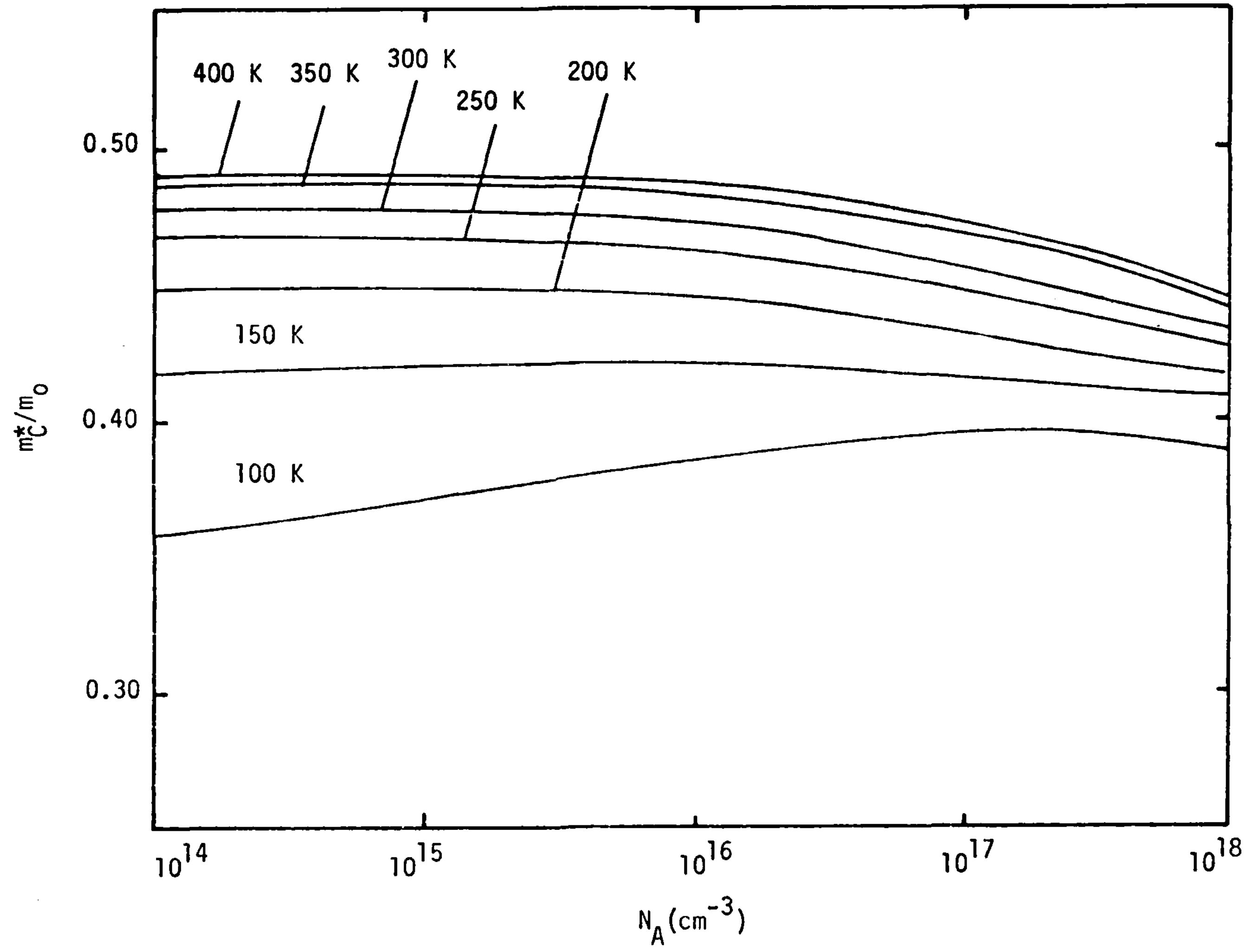

Figure 2.5. The acceptor density dependence of the combined conductivity effective mass of holes in silicon as a function of temperature.

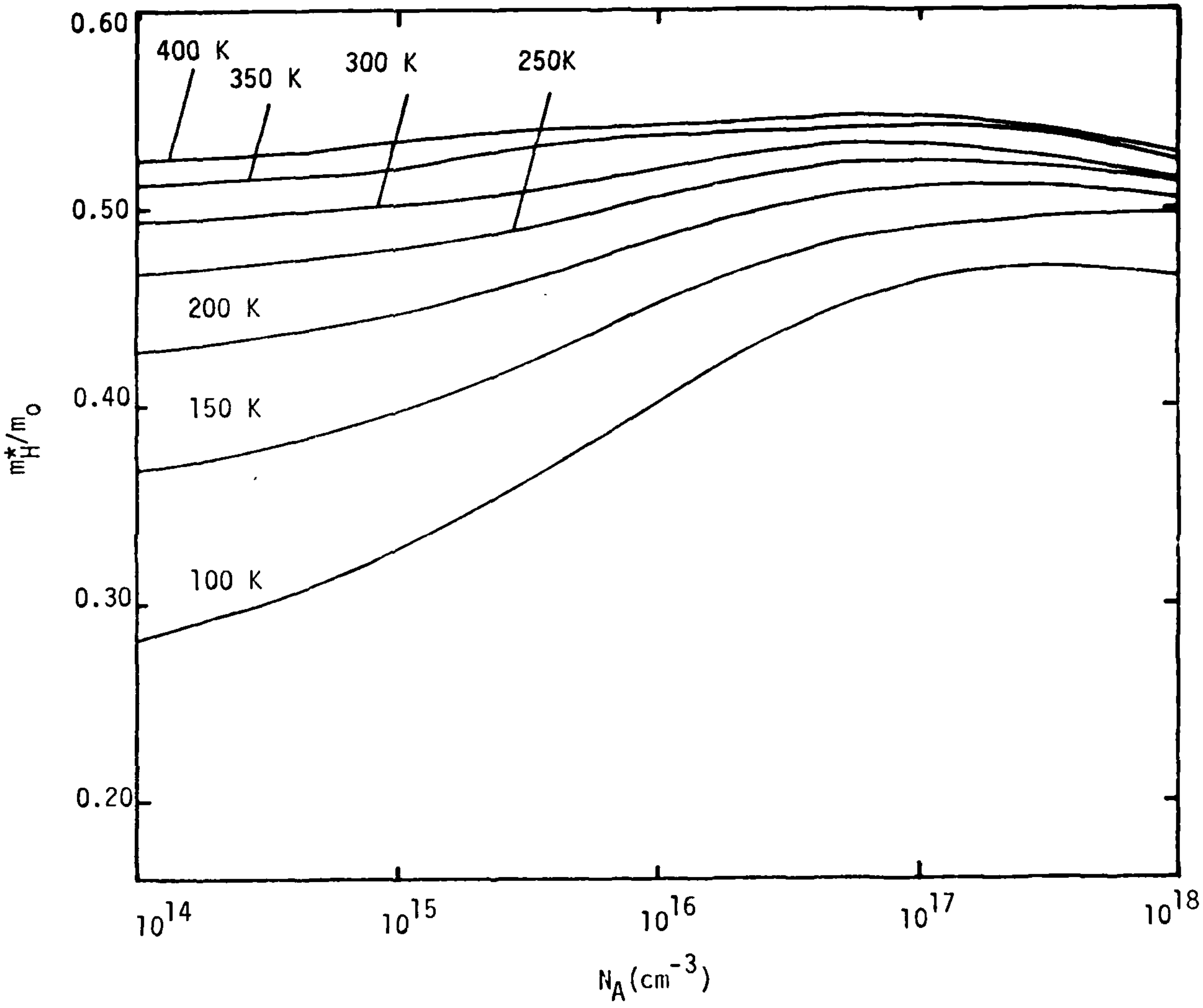

Figure 2.6. The acceptor density dependence of the combined Hall effective mass of holes in silicon as a function of temperature.

2.4 Discussion

The idea of temperature-dependent effective mass is supported by a number of experimental data. Cardona et al [21] found an increase of about 12 percent in optical effective mass between 90 and 300 K in heavily-doped p-type silicon. Cyclotron-resonance studies conducted by Hensel and Feher [22] show that when carrier heating populates deeper regions of the light-hole band, the nonparabolic nature of this band at higher values of $\overline{k}$ results in an increase in the effective mass of holes.

The model used here in the calculation of hole density-of-states effective mass is identical to that of Barber [25], and consequently our results for m_{Di}^* and m_D^* are in excellent agreement with those of Barber [25]. We have extended Barber's work to the calculations of m_C^* and m_H^* in p-type silicon. The increase of m_C^* by 36 percent at 400 K shown in Figure 2.3 is much larger than that reported by Costato and Reggiani (9 percent) [26]. Their calculation was done over a similar range of temperatures, and their value at 100 K, m_C=0.342 m_o, is somewhat lower than our calculated value (.3604 m_o). The discrepancies between our results and those of Costato and Reggiani are due mainly to the correction of m_D^* for the explicit temperature dependence of the energy gap, the inclusion of the split-off band, and the consideration of unequal relaxation times in the three bands. Note that our calculations of effective masses were achieved through more rigorous mathematical derivations, while those of Costato and Reggiani followed a more empirical curve-fitting type of procedure.

The experimental values of density-of-states effective masses of holes in p-type silicon have been published by numerous authors [21,22, 39,40], but very little data can be found for the conductivity and the

Hall effective masses, making it difficult to properly assess the value of our calculations. There seems to be no obvious way to measure these quantities from d.c. transport measurements. Magneto-kerr effect measurements conducted by Hauge [41], indicate that m_c^* could increase by as much as 31 percent in the range of temperatures from 100 (M_c^* = 0.510 M_0) to 300 K. This is in reasonable agreement with our calculated percentage increase in m_c^* in the same temperature range (33 percent), but it is impossible to compare our calculations with Hauge's experimental results, because our effective mass definition was chosen to be mainly applicable to the study of the Hall and conductivity mobility in the low field limit, and this may not apply to the measurements of Hauge [41].

From the results of this chapter it can be seen that the approximation of a constant effective mass seems to be inadequate to describe transport properties of holes in silicon above 100 K. There is a substantial increase in the effective mass of holes from 100 to 400 K due to the nonparabolicity of the light-hole band, and a smaller, though not negligible, contribution due to the explicit temperature dependence and the effects of the split-off band. The validity of this model for the calculation of density-of-states effective mass has been well established [25]. Barber [25] has shown that when the temperature-dependent effective masses are substituted into the theoretical expression for intrinsic carrier density in silicon, the agreement with reported measurements of n_i is within the limits of experimental error. Application of this model to theoretical calculation of mobility and resistivity in p-type silicon [17] has provided excellent agreement between theoretical and and experimental values (resistivity with ±6 percent) over a temperature range from 100 to 400 K and dopant density range from 10^{14} to $3\text{x}10^{18}$ cm^{-3}. This calculation is limited to applications in conductivity mobility and low field Hall effect.

CHAPTER III

MOBILITY AND SCATTERING RELAXATION TIME

3.1 Introduction

The study of transport phenomena in semiconductors requires an accurate knowledge of variations in the conductivity mobility and the resistivity with changes in temperature and dopant density. The resistivity is an easily-measured parameter, but the conductivity mobility is a more difficult parameter to evaluate. In general, four different kinds of mobility enter into common discussion [42]. The microscopic mobility is the actual velocity per unit electric field of a free carrier in a crystal. This cannot be measured directly. The conductivity mobility is the mobility associated with the conductivity expression, $\sigma = ep\mu_C$. This mobility involves an average relaxation time $\langle\tau\rangle$ dependent on the nature of the scattering process, and in the case of nonspherical equal energy surfaces, this mobility also involves a combined effective mass. The Hall mobility is the product of the measured conductivity and the measured Hall coefficient. In general, the Hall mobility differs from the conductivity mobility by a factor called the Hall factor. The drift mobility is the velocity or drift per unit field for a carrier moving in an electric field. If trapping centers are present, so that the actual drift process is not simply motion through the conduction band, but involves a series of trapping and untrapping processes, the drift mobility can be much less than the conductivity mobility. The four mobilities are all equal only when the following three conditions are met [42]: (a) spherical equal energy surfaces with extremum at $\overline{k} = 0$, (b) relaxation time independent of carrier energy, and (c) negligible trapping effects. Since conditions (a) and (b) are not met in p-type silicon, it is improper to judge the behaviour of one kind of mobility based on knowledge of a different kind of mobility. Thus drift or Hall mobility data cannot be tacitly assumed to be accurate substitutes for conductivity mobility values.

As mentioned above, the conductivity mobility involves an average scattering relaxation time. In any semiconductor, the charge carriers (i.e., holes and electrons), at temperatures above absolute zero, may be scattered by a number of mechanisms. Different mechanisms are dominant in certain temperature and dopant density regimes, but in some cases two or more may be interacting simultaneously. Thus in calculating the conductivity mobility over a wide range of temperatures and dopant densities, all the relevant scattering mechanisms must be taken into account. In the case of silicon, acoustic and optical phonon scattering, and ionized and neutral impurity scattering are of major importance. Hole-hole scattering also plays an important role in determining the mobility. In the following sections the theoretical effects of these scattering mechanisms on the mobility will be considered.

3.2 Mobility and Average Scattering Relaxation Time

The calculation of mobility of holes in the valence band of silicon is accomplished by evaluating the mobility separately in the heavy-hole band, the light-hole band, and the split-off band considering all appropriate scattering mechanisms. The overall mobility is then evaluated as a weighted average of the single-band mobilities over the individual hole densities in each band.

The conductivity mobility in each of the three valence bands is calculated from

$$\mu_{Ci} = \frac{e<\tau_i>}{m^*_{Ci}} \tag{3.1}$$

where

$$<\tau_i> = \frac{\int \varepsilon^{3/2}\tau_i\left(\frac{\partial f_o}{\partial \varepsilon}\right)d\varepsilon}{\int \varepsilon^{3/2}\left(\frac{\partial f_o}{\partial \varepsilon}\right)d\varepsilon} \tag{3.2}$$

for the case of Fermi-Dirac statistics, and τ_i represents the total scattering relaxation time in band i. Because each scattering mechanism has its own dependence on scattering energy, a simple closed form expression for total scattering relaxation time as a function of temperature cannot be obtained. The use of numerical techniques is necessary to solve for the relaxation time. In the case of p-type silicon, the peculiarities of a degenerate, warped, and nonparabolic valence band must be taken into account [1]. The possibility of interband as well as intraband transitions must also be taken into account in the analysis. With the inclusion of interband scattering as given by Bir et al. [43], the total relaxation time in the heavy- (i = 1) and light-holes (i = 2) bands is given by

$$\tau_i = \frac{1}{\delta}\left(1 + \frac{m^*_{Di}}{m^*_{Dj}}\,\frac{\tau_{jj}}{\tau_{ij}}\right)\tau_{ii} \qquad i \neq j;\ i = 1,2;\ j = 1,2 \tag{3.3}$$

where

$$\delta = 1 - \frac{\tau_{11}\tau_{22}}{\tau_{12}\tau_{21}} \tag{3.4}$$

and

$$\tau_{ii} = \left[\tau_{aci}^{-1} + \tau_{oi}^{-1} + \tau_{Ii}^{-1} + \tau_{Ni}^{-1}\right]^{-1} \tag{3.5}$$

The total relaxation time in the split-off band is given by

$$\tau_3 = \left[\tau_{ac3}^{-1} + \tau_{o3}^{-1} + \tau_{I3}^{-1} + \tau_{N3}^{-1}\right]^{-1} \tag{3.6}$$

Only transitions between the light- and heavy-hole band are considered; the relaxation time τ_{ji} takes into account a transition from band i to band j; and τ_{aci}, τ_{oi}, τ_{Ii}, and τ_{Ni} are the relaxation times corresponding to scattering by acoustical phonons, optical phonons, ionized impurities, and neutral impurities respectively, with i as the band index. The procedure for including the nonparabolicity of the band structure into calculations of relaxation time, consists of modifying the relaxation time for a given scattering process by replacing the temperature independent effective mass of the parabolic band by the temperature dependent effective mass of the nonparabolic band. This procedure has been successfully applied to the study of acoustic phonon scattering in nonparabolic bands by Radcliffe [18]. Optical phonon and ionized impurity scattering in nonparabolic bands have been considered by Barrie [19] in the same manner. Braggins [1] has used the same method to include nonparabolicity in his study of p-type silicon. In this work, the relaxation times appropriate to degenerate, parabolic valence bands have been used and modified according to the prescription of Radcliffe [18], Barrie [19], and Braggins [1]. The anisotropy of the energy spectrum is not considered in this model, because from the transport theory for parabolic bands it is known that this anisotropy has no influence on the temperature dependence of mobility, but only on its absolute value [10]. Each of the four scattering mechanisms will now be discussed.

3.3 Acoustical Phonon Scattering

The relaxation time for scattering by acoustical phonons includes both the possibility of interband as well as intraband scattering. The treatment of the acoustical phonons has been based on the theory of Bir, Normantas, and Pikus [43] where the relaxation times can be expressed in terms of a single constant, τ_x, which controls the overall magnitude of the scattering. Both transverse and longitudinal phonons participate in the scattering so that

$$\tau_{ac1}^{-1} = \frac{m_{D1}^{*\,3/2}}{\tau_x} \left\{ L_{11}^{(2)} + \gamma_{ij}^{3} L_{11}^{(1)} + \frac{C_\ell^2}{C_t^2} \beta^2 \left[T_{11}^{(2)} + \gamma_{ij}^{3} T_{11}^{(1)} \right] \right\} T^{3/2} \varepsilon^{1/2} \tag{3.7}$$

and

$$\tau_{ac2}^{-1} = \frac{m_{D2}^{*\,3/2}}{\tau_x} \left\{ L_{22}^{(2)} + \gamma_{ij}^{3} L_{22}^{(1)} + \frac{C_\ell^2}{C_t^2} \beta^2 \left[T_{22}^{(2)} + \gamma_{ij}^{3} T_{22}^{(1)} \right] \right\} T^{3/2} \varepsilon^{1/2} \tag{3.8}$$

for intraband scattering, while

$$\tau_{ij}^{-1}\,\gamma_{ij}^{-5} = \tau_{ji}^{-1} = \frac{m_{Di}^{*\,3/2}}{\tau_x}\left\{ L_{ij}^{(2)} + \frac{C_\ell^2}{C_t^2}\,\beta^2\left[T_{ij}^{(2)}\right]\right\} T^{3/2}\varepsilon^{1/2} \tag{3.9}$$

for interband scattering. In the split-off band, the scattering relaxation time is given by

$$\tau_{ac3}^{-1} = \frac{1}{\tau_x}\left(\varepsilon - \frac{\Delta}{k_oT}\right)^{1/2} T^{3/2} \tag{3.10}$$

In these equations

$$\frac{1}{\tau_x} = \frac{k_o^{3/2}a^2m_o^{3/2}}{\sqrt{2}\pi\hbar^4\rho_s C^2_\ell} \tag{3.11}$$

$\gamma_{ij} = m^*_{Di}/m^*_{Dj}$, $\beta = b/a$, a and b are valence band acoustic deformation potential constants in the Picus and Bir [44] notation, ρ_s is the density, C_ℓ and C_t are the longitudinal and transverse sound velocities in silicon and L_{ij} and T_{ij} are functions of β and γ_{ij} defined in [43].

3.4 Optical Phonon Scattering

Optical phonon scattering, while negligible at very low temperatures, cannot be ignored at high temperatures. Ehrenreich and Overhauser [45] have calculated the mobility of holes in silicon and its dependence on temperature. The calculated mobility follows a $T^{-2.3}$ dependence for reasonable choices of the parameters which described the mixing of optical and acoustical phonon scattering. This agrees with experimental results [5,8]. The relaxation time for scattering by nonpolar optical phonons is given by [46]

$$\tau_{oi}^{-1} = \frac{m_{Di}^{*\,3/2}}{\tau_x} W\theta_D T^{1/2} \left\{ (n_o+1)\left(\varepsilon - \frac{\theta_D}{T}\right)^{1/2} + n_o\left(\varepsilon + \frac{\theta_D}{T}\right)^{1/2} \right\} \qquad i = 1,2,3 \tag{3.12}$$

where θ_D is the Debye temperature, $n_o = (\exp(\theta_D/T)-1)^{-1}$ is the phonon distribution function, and W is a constant which determines the relative coupling strength of the holes to the optical phonon mode compared to the acoustical phonon mode

$$W = \frac{D_o^2 \hbar^2 C_\ell^2}{2k_o^2 a^2 \theta_D^2} \tag{3.13}$$

where D_o^2 is the optical deformation potential constant. The first term in the brackets of equation (3.12) corresponds to optical phonon emmission and is relevant only when this is energetically possible ($\varepsilon > \theta_D/T$). The second term in the brackets corresponds to optical phonon absorption.

3.5 Ionized Impurity Scattering

The Columbic interaction between ionized impurities and charge carriers drifting through the cyrstal under the action of an applied electric field causes scattering of the charge carriers. Scattering by ionized impurities was first considered by Conwell and Weisskopf [47]. The basic assumption is that the Coulomb field is cut off at half the distance between charged impurities. This is equivalent to assuming that a charge carrier sees only one charged impurity at a time, the effect of the other charged impurities being sufficiently screened as to be negligible. This approach was improved by Brooks [48] and Herring [49] who associated the cut-off of the Coulomb potential with a screening distance, the free carriers being assumed to provide screening against the charge of the impurities. In the low dopant density limit, the scattering relaxation time due to ionized impurities is given by [48,49]

$$\tau_{Ii}^{-1} = \frac{\pi e^4 N_A^- G(b_i)}{(2m_{Di}^*)^{1/2} \varepsilon_s^2 (k_o T)^{3/2}} \varepsilon^{-3/2}, \qquad i = 1,2,3 \tag{3.14}$$

where

$$G(b_i) = \ell n(b_i+1) - \frac{1}{(b_i+1)} \tag{3.15}$$

and

$$b_i = \frac{24\pi \; m_{Di}^* \varepsilon_s (k_o T)^2}{e^2 h^2 p'} \tag{3.16}$$

where p' is the screening carrier density, $p' = p + N_A^-(1 - N_A^-/N_A)$, for $N_D = 0$.

3.6 Neutral Impurity Scattering

Scattering by neutral impurities in semiconductors has been considered by Erginsoy [50] as a variation of the problem of the scattering of electrons by neutral hydogen atoms. The result is a temperature independent relaxation time given by

$$\tau_{Ni}^{-1} = \left(\frac{\varepsilon_s \hbar^2}{m_G^* e^2}\right) \frac{20\hbar}{m_{Di}^*} N_N, \qquad i = 1,2,3 \tag{3.17}$$

where N_N is the density of neutral impurities and m_G^* is the geometric mean mass appropriate for evaluating the scaled Bohr radius term [48]. Sclar [51,52] has included the possibility of bound states in the evaluation of electron-hydrogen impurity scattering by using a three-dimensional square well to estimate the influence of a weakly-bound state on the scattering. In this case the relaxation time is given by

$$\tau_{Ni}^{-1} = \frac{2^{3/2}\pi\hbar^2 N_N}{(k_o T)^{1/2} m_{Di}^{*\,3/2}} \left\{ \varepsilon^{1/2} + \frac{E_1}{k_o T\, \varepsilon^{1/2}} \right\}, \qquad i = 1,2,3 \tag{3.18}$$

where

$$E_1 = 1.136 \times 10^{-19} \frac{m_D^*}{m_o} \left(\frac{\varepsilon_o}{\varepsilon_s}\right)^2 \tag{3.19}$$

is the binding energy of neutral acceptors.

For silicon doped with shallow impurities, this type of scattering is important at low temperatures where neutral impurities may outnumber ionized impurities. For the deeper levels, where neutral impurities can exist at higher temperatures, the influence of neutral impurity scattering can extend over a wide range of temperatures.

3.7 Effect of Hole-Hole Scattering

The expressions thus far presented for scattering relaxation time neglect the effect of hole-hole scattering. Although hole-hole scattering does not affect the current density directly since it cannot alter the total momentum, it tends to randomnize the way in which this total momentum is distributed among holes of different energies. When the scattering mechanism is such as to lead to a nonuniform distribution, hole-hole scattering gives rise to a net transfer of momentum from holes which dissipate momentum less efficiently to those which dissipate momentum more efficiently, resulting in an overall greater rate of momentum transfer, and lower mobility [53]. Thus the size of the effect of hole-hole scattering on the scattering relaxation time is a function of the energy dependence of the relaxation time. The hole-hole reduction factor, γ_{hh}, can be derived by means of a classical formulation introduced by Keyes [54]. When hole-hole collisions are much more frequent than hole-acceptor collisions, the average relaxation time for a parabolic band in the Keyes [54] approximation approaches the limiting form

$$\langle\tau_{hh}\rangle = \frac{\int \varepsilon^{3/2}\left(\frac{\partial f_o}{\partial \varepsilon}\right)d\varepsilon}{\int \varepsilon^{3/2}\tau^{-1}\left(\frac{\partial f_o}{\partial \varepsilon}\right)d\varepsilon} \tag{3.20}$$

where f_o is the Fermi-Dirac distribution function. On the other hand, if hole-hole collisions are neglected, the average relaxation time is given by equation (3.2).

Thus the hole-hole reduction factor (i.e., the ratio of $\langle\tau_{hh}\rangle$ to $\langle\tau\rangle$) can be expressed as

$$\gamma_{hh} = \left\{ \frac{\int \varepsilon^{3/2}\tau\left(\frac{\partial f_o}{\partial \varepsilon}\right)d\varepsilon \times \int \varepsilon^{3/2}\tau^{-1}\left(\frac{\partial f_o}{\partial \varepsilon}\right)d\varepsilon}{\left[\int \varepsilon^{3/2}\left(\frac{\partial f_o}{\partial \varepsilon}\right)d\varepsilon\right]^2} \right\}^{-1} \tag{3.21}$$

$$\gamma_{hh} = \frac{1}{<\tau><\tau^{-1}>} \tag{3.21a}$$

for optical phonon scattering, and $\gamma_{hh}{}^{o}$, the hole-hole reduction factor, is evaluated from equation (3.21).

For acoustical phonon scattering it is assumed that $\gamma_{hh}{}^{a}$ decreases linearly with increasing dopant density from a value of one to a value $\gamma_{hh}{}^{a} = 9\pi/32 = 0.88$ [17] in a certain range of impurity concentration. The exact relationship ($\gamma_{hh}{}^{a} = 1.0004 - 4.013378 \times 10^{-19} N_A$, $10^{15} \leq N_A \leq 3 \leq 10^{17}$) is determined empirically with a best fit of the experimental data.

Luong and Shaw [55] using a one-particle-like approximation from the Hartree-Fock theory, have shown that by inclusion of hole-hole scattering, the Brooks-Herring [48,49] formula is reduced by a factor which can be expressed in closed form as

$$\gamma_{hh}{}^{i} = \left(\frac{N_A^-}{p'}\right) \left[1 - \exp\left(\frac{p'}{N_A^-}\right)\right] \tag{3.22}$$

where N_A^- is the ionized acceptor density and p' is the screening hole density. In the case of neutral impurity scattering, hole-hole scattering has no significance because τ_N is independent of hole energy.

Thus the overal scattering relaxation time in each hole band is calculated from equations (3.3), (3.5), and (3.6) with the terms of these equations properly corrected for the effects of hole-hole scattering. Because the individual energy surfaces are different from each other, the relaxation times also differ from each other and cannot be assumed equal except in restricted ranges of temperature and dopant density [43].

3.8 Mobility in the Combined Valence Band

The conductivity mobility in each individual band is calculated from equation (3.1), *and the combined conductivity mobility in the* valance band is then evaluated as a weighted average of the single-band mobilities over the population of holes in each band, thus

$$\mu_C = \mu_1\left(\frac{m^*_{D1}}{m^*_D}\right)^{3/2} + \mu_2\left(\frac{m^*_{D2}}{m^*_D}\right)^{3/2} + \mu_3\left(\frac{m^*_{D3}}{m^*_D}\right)^{3/2} \tag{3.23}$$

Using equation (3.23) and the parameters listed in Table 3-1, we have calculated the hole mobility for silicon doped with boron, gallium, and indium as functions of dopant density and temperature, for $10^{14} \le N_A \le 10^{18}\text{cm}^{-3}$ and $100 \le T \le 400$ K. The results are displayed in Figures 3.1 through 3.6. In the calculations of mobility and resistivity in silicon doped with gallium and indium, it was assumed that boron impurities were also present. Since very pure silicon has a resistivity on the order of 1000Ω-cm, it was assumed that boron densities of 10^{13} and $5\text{x}10^{13}\text{cm}^{-3}$ existed in the gallium- and indium-doped samples, respectively. The values of these background densities were deduced from a best fit of the experimental data. For this reason, especially in the case of indium-doped silicon, the actual role of the impurities at low temperatures and/or low dopant densities is masked by the action of the always present boron impurities. As the dopant density and temperature increase, the assumed background densities of boron impurities become insignificant compared to the density of ionized dopant atoms, and Figures 3.1 through 3.6 accurately depict the influence of the particular type of impurity on the resistivity and mobility of holes in p-type silicon. The figures also show that for the case of the

Table 3-1. Values used in the calculations.

Parameter	Value	Unit
Δ	44.0	meV
a	-6.4*	eV
b	-1.36*	eV
C_ℓ^2/C_t^2	2.09*	
θ_D	735	K
ρ_s	2.329×10^3	kg/m^3
ε_s	11.7	ε_o
τ_x	6.96×10^{-10}	sec $K^{3/2}$
W	0.244	
m_o	9.1×10^{-31}	kg
h	6.25×10^{-34}	joule-sec
k_o	1.38×10^{-23}	joules/K
e	1.6×10^{-19}	coul

* These values were obtained from references [1] and [22].

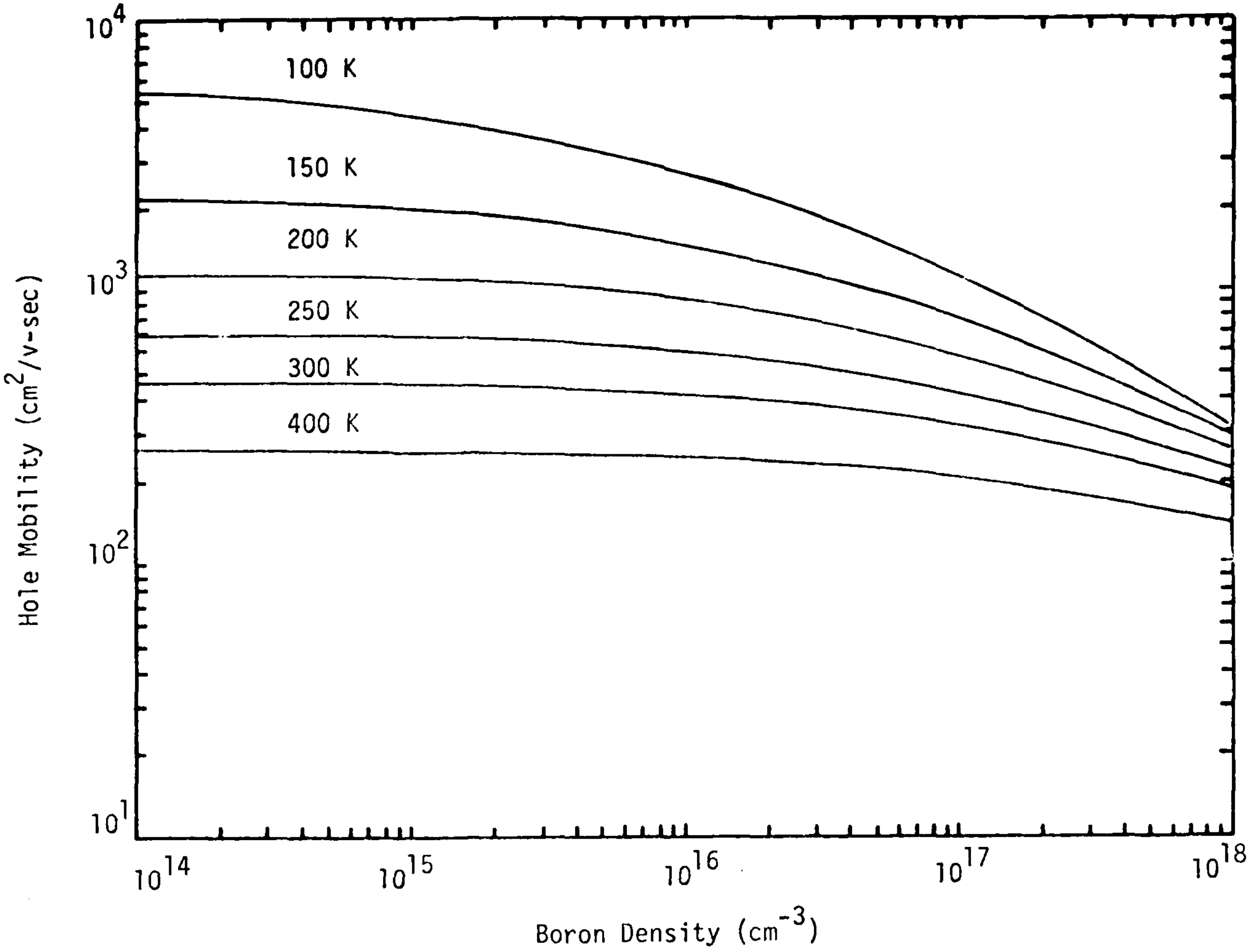

Figure 3.1. The calculated hole mobility vs dopant density for boron-doped silicon with temperature as a parameter.

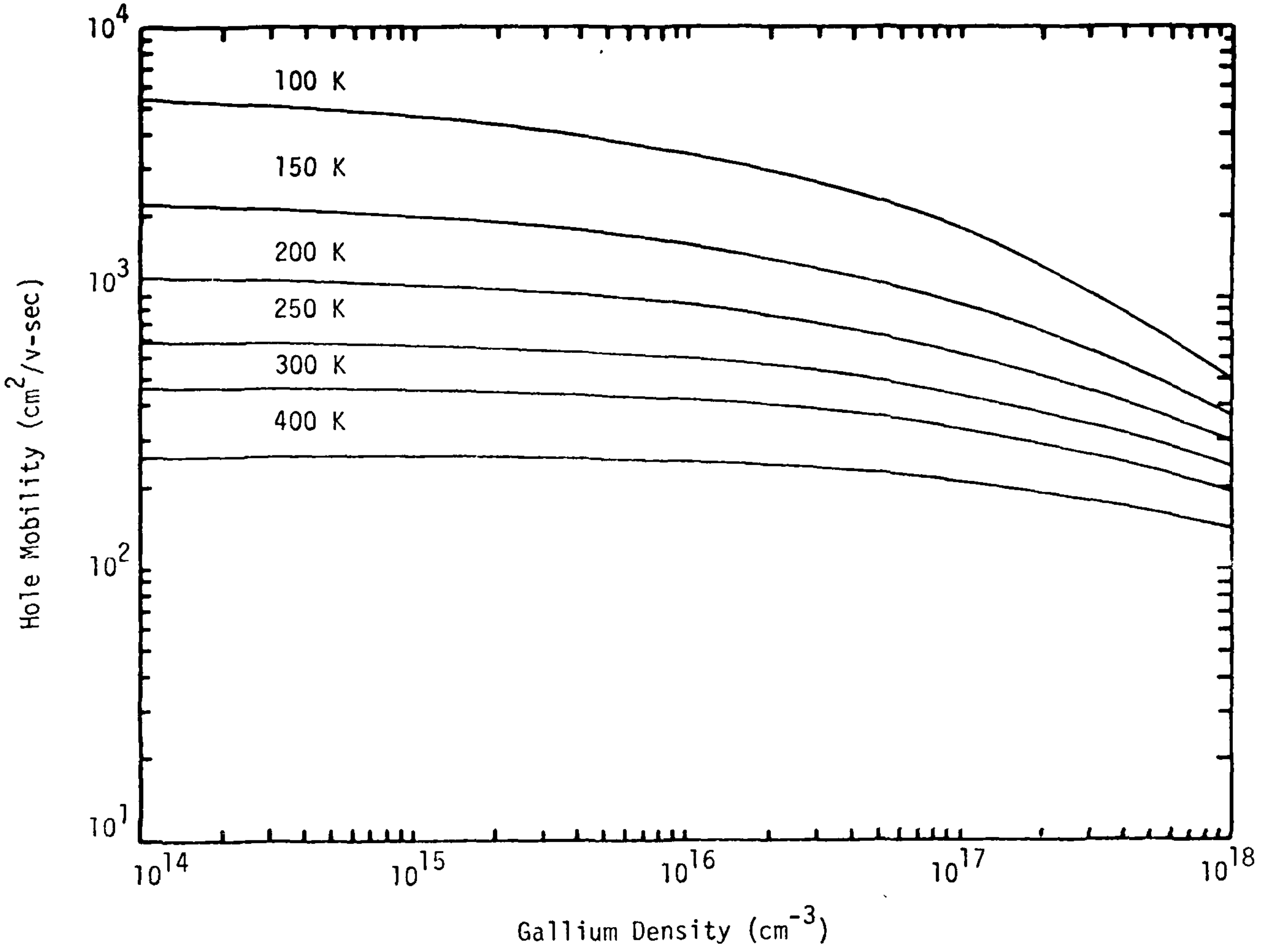

Figure 3.2. The calculated hole mobility vs dopant density for gallium-doped silicon with temperature as a parameter.

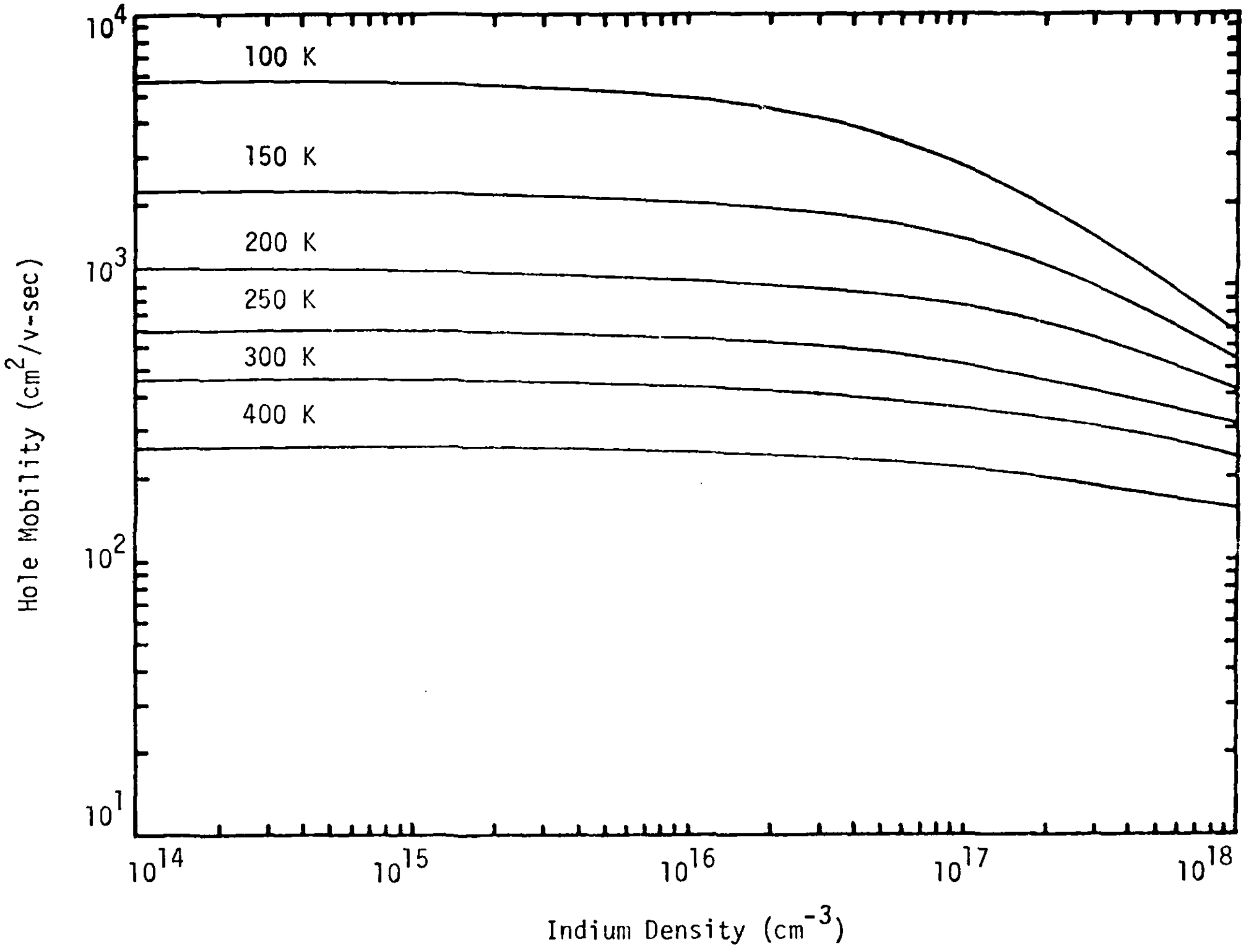

Figure 3.3. The calculated hole mobility vs dopant density for indium-doped silicon with temperature as a parameter.

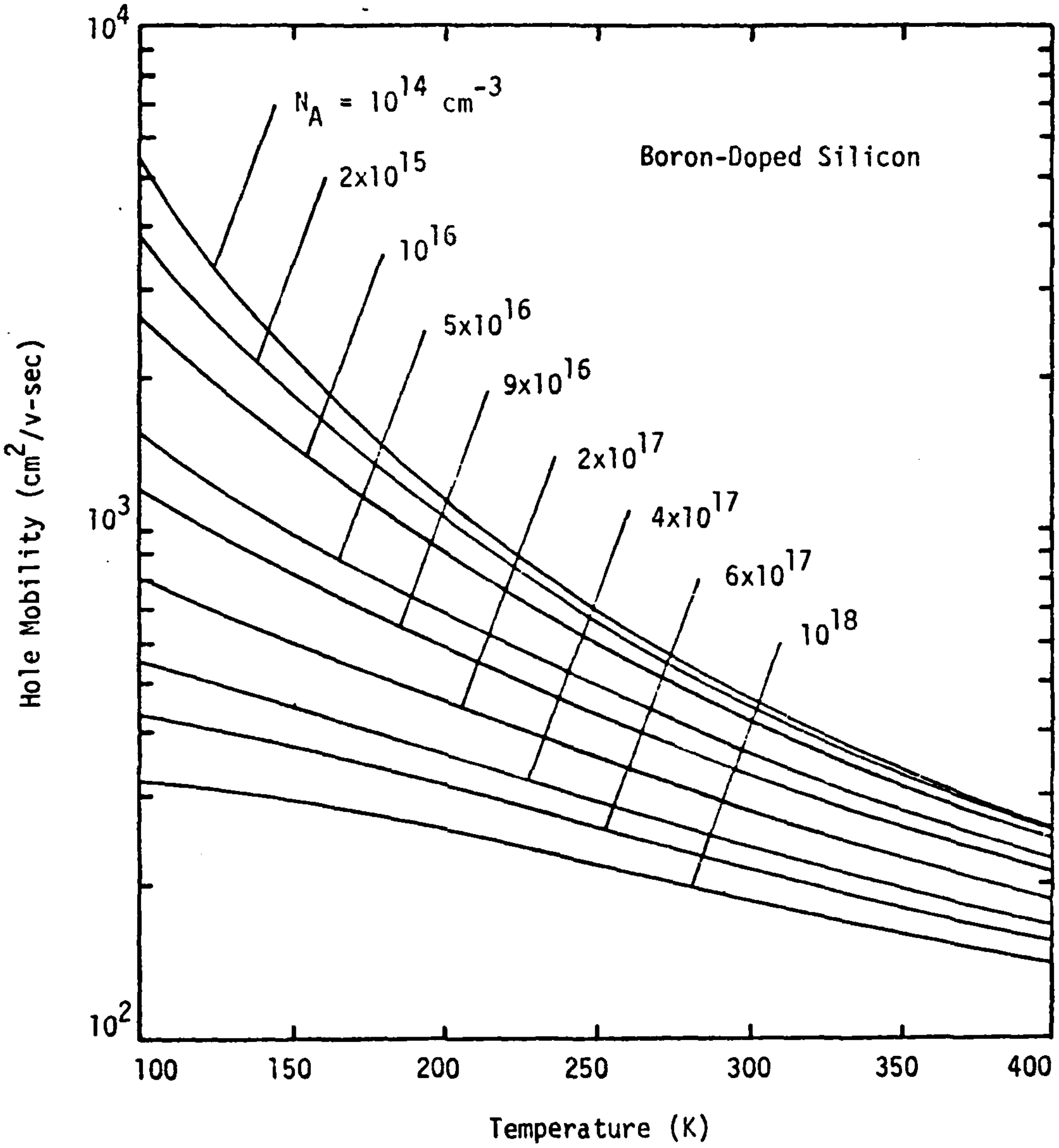

Figure 3.4. The calculated hole mobility vs temperature for boron-doped silicon with dopant density as a parameter.

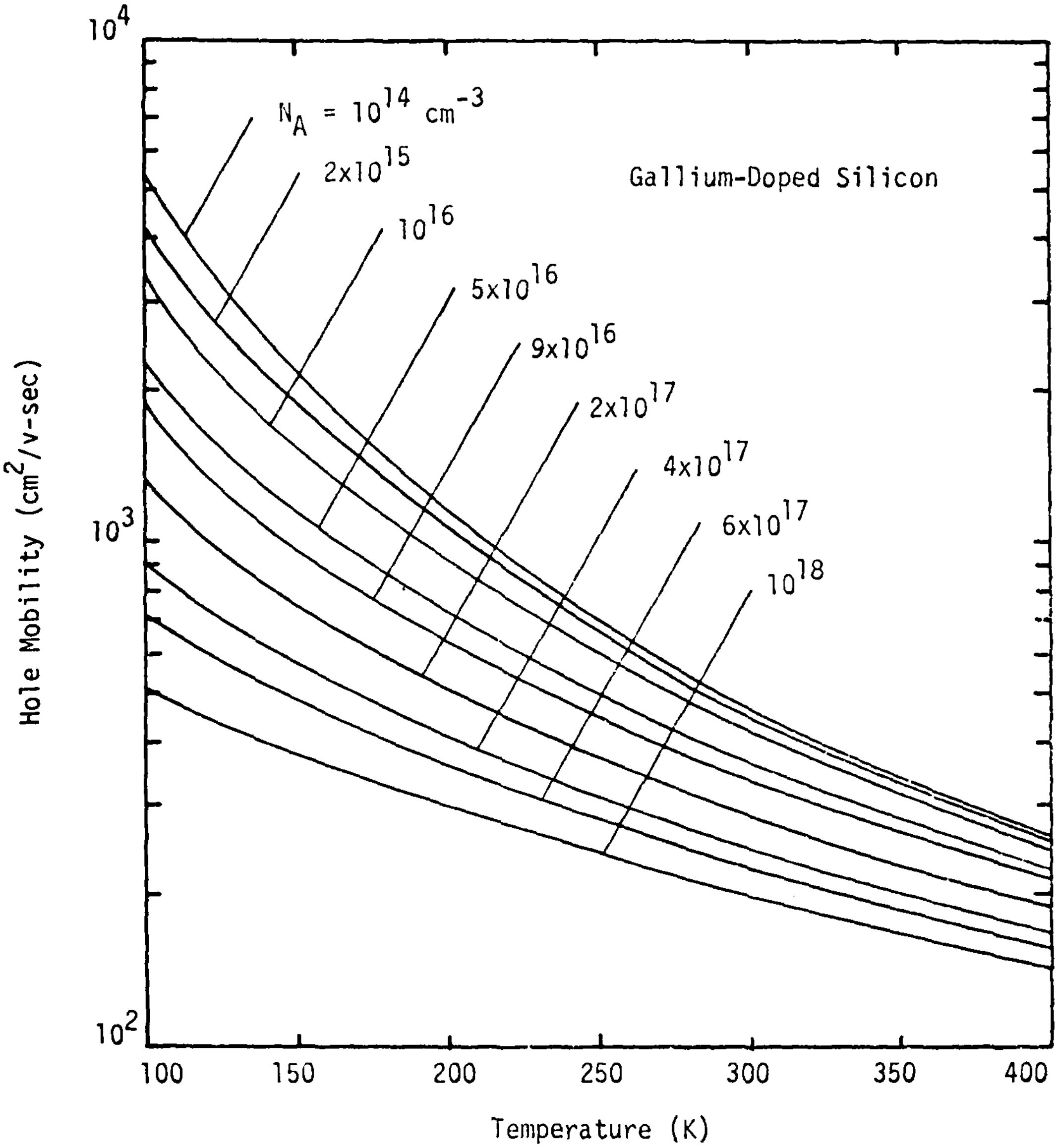

Figure 3.5. The calculated hole mobility vs temperature for gallium-doped silicon with dopant density as a parameter.

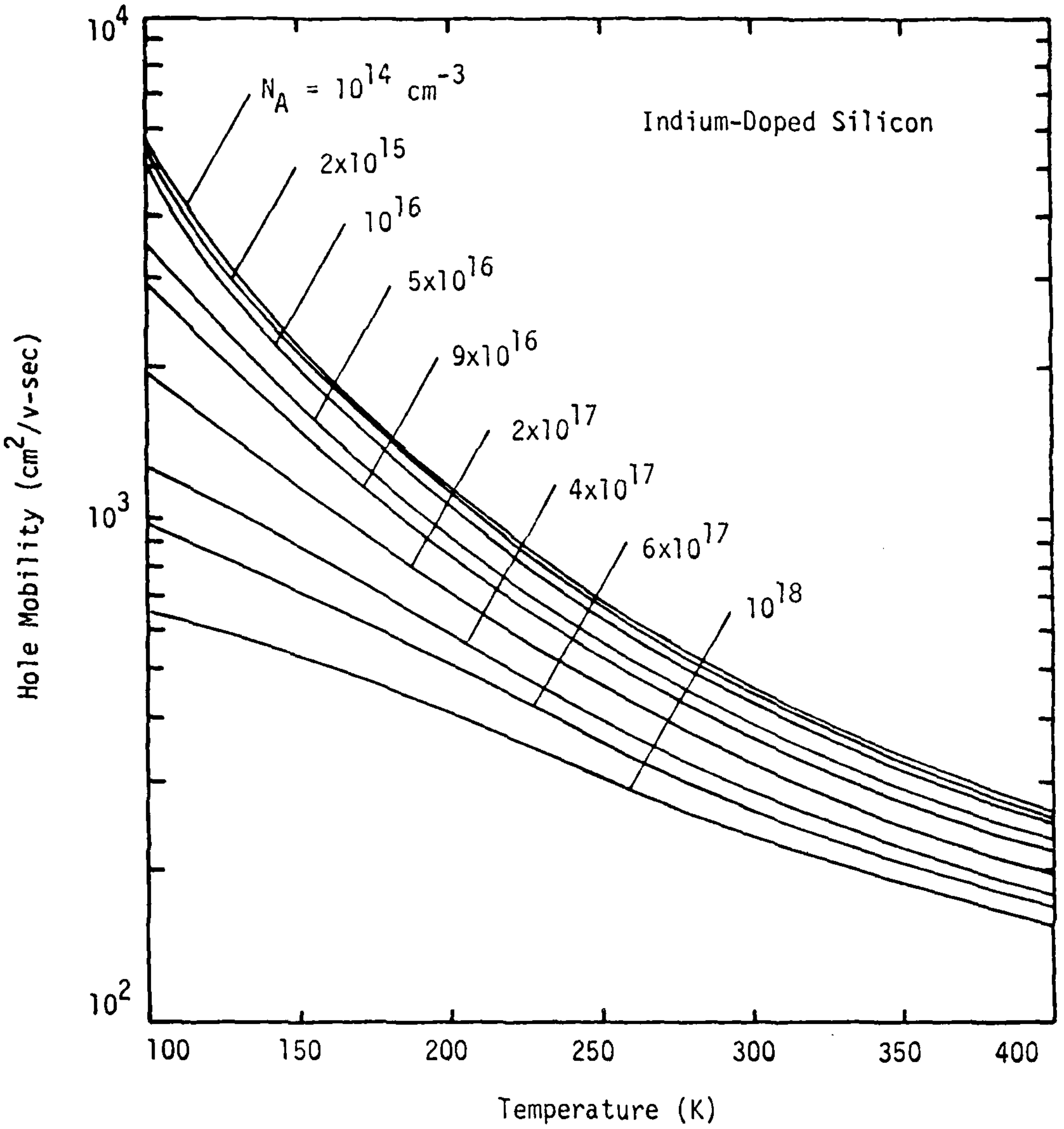

Figure 3.6. The calculated hole mobility vs temperature for indium-doped silicon with dopant density as a parameter.

shallower ionization energies, the mobility depends more strongly on temperature for the lightly-doped case where lattice scattering is dominant and become less temperature dependent as the dopant density increases.

The constant, τ_x, was found by fitting the mobility to experimental data in the lattice-scattering-limited range. Our value of τ_x is equivalent to an acoustic deformation potential constant of 8.099 eV. The optical phonon coupling constant, W, was then found by fitting the mobility to the high temperature experimental data. Our value of W is equivalent to an optical deformation potential constant of 6.024×10^8 eV/cm.

CHAPTER IV

HOLE DENSITY AND RESISTIVITY

4.1 Introduction

The resistivity of semiconductor materials is one of their most useful and easily measured properties. Theoretical calculations of resistivity depend on the formulation of conductivity mobility, and the determination of hole density. For extrinsic semiconductors, the hole density is determined primarily by the percentage of ionization of impurity atoms. The following sections discuss the dependence of hole density and resistivity on temperature and dopant density.

4.2 Ionization of Impurity Atoms

For the case of Fermi-Dirac statistics, the hole density is given by

$$p = \frac{4}{\sqrt{\pi}}\left[\frac{2\pi k_o T m_D^*}{h^2}\right]^{3/2} F_{\frac{1}{2}}(\eta) \qquad (4.1)$$

where, m_D^*, the density-of-states effective mass, contains information pertaining to the nonparabolic nature of the valence band. In the limit of low dopant densities, equation (4.1) reduces to

$$p = N_V \exp(\eta) \qquad (4.2)$$

where $N_V = 2(2\pi m_D^* k_o T/h^2)^{3/2}$ is the effective density of valence band states. For the range of temperatures considered in this study, the hole density is calculated by assuming that the density of carriers is determined by the impurities present in the silicon sample. The density of ionized acceptor impurities in p-type silicon is computed from the charge neutrality equation

$$N_A^- - N_D^+ = p - n \tag{4.3}$$

This reduces to

$$p \simeq N_A^- \tag{4.4}$$

for the case of uncompensated material.

The density of ionized acceptors is [56]

$$N_A^- = \frac{N_A}{1 + g \exp\left(\frac{E_A - E_F}{k_o T}\right)} \tag{4.5}$$

where E_A is the acceptor ionization energy, and g is the ground state degeneracy. Excited states have a very minor influence on the carrier concentration due to the large separation between the ground state and the excited states [1,56]. Letting

$$g = 4 + 2 \exp\left(- \frac{\Delta}{k_o T}\right) \tag{4.6}$$

enables us to include the contribution of the split-off band [17]. The density of ionized acceptors is computed by iterating E_F in equations (4.2) and (4.5) until equation (4.4) is fulfilled within a given level of accuracy.

Experimental evidence shows that the acceptor ionization energy E_A is not a constant, but decreases with increasing dopant density [9]. Penin et al. [57] have determined in a study of heavily doped silicon from 4 to 300 K that for shallow impurities such as boron and phosphorus the ionization energy decreases and finally disappears altogether for impurity densities greater than $3x10^{18}$ cm^{-3}. For impurities with deeper activation energies, it is also expected that at some impurity concentration, the impurity activation energy should become a function of the impurity concentration. However, in the case of gallium and indium, this should happen at higher impurity concentrations than for the shallower level impurities. This is due to the smaller geometrical dimensions of the wave functions applicable to the deeper levels, so that overlapping effects which promote the reduction in activation energy require higher impurity concentrations [14]. For shallow impurities such as boron and phosphorus, empirical expressions [9,57] relating the dependence of ionization energy to dopant density have been established. In the case of Ga, there is data [15] on activation energy vs concentration, but not enough on which to base an accurate relationship. For this reason the value of E_A = 0.056eV was used. For In, E_A = 0.156eV [58] was used. Figures 4.1 through 4.3 show the ratio of ionized and total impurity density as a function of impurity density with temperature as a parameter for $100 \le T \le 400$ K for silicon doped with boron, gallium, and indium. It is clearly shown in these figures that the ionization of impurities for the deeper levels is significantly lower even at low dopant densities so that it is necessary to go to higher

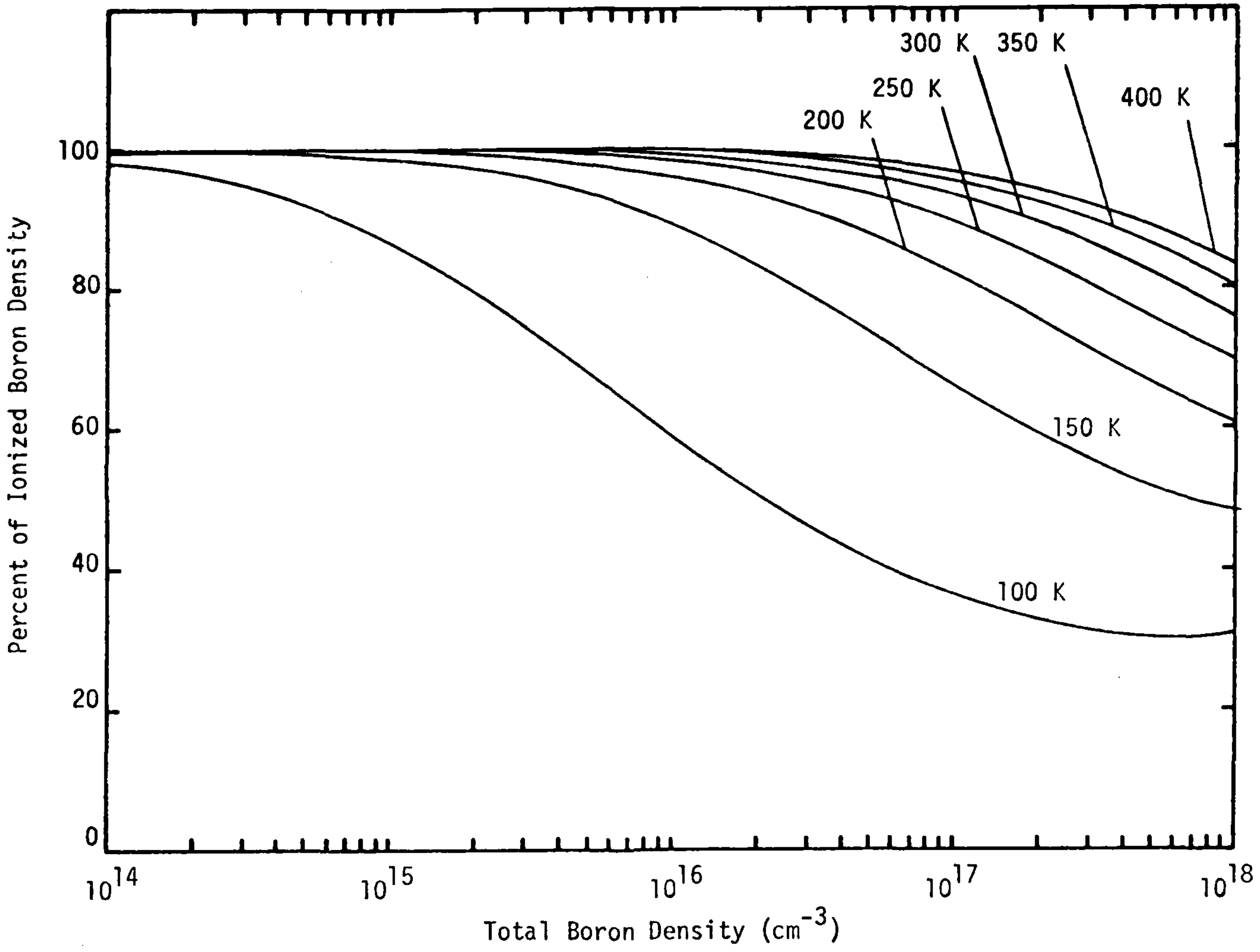

Figure 4.1. Theoretical calculations of the ratio of ionized and total boron density vs boron density with temperature as a parameter.

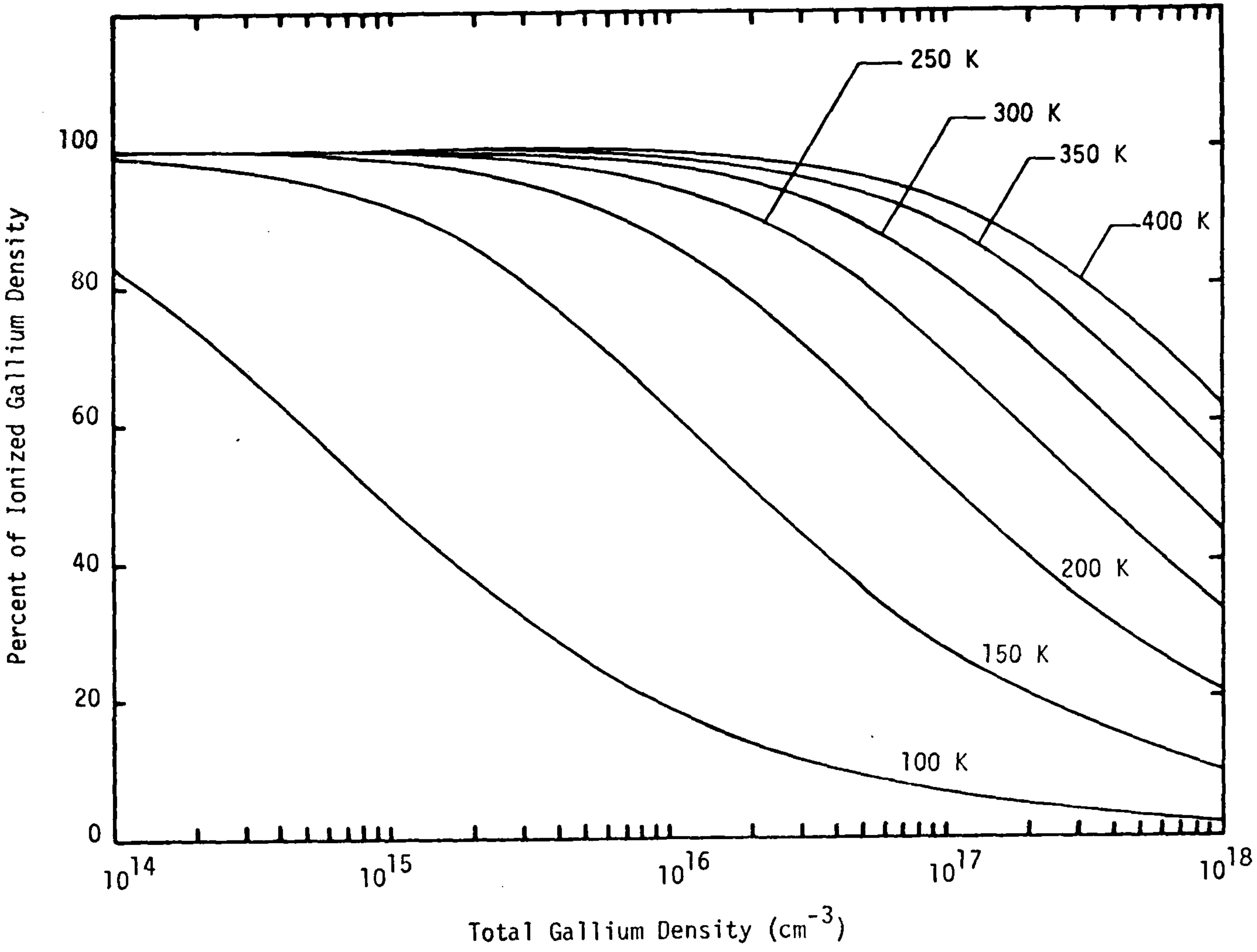

Figure 4.2. Theoretical calculations of the ratio of ionized and total gallium density vs gallium density with temperature as a parameter.

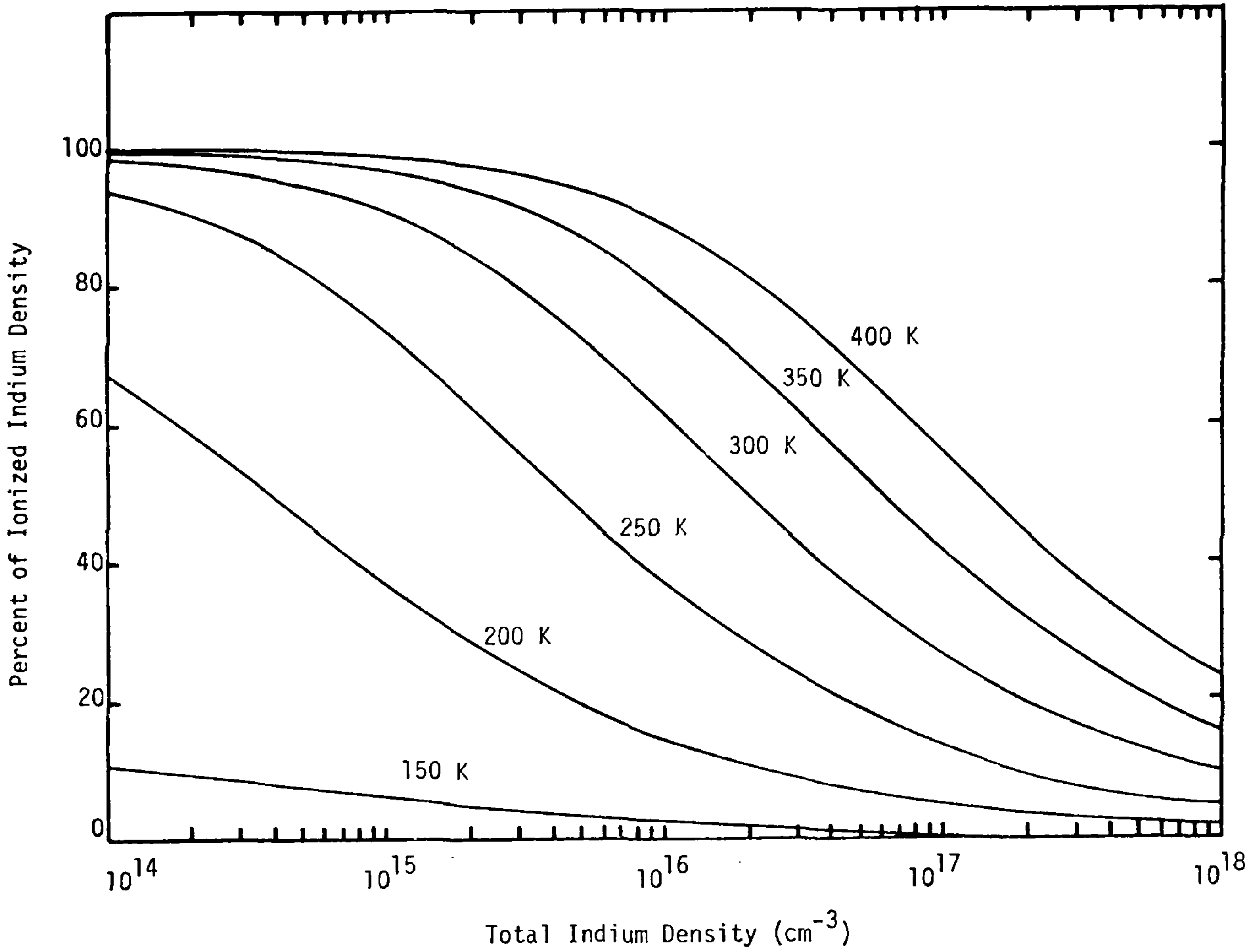

Figure 4.3. Theoretical calculations of the ratio of ionized and total indium density vs indium density with temperature as a parameter.

temperatures to achieve total ionization of impurities. The deionization of impurities is most significant for low temperatures and high impurity densities.

4.3 Resistivity of p-Type Silicon

The resistivity of p-type silicon is given by

$$\rho = \frac{1}{e\mu_C p} \tag{4.7}$$

where μ_C is the hole conductivity mobility calculated from equation (3.23) and p is the hole density discussed in Section 4.2. Equation (4.7) was used to calculate the hole resistivity for silicon doped with boron, gallium, and indium as a function of dopant density and temperature, for $10^{14} \le N_A \le 10^{18}$ cm^{-3} and $100 \le T \le 400$ K. The results are displayed in Figures 4.4 through 4.9. In the calculations of resistivity in silicon doped with gallium and indium, as was done for conductivity mobility, it was assumed that boron impurities were also present. Boron densities of 10^{13} and 5×10^{13} cm^{-3} were assumed to exist in the gallium- and indium-doped samples, respectively. The values of these background densities were deduced from a best fit of the experimental data. As the dopant density and temperature increase, the assumed background densities of shallow impurities becomes insignificant compared to the density of ionized dopant atoms, and Figures 4.4 through 4.9 accurately depict the influence of the particular type of impurity on the resistivity of holes in p-type silicon. The figures also show that for the case of the shallower ionization energies, resistivity depends more strongly on temperature for the lightly doped case where lattice scattering is dominant and become less temperature dependent as the dopant density increases.

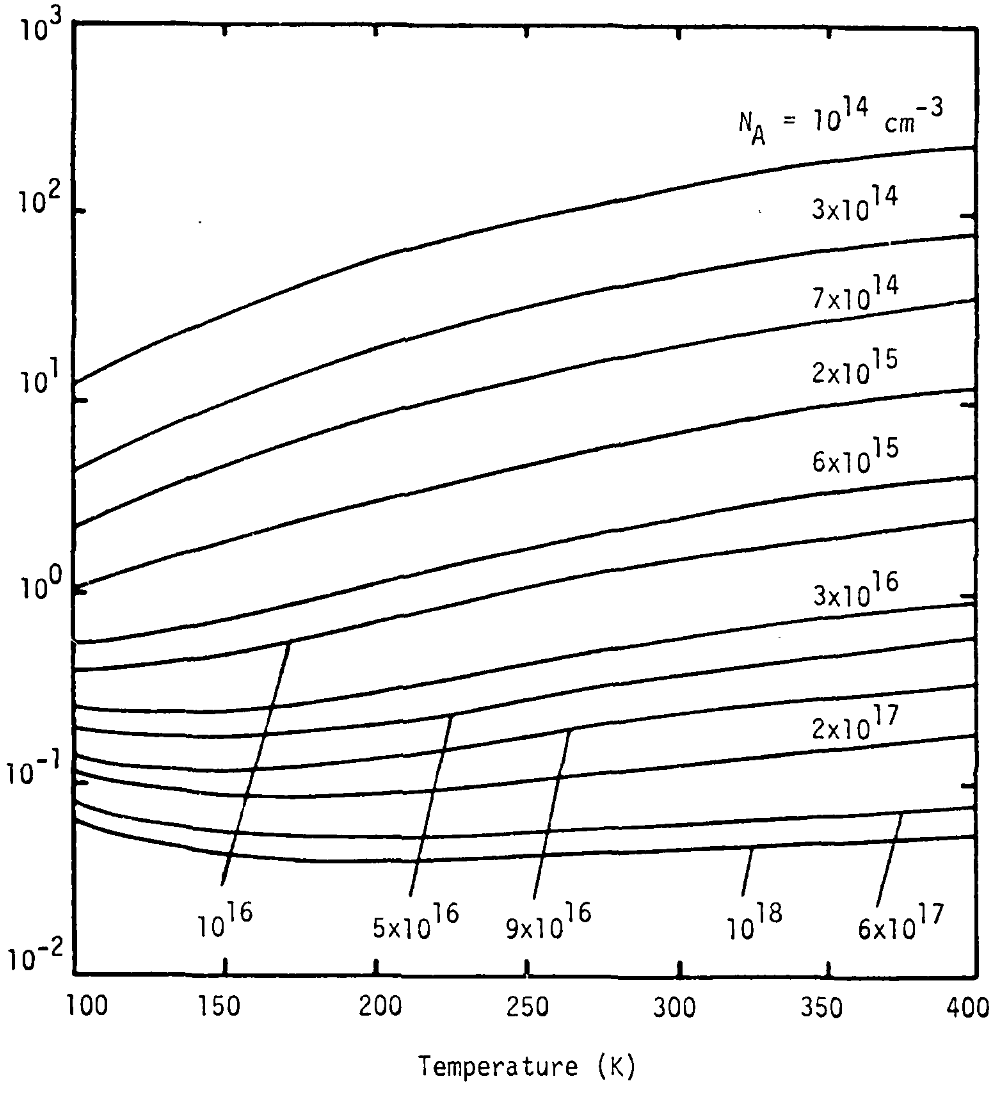

Figure 4.4. Theoretical calculations of resistivity vs temperature for boron-doped silicon with dopant density as a parameter.

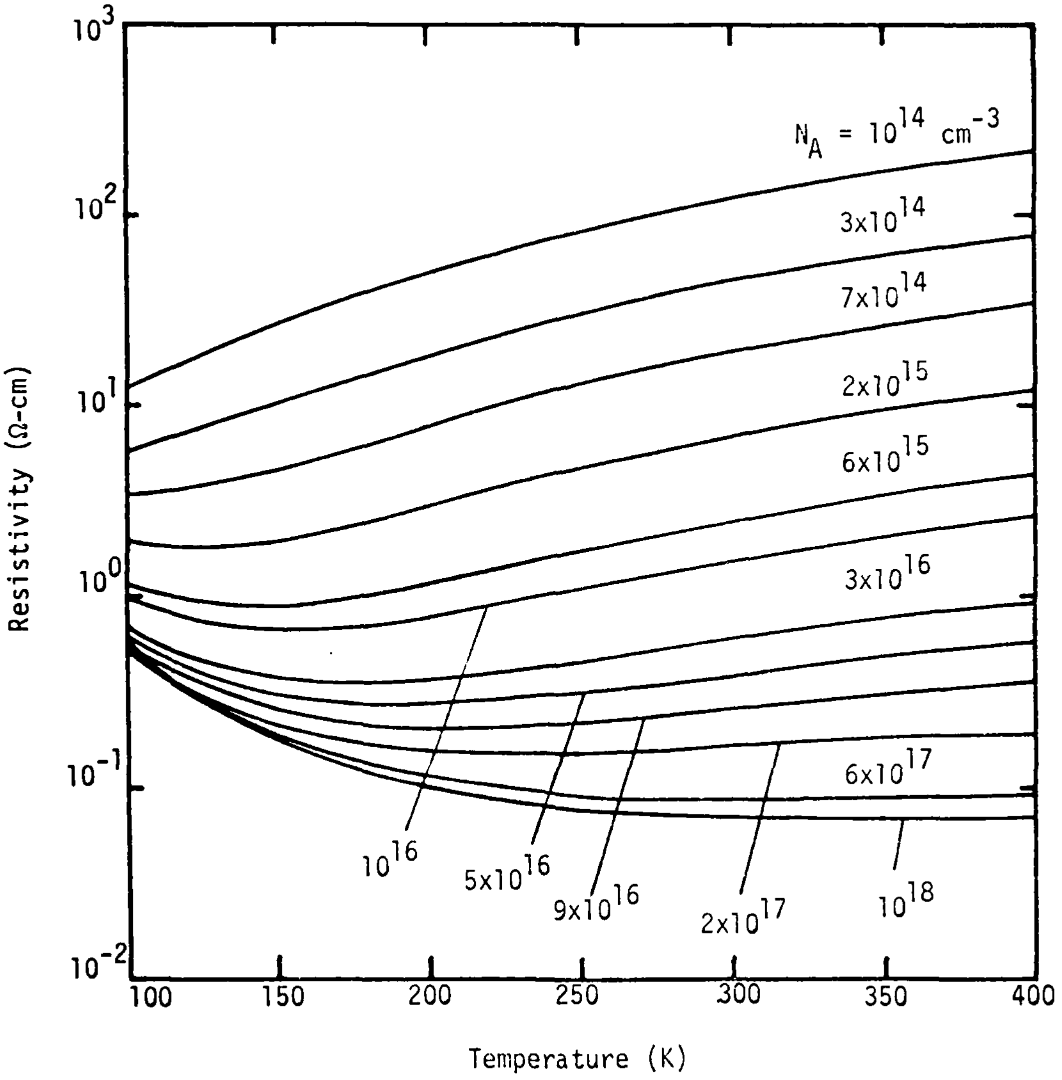

Figure 4.5. Theoretical calculations of resistivity vs temperature for gallium-doped silicon with dopant density as a parameter.

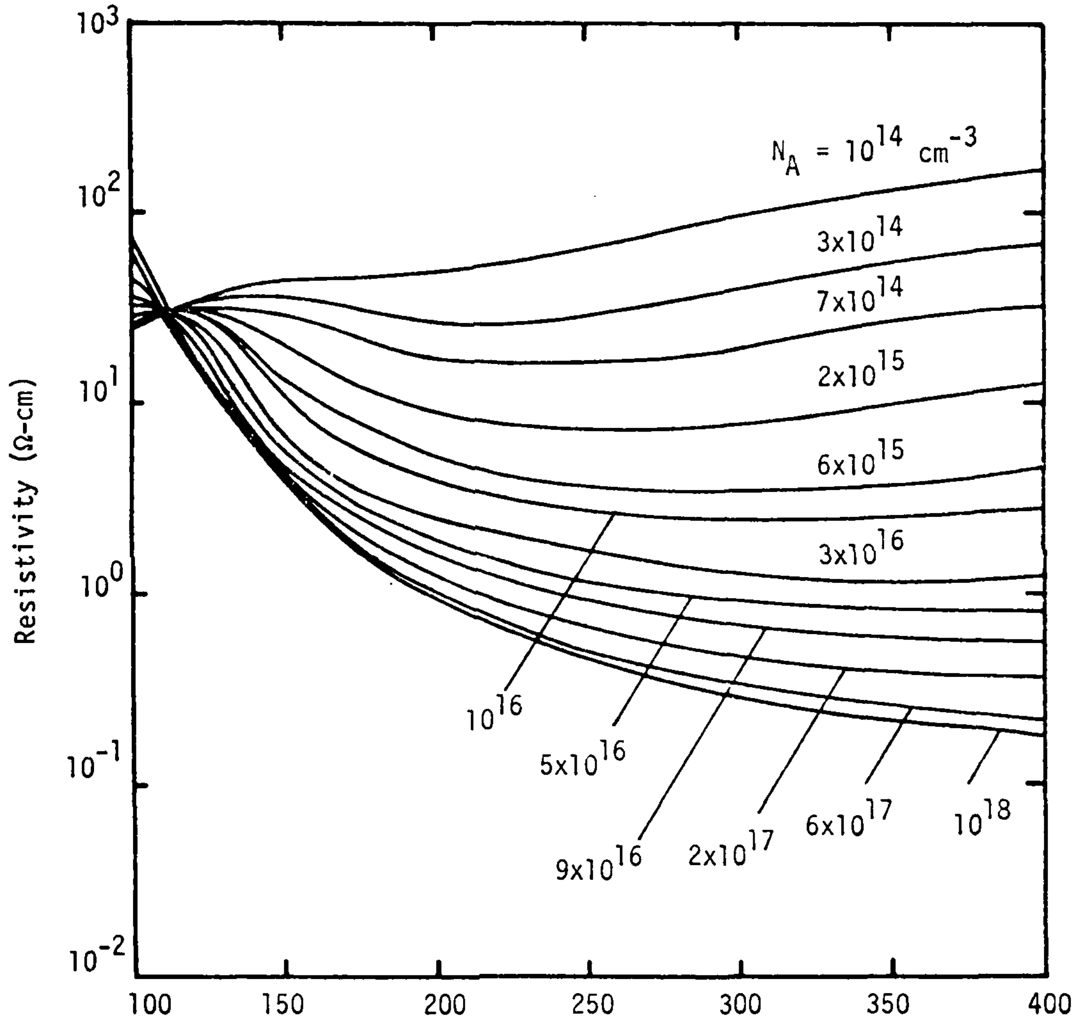

gure 4.6. Theoretical calculations of resistivity vs temperature for indium-doped silicon with dopant density as a parameter.

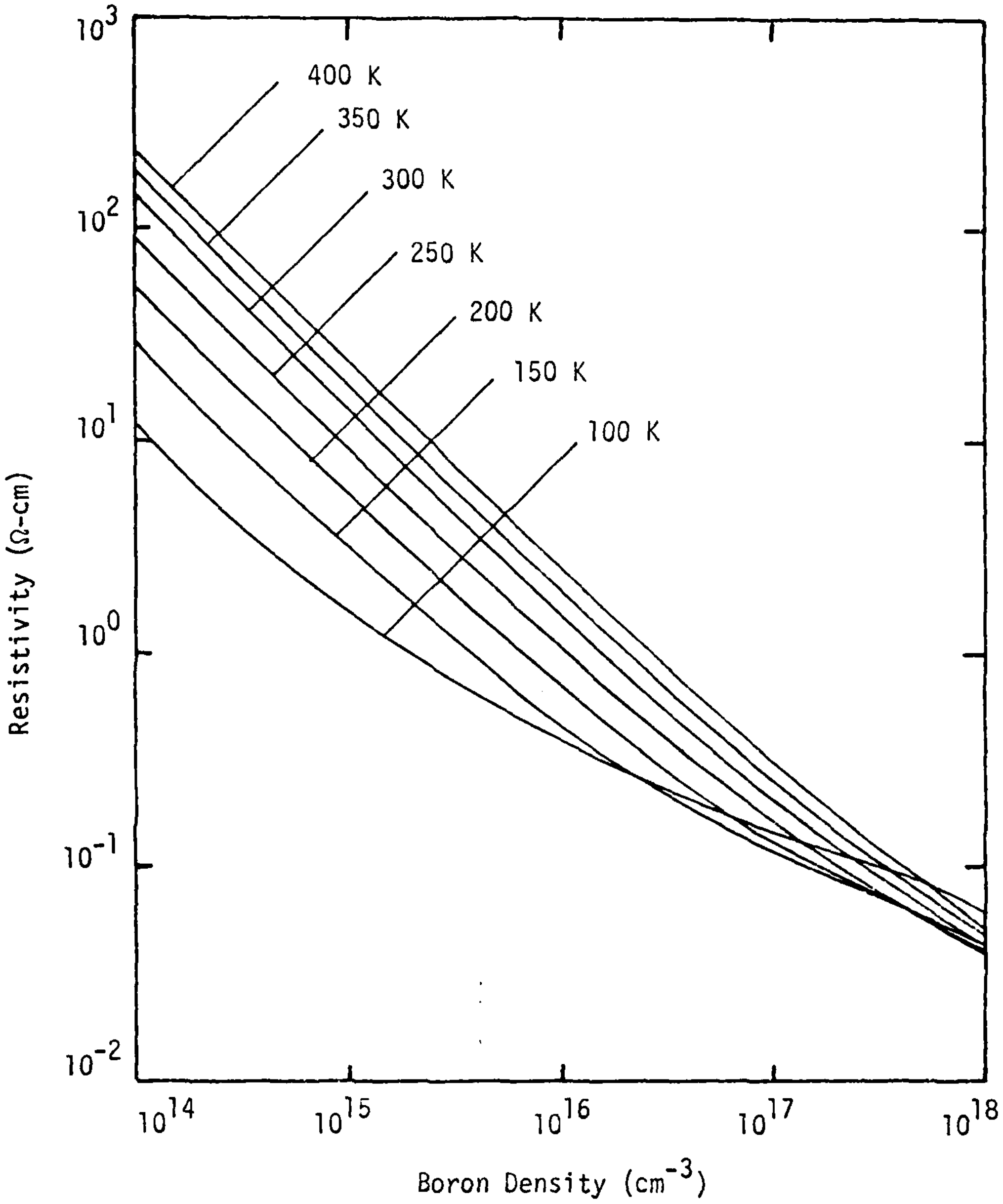

Figure 4.7. Theoretical calculations of resistivity vs dopant density for boron-doped silicon with temperature as a parameter.

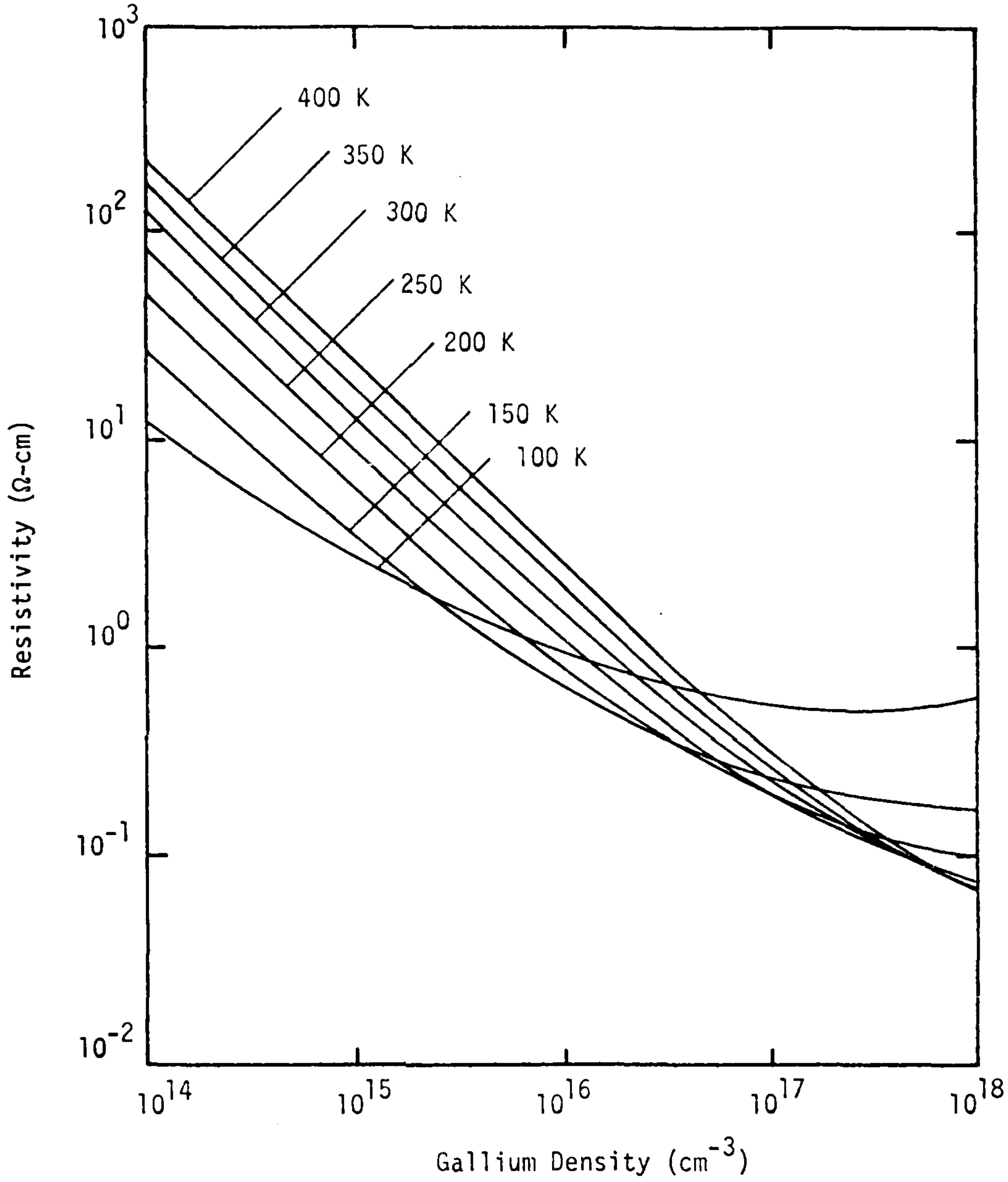

Figure 4.8. Theoretical calculations of resistivity vs dopant density for gallium-doped silicon with temperature as a parameter.

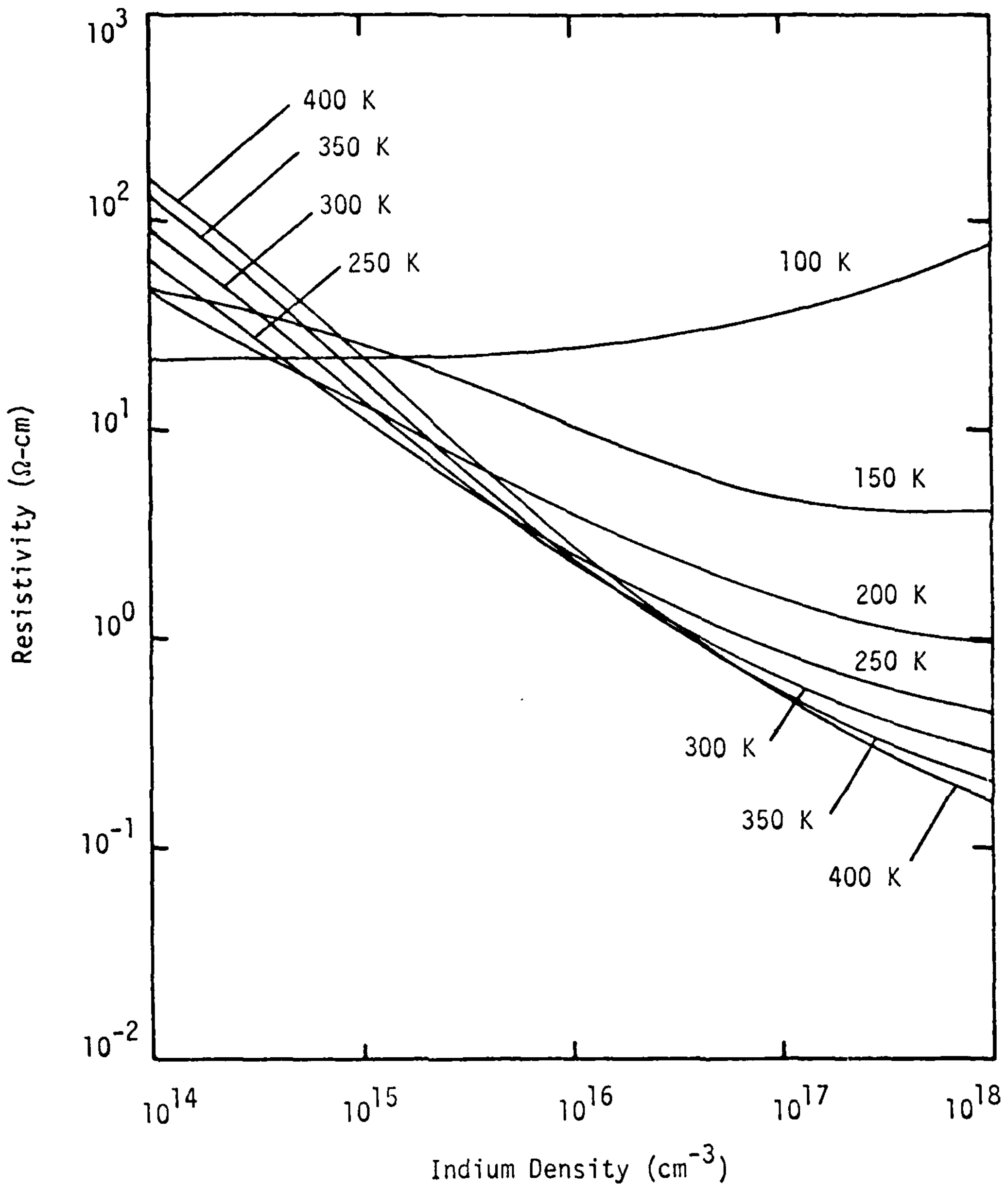

Figure 4.9. Theoretical calculations of resistivity vs dopant density for indium-doped silicon with temperature as a parameter.

CHAPTER V

THE HALL FACTOR IN p-TYPE SILICON

5.1 Introduction

The most direct determination of the mobility is by the Haynes-Schokley drift method, wherein the drift of charge carriers in a known electric field is measured. However, the assumption, made when these experiments were initiated, that the drift mobility of holes as minority carriers in an n-type sample is the same as when they constitute the majority carriers, is invalid in view of carrier-carrier scattering [59]. Also the experiment can succeed only if the lifetime of the minority carriers is larger than the transit time. For this reason, usually Hall mobilities are measured instead. The Hall mobility is the product of the measured conductivity and the measured Hall coefficient. In general the Hall mobility differs from the conductivity mobility by a factor called the Hall factor. Determination of the Hall factor may be avoided by making use of the high field limit. For sufficiently high magnetic fields several simplifications occur in the magnetic field dependence of the Hall coefficient. In the high-field limit (when the product of mobility and magnetic induction becomes greater than 10^8 cm^{-2} gauss/volt-sec [60]) the Hall coefficient is simply related to the carrier concentration by [61]

$$R_H = \frac{1}{pe} \tag{5.1}$$

and thus the conductivity mobility and the Hall mobility are equal. Although the high field limit simplifies use of the Hall mobility considerably, excessively high magnetic fields can cause problems due to the quantization of the hole orbits in a magnetic field [1]. The quantization of the particle motion in a magnetic field will create Landau levels within the band. The Landau levels will modify the density of states in the valence band which could affect the interpretation of experimental data [56]. Another high magnetic field effect of importance is the "magnetic freeze out" which occurs with the stronger localization of bound state wave-functions in a strong magnetic field [62]. Due to the more localized charge distribution, the Coulomb binding energy of the impurity state is increased so that at a fixed temperature the concentration of thermally excited charge carriers will be smaller and the Hall coefficient will be effectively increased.

Thus, in order to avoid these high field region complications and obtain an experimental determination of the value of conductivity mobility in the low field limit, it is necessary to have an accurate knowledge of the Hall factor with which to modify measured Hall mobilities. Hall measurements are routinely used to experimentally determine the density of ionized impurities in a semiconductor sample. This determination is possible only if an accurate value of the Hall factor for the particular temperature and dopant density considered is available.

5.2 The Hall Factor

The Hall and conductivity mobilities are related by the Hall factor as follows:

$$r_H = \frac{\mu_H}{\mu_C} \tag{5.2}$$

For nondegenerate, spherically symmetric bands, it can be shown that [59] $r_H \geq 1$, and that

$$r_H = \frac{\langle\tau^2\rangle}{\langle\tau\rangle^2} \tag{5.3}$$

In general most previous work [5,59] has assumed that equation (5.3) is valid in the case of p-type silicon and thus r_H will vary between 1.18 ($\tau(E) \propto E^{-1/2}$ for lattice scattering) and 1.93 ($\tau(E) \propto E^{3/2}$ for ionized impurity scattering), if hole-hole scattering is neglected, and will approach unity for the degenerate case. This theory does not allow for values of r_H less than one. Experimental evidence indicating values of r_H less than one has been attributed to poor quality of the measured samples [5]. Debye and Kohane [63] found that the measured drift mobility for holes is considerably larger than the measured Hall mobility. Values of r_H less than unity were also reported by Wolfstirn [15] for the case of gallium-doped silicon. More recent experiments [64] show that a value of r_H less than unity is necessary to reconcile differences between the hole concentration measured via Hall coefficient methods and that inferred from dopant densities determined from C-V and junction breakdown measurements. The usual assumption made is to let r_H be equal to one and thus consider the Hall mobility equal to the conductivity mobility. Neglecting the Hall scattering factor alters both the magnitude and temperature dependence of the carrier concentration from that given by the charge balance equation. In fitting data to the charge balance equation, both thermal carrier concentration and dopant impurity activation energy are overestimated by the assumption of unity Hall factor. A more complete theoretical treatment of the Hall factor can be undertaken by considering the nonparabolic and anisotropic nature of the valence band of silicon.

Chapter II described the constant energy surfaces as warped spheres. Warping of the energy surfaces has a significant effect on the ratio of Hall to conductivity mobility. When the bands are warped, the Hall factor depends on the degree of warping as well as the scattering mechanism [30].

The Hall mobility is the product of the ohmic conductivity and the Hall coefficient

$$\mu_H = \sigma_C R_H \tag{5.4}$$

In the low field limit the Hall coefficient for a nonparabolic, anisotropic band i is given by [37]

$$R_{Hi} = \frac{\sigma_{Hi}}{\sigma_{Ci}^2} \tag{5.5}$$

Thus by substituting equations (2.9) and (2.10) into equation (5.5) the Hall coefficient can be expressed as

$$R_{Hi} = \frac{r_{Hi}}{p_i e} \tag{5.6}$$

where

$$r_{Hi} = \left(\frac{m^*_{Ci}}{m^*_{Hi}}\right)^2 \left(\frac{<\tau_i^2>}{<\tau_i>^2}\right) \tag{5.7}$$

is the Hall factor. We see that allowing for a difference between the values of conductivity and Hall effective masses due to the anisotropic, nonparabolic nature of the band, enables us to separate the Hall factor into two components: the mass anisotropy factor given by

$$r_{Ai} = \left(\frac{m^*_{Ci}}{m^*_{Hi}}\right)^2 \tag{5.8}$$

and the scattering factor given by

$$r_{Si} = \frac{<\tau_i^2>}{<\tau_i>^2} \tag{5.9}$$

These components of the Hall factor will be considered in detail in the next two sections.

5.3 The Mass Anisotropy Factor

Lax and Mavroides [20] have derived expressions for r_A based on the Dresselhaus et al [28] model of the valence band of germanium and silicon. Their formulation for r_A acknowledges the anisotropy, but neglects the nonparabolicity of the bands. In general it is found that r_A is less than unity unless the scattering anisotropy becomes extreme [30]. In order to determine the variation of the mass anisotropy factor with changes in temperature and dopant density for the combined valence band of silicon, equation (5.8) was evaluated using the values of combined valence band effective mass obtained from equations (2.28) and (2.29).

The results of this calculation are presented in Figures 5.1 and 5.2. These figures show the significant contribution of the mass anisotropy factor to the Hall factor. Since the influence of nonparabolicity is reduced in degenerate material [25], it follows as shown in Figures 5.1 and 5.2, that the variation of r_A with temperature is much stronger at low dopant densities, since it is in this dopant density range that the variation of effective mass with temperature is the strongest. We note that the mass anisotropy factor is less than unity for all temperatures considered in this work once the dopant density increases past 6×10^{15} cm^{-3}. At 300 K, r_A is less than unity even for dopant densities as low as 10^{14} cm^{-3}.

5.4 The Scattering Factor

The scattering factor, r_S, depicted in Figures 5.3 and 5.4 as a function of temperature and dopant density, does not follow the traditionally expected variation between $3\pi/8 = 1.18$ and $315\pi/512 = 1.93$ as the dominant scattering mechanism changes from lattice to ionized impurity scattering. Putley [65] has noted that hole-hole scattering can modify r_S. He estimates that for ionized impurity scattering, r_S can be reduced from $315\pi/512$ to a value close to unity. At low dopant densities where the dominant scattering mechanism is acoustic phonon scattering, r_S varies between 1.08 for T = 100, to 1.24 for T = 400 K. The deviation from the traditionally expected value of $r_S = 1.18$ is due to the contributions of optical phonon modes at the higher temperatures. Hole-hole collisions also affect the impurity and optical phonon scattering contributions so they become significant even at low temperatures and dopant densities. At higher values of dopant density, the effects of hole-hole scattering on the ionized impurity scattering mechanism

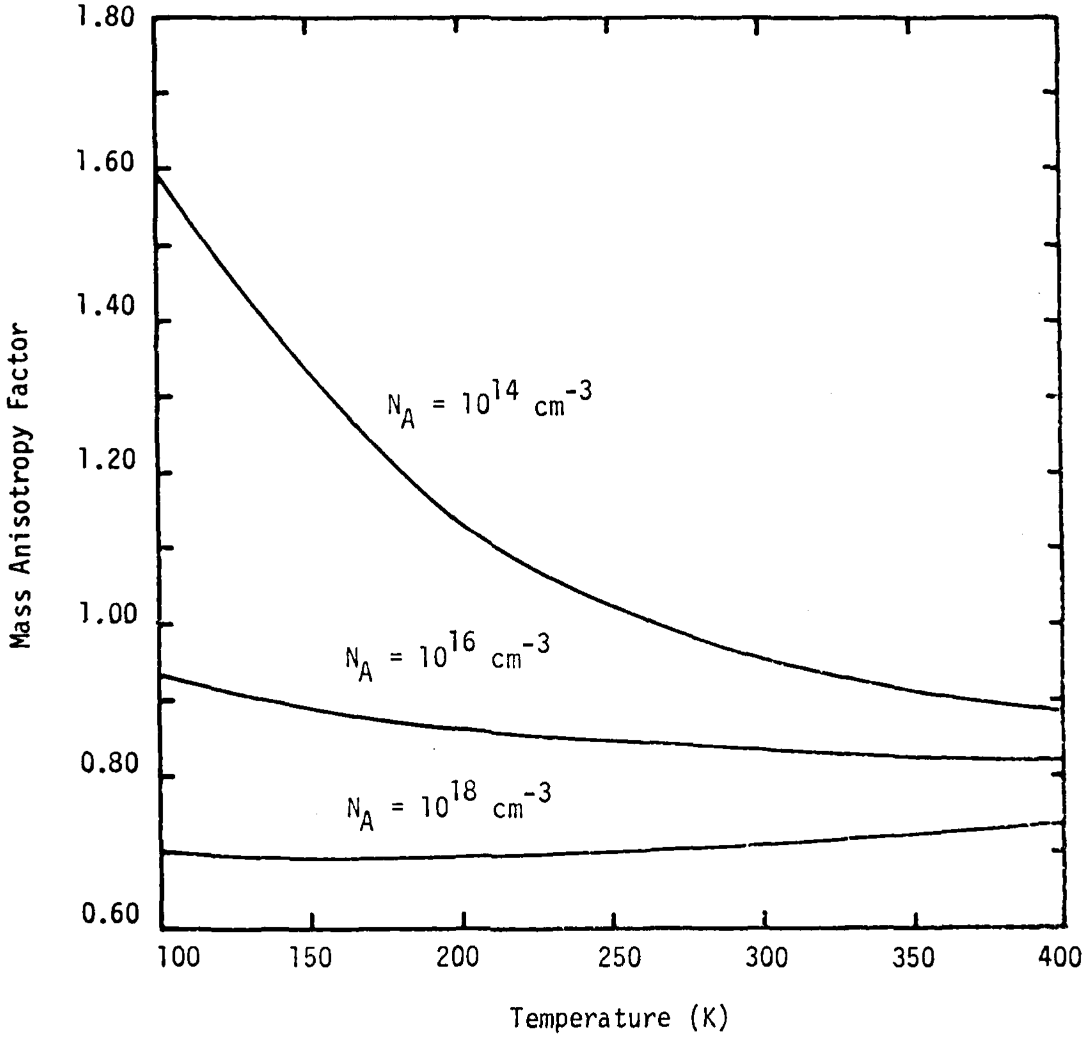

Figure 5.1. The mass anisotropy factor r_A as a function of temperature for various impurity dopant densities.

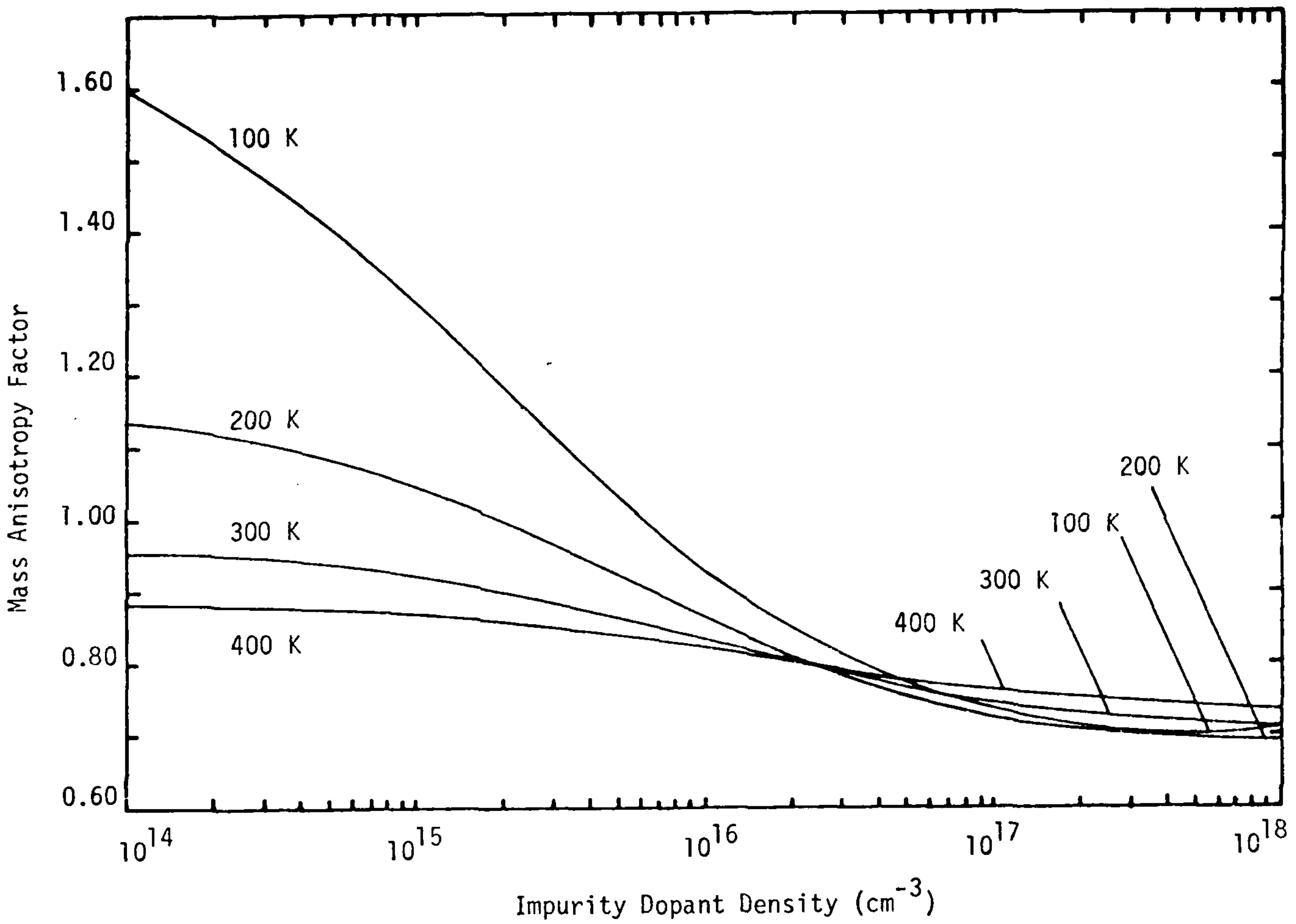

Figure 5.2. The mass anisotropy factor r_A as a function of impurity dopant density for various temperatures.

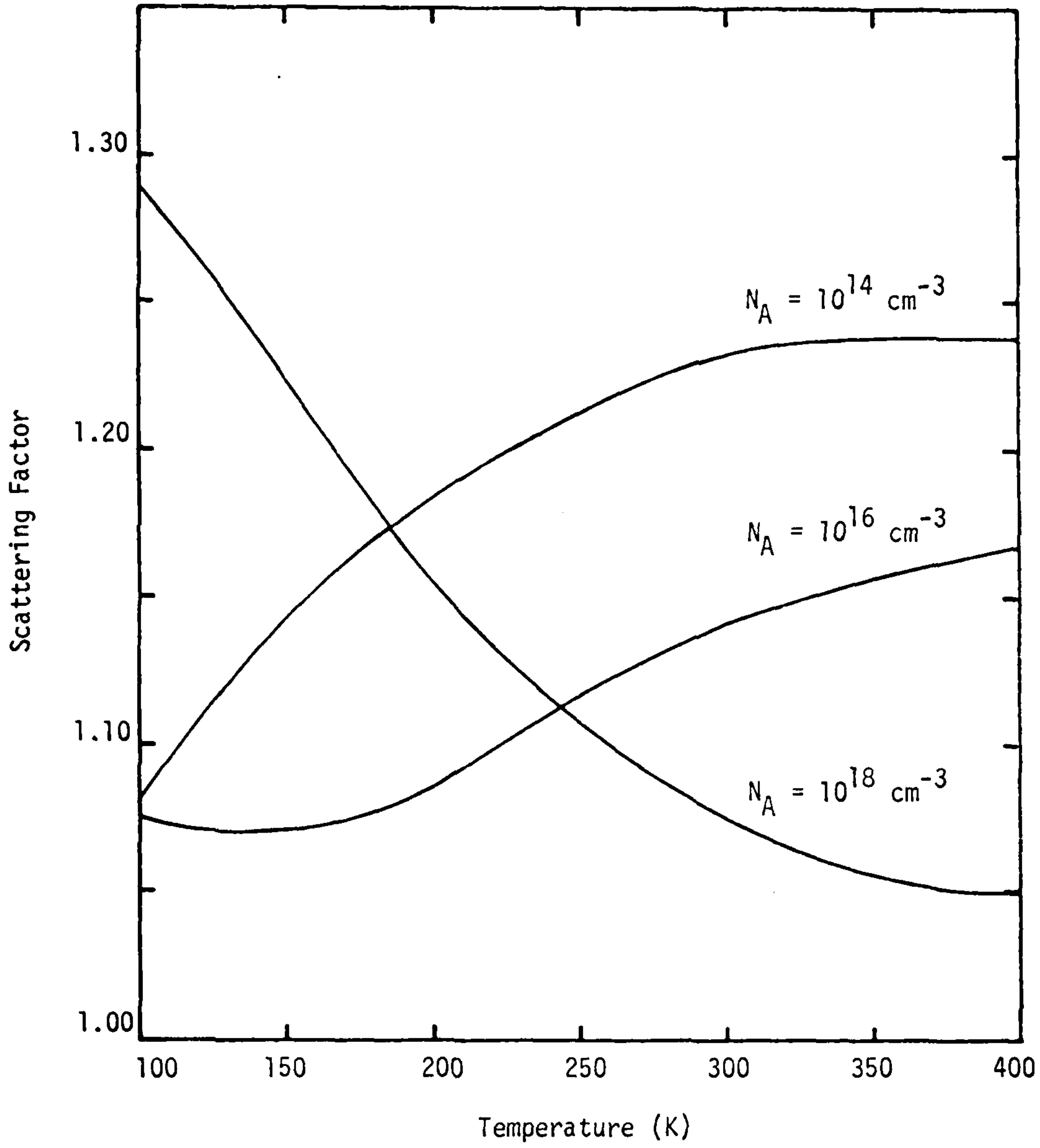

Figure 5.3. The scattering factor r_S as a function of temperature for boron-doped silicon with dopant density as a parameter.

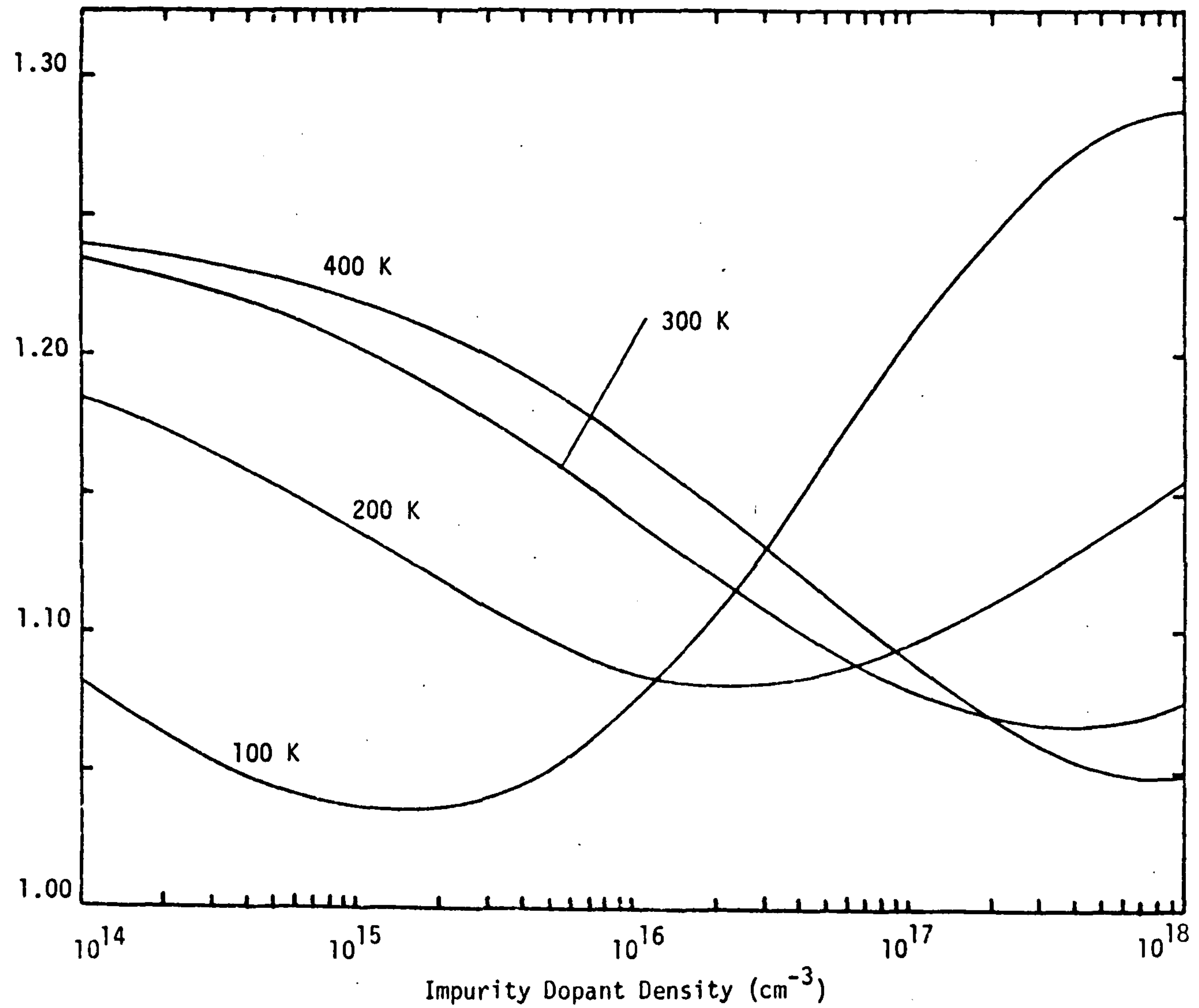

Figure 5.4. The scattering factor r_S as a function of dopant density for boron-doped silicon with temperature as a parameter.

AD-A091 310 AIR FORCE INST OF TECH WRIGHT-PATTERSON AFB OH F/G 20/12
THE MOBILITY, RESISTIVITY AND CARRIER DENSITY IN P-TYPE SILICON--ETC(U)
AUG 79 L C LINARES
UNCLASSIFIED AFIT-CI-79-232D NL

2 OF 2
AD
A091310

END
DATE
FILMED
12-80
DTIC

become very noticeable. At $N_A = 10^{18}$ cm^{-3}, the highest value of r_S is 1.29 for T = 100 K, where the dopant impurities are only about 30 percent ionized [17]. At higher temperatures where the percentage of ionized impurity atoms is over 80 percent, the effects of hole-hole scattering bring r_S from its traditionally expected value of 1.93 to 1.05 for T = 400 K.

5.5 Hall Mobility and Hall Factor in the Combined Valence Band

Expressions for Hall coefficient, applicable in the case where holes in more than one band take place in conduction, are given by Putley [66]. For the case of p-type silicon, assuming no compensation and operation in the low field region, the Hall coefficient is given by [66]

$$R_H = \frac{\sum_{i=1}^{3} R_{Hi}\sigma_{Ci}^{2}}{\left(\sum_{i=1}^{3} \sigma_{Ci}\right)^{2}} \tag{5.10}$$

By substituting equations (2.9) and (5.6) through (5.10) into equation (5.4), the Hall mobility in the combined valence band of silicon can be expressed by

$$\mu_H = e\left\{\frac{\sum_{i=1}^{3} \frac{m_{Di}^{*\,3/2}\langle\tau_i^{2}\rangle}{m_{Hi}^{*\,2}}}{\sum_{i=1}^{3} \frac{m_{Di}^{*\,3/2}\langle\tau_i\rangle}{m_{Ci}^{*}}}\right\} \tag{5.11}$$

The conductivity mobility for the combined valence band can be expressed by

$$\mu_C = \frac{e}{m_D^{*3/2}} \left\{ \sum_{i=1}^{3} \frac{m_{Di}^{*3/2}}{m_{Ci}^{*}} \langle \tau_i \rangle \right\} \tag{5.12}$$

Then using equations (5.11) and (5.12) we can express the Hall factor in terms of the scattering relocation times and effective masses of the individual bands by

$$r_H = \frac{m_D^{*3/2} \left\{ \sum_{i=1}^{3} \frac{m_{Di}^{*3/2}}{m_{Hi}^{*2}} \langle \tau_i^{2} \rangle \right\}}{\left\{ \sum_{i=1}^{3} \frac{m_{Di}^{*3/2}}{m_{Ci}^{*}} \langle \tau_2 \rangle \right\}^2} \tag{5.13}$$

Figures 5.5 and 5.6 summarize the results of equation (5.13) as a function of temperature and dopant density. These figures show that the Hall factor ranges theoretically between 1.73 and 0.77 for temperatures between 100 and 400 K and dopant densities between 10^{14} and 10^{18} cm^{-3}. For temperatures above 200 K, r_H becomes less than unity for dopant densities greater than $5.5\text{x}10^{15}$ cm^{-3}. Figures 5.7 and 5.8 show the theoretically predicted Hall mobility as functions of temperature and dopant density. These two figures show the results of evaluating equation (5.11) with the aid of numerical integration, and adjusting the lattice scattering mobility to give the best fit to values of conductivity mobility deduced from resistivity measurements.

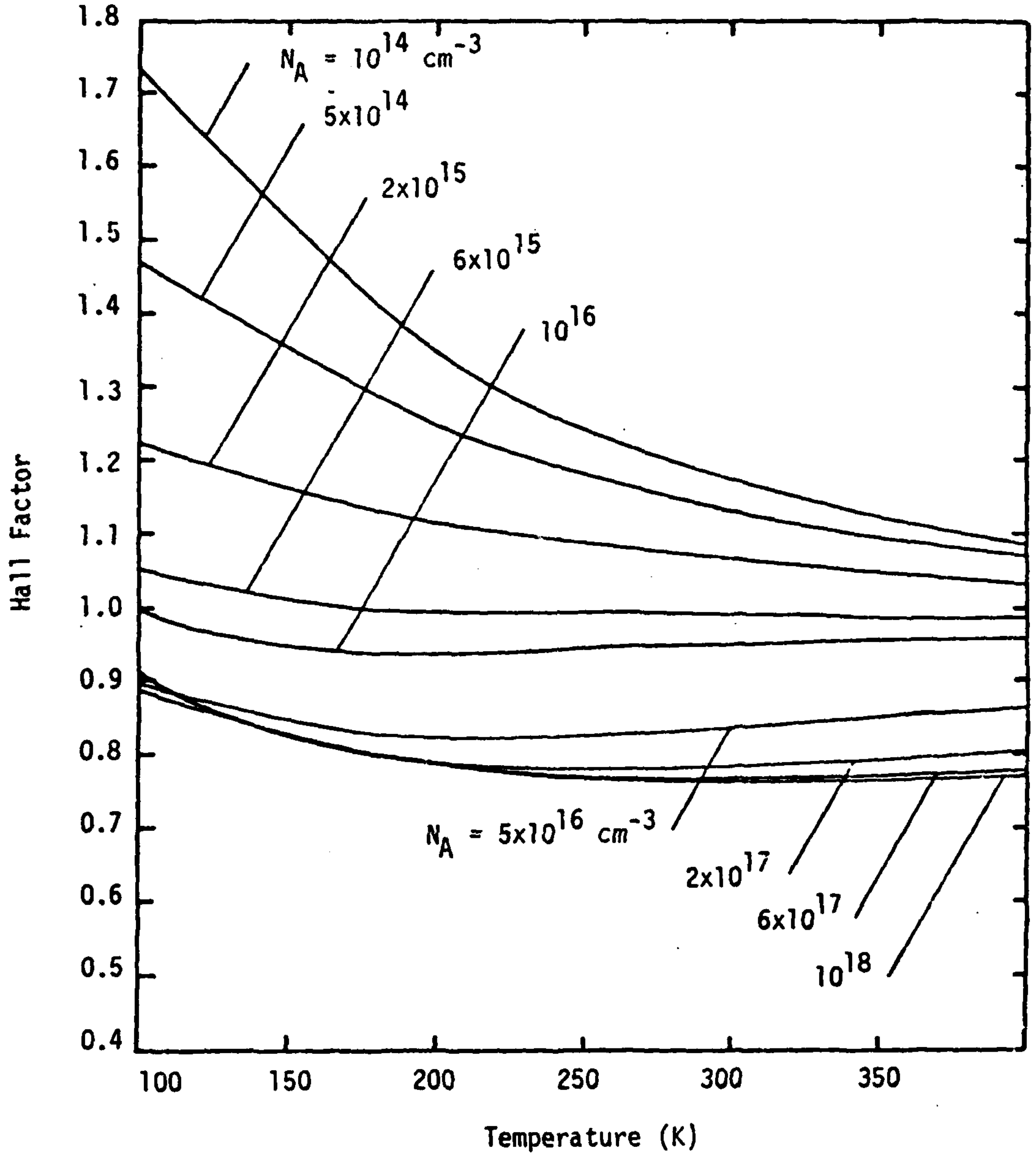

Figure 5.5. Theoretical Hall factor vs temperature for boron-doped silicon with dopant density as a parameter.

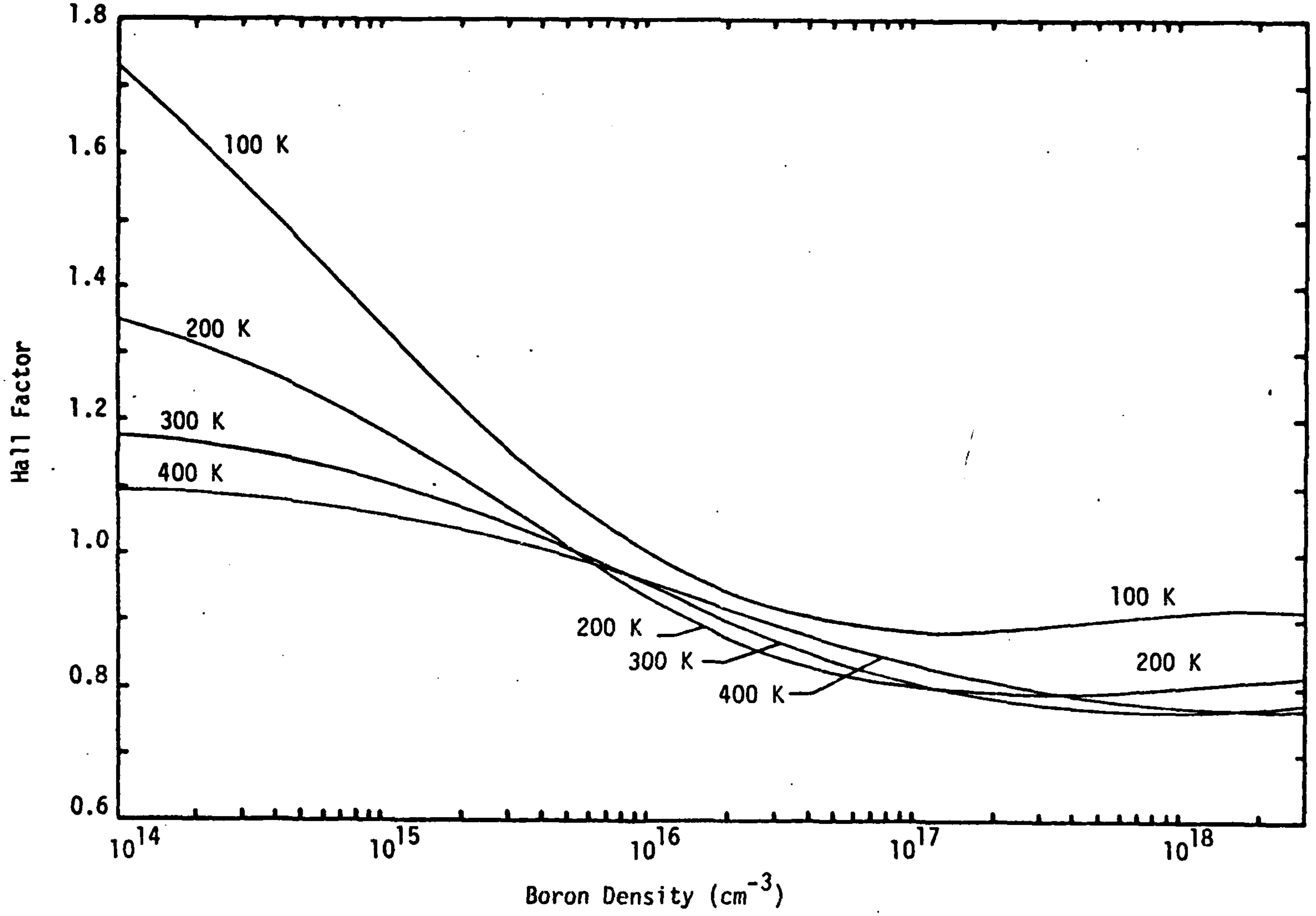

Figure 5.6. Theoretical Hall factor vs dopant density for boron-doped silicon with temperature as a parameter.

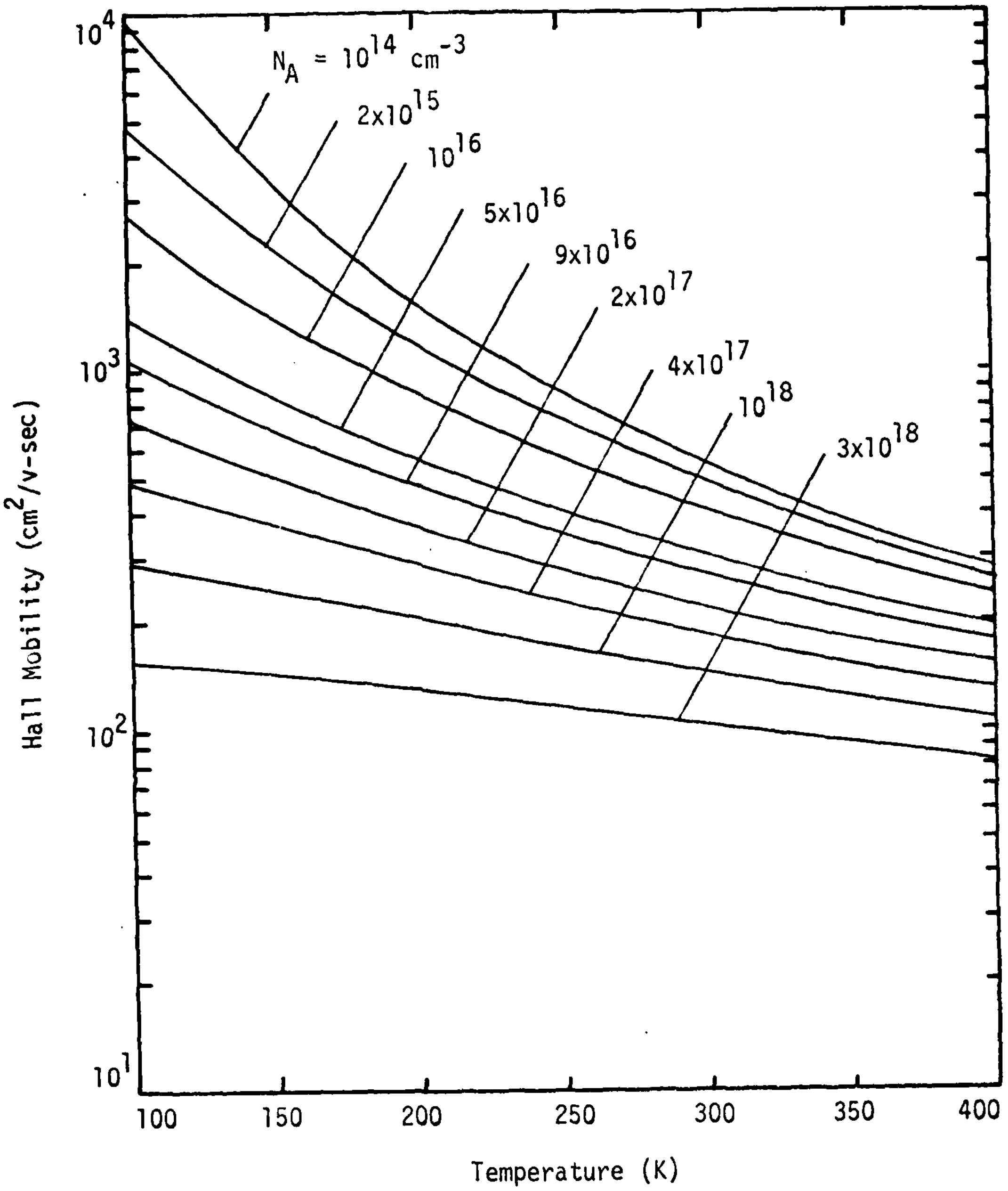

Figure 5.7. Theoretical Hall mobility as a function of temperature for boron-doped silicon with dopant density as a parameter.

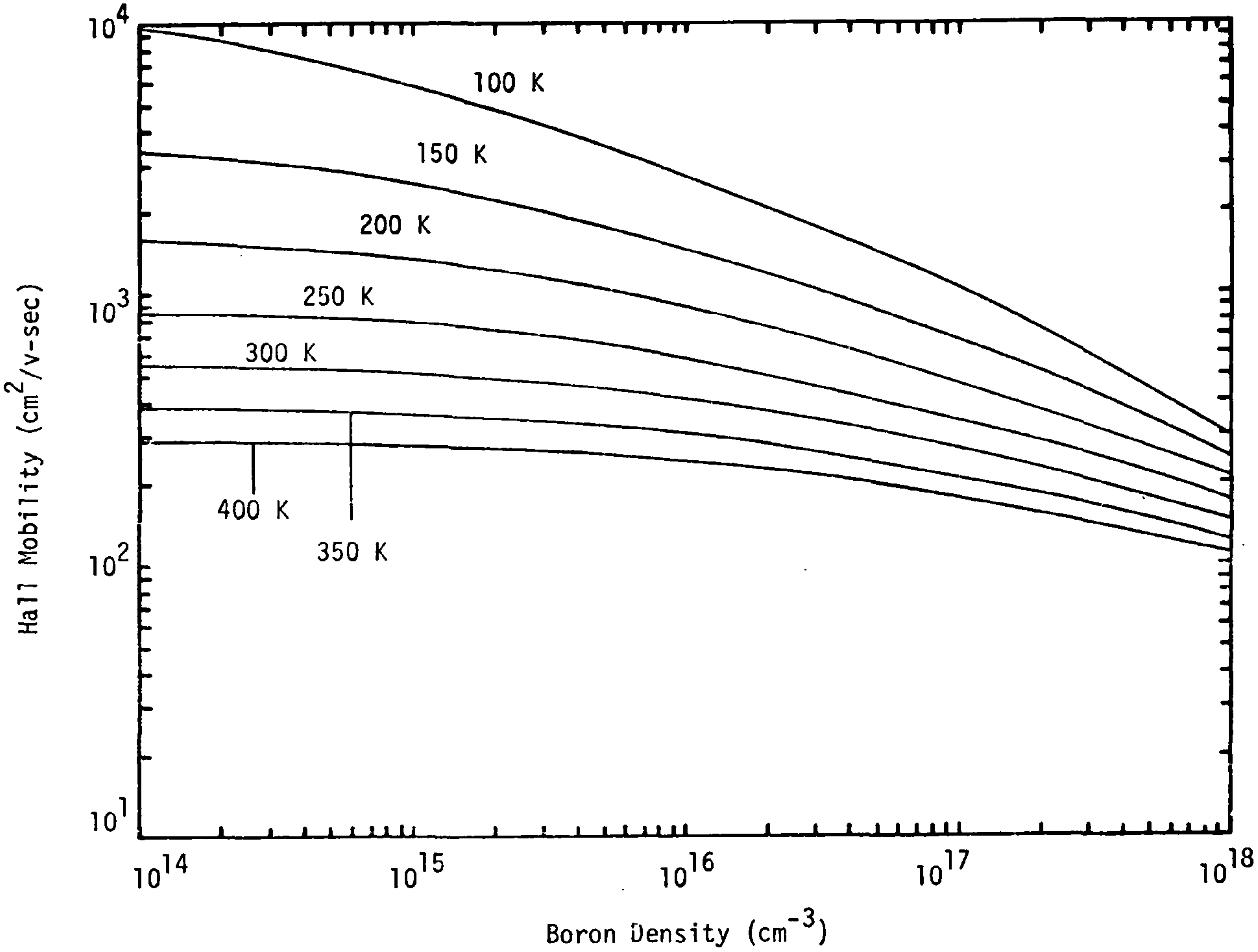

Figure 5.8. Theoretical Hall mobility as a function of dopant density for boron-doped silicon with temperature as a parameter.

CHAPTER VI

EXPERIMENTAL PROCEDURES

6.1 Introduction

Experimental measurements of resistivity, Hall coefficient and dopant density were made on six silicon wafers, four doped with gallium, and two doped with indium, in dopant densities ranging from 4.25×10^{15} to 3.46×10^{17} cm^{-3}. These wafers were cut from crystals grown along the <111> and <100> direction. Additional data were obtained from boron-doped silicon wafers to further verify the adequacy of the theory. The data were obtained from test patterns NBS-4 [67] fabricated on the silicon wafers. This test pattern was designed at the National Bureau of Standards primarily for use in the evaluation of the resistivity versus dopant density relation in silicon. Resistivity measurements were made on four-probe square array resistors and collector Hall effect resistors, while the net dopant density in the specimens was determined by the junction C-V method on a gated base-collector diode. Mean values of resistivity, dopant density and Hall coefficient were determined by measuring five to eight selected test cells with a standard deviation in resistivity at 300 K under five percent. The following sections describe the test sample preparation and fabrication procedure, and the measurement procedures.

6.2 Fabrication Procedure

The overall pattern is fabricated on a square silicon chip 200 mils on a side where six mask levels are used [68]. The masks were used in the following sequence: base, emitter, base contact, gate oxide, contact and metal. Appropriate cleaning procedures (see Appendix A) precede the diffusion of impurities, and a negative photoresist process was used in the masking steps. The base mask delineates regions whose conductivity type is opposite from that of the collector substrate, and the emitter mask delineates regions whose conductivity type is the same as that of the collector substrate. A base region approximately two μm deep is diffused into the background material; then the emitter region is diffused into the base to a depth of approximately one μm. The base contact mask is used to open windows onto the base region, where an n^+ diffusion is made to improve ohmic contact to the base. The gate oxide mask delineates regions where an oxide layer of closely controlled thickness is grown to serve as a gate for MOS devices. After front-side metallization, a portion of the wafer was separated. This section was scribed to provide the Hall effect devices. The remainder of the wafer was then metallized on the backside and alloyed. After scribing, the devices were mounted on TO-5 headers, metal contact bonding was made, and the devices were encapsulated. A layer of ceramic insulating material was used to isolate the devices from contact with the header. Resistivity measurements were then made to select devices for use in this study.

6.3 Experimental Measurements

The structures used to evaluate the resistivity of the bulk material are the Hall effect resistor and the collector four-probe resistor [68]. The four-probe resistor has four point contacts arranged in a square array. The structure (see Appendix A) is fabricated by diffusing a base over a large area except at the four point contacts which are protected from the base diffusion by oxide islands. Emitters are diffused at these points in order to make low resistance contacts to the collector material. The purpose of the base diffusion is to eliminate surface currents. The bulk resistivity is determined by forcing a current, I, between two adjacent probes and measuring the voltage, V, between the other two probes. The resistivity of the material is determined from [69]

$$\rho = \frac{2\pi SV}{(2-\sqrt{2})IC'} \qquad (6.1)$$

where S is the probe spacing and C' is a correction factor dependent on the ratio of probe spacing to the thickness of the chip [70]. This correction factor is given by

$$C' = 1 + \frac{4}{2-\sqrt{2}} \sum_{n=1}^{\infty} (-1)^n \left(1 + \frac{4n^2w^2}{S^2}\right)^{-1/2} - \frac{2\sqrt{2}}{2-\sqrt{2}} \sum_{n=1}^{\infty} (-1)^n \left(1 + \frac{2n^2w^2}{S^2}\right)^{-1/2} \qquad (6.2)$$

where w is the thickness of the chip.

The collector Hall effect resistor is a four-terminal resistor formed in a square chip 100 mils on a side. Contacts are formed on the four corners by an emitter diffusion (see Appendix A). The resistivity is calculated from [71]

$$\rho = \frac{\pi w}{\ell n2} \frac{V}{I} \tag{6.3}$$

where w is the thickness of the chip, and V is the voltage difference between nearest neighbor contacts for a current, I, passed between the remaining two contacts. The TO-5 header was mounted in the sample holder of an Air Products and Chemicals AC-3L CRYO-TIP liquid nitrogen system. This enabled variation of the sample temperature between 100 and 350 K. The temperature was measured by a chromel vs gold with 0.07 atomic percent iron thermocouple. For temperatures above 350 K, the sample was placed in a Stratham Temperature Test Chamber.

The structure used for the Hall coefficient measurements is the collector Hall effect resistor. The Hall coefficient is calculated from

$$R_H = \frac{V_H w}{BI} \tag{6.4}$$

where V_H is the voltage difference measured between opposite contacts for a current, I, passed between the remaining two contacts, and B is the magnetic field density perpendicular to the plane of the chip; thus the samples are oriented so that the magnetic field is in the crystal growth direction, <111> for the gallium-doped samples, and <100> for the indium-doped samples. The Hall mobility is determined from

$$\mu_H = \frac{R_H}{\rho} \qquad (6.5)$$

where ρ is determined from resistivity measurements on the Hall and four-point structures. The magnetic field for the Hall measurements was provided by a Varian Associates (V3703) six-inch electromagnet with a current regulated power supply (V-FR2503). The magnetic field strength was monitored by a Bell 620 gaussmeter with an STB4-0402 probe with a stated accuracy of 0.1 percent. Data was taken over a temperature range from 100 to 350 K. The current used in the resistivity and Hall coefficient measurements was provided by a Keithley 225 current source capable of accuracy within ±0.5 percent of the three-digit readout. The current was monitored by voltage readings across precision resistors connected in series with the current source. These resistors were part of a Dana-651 current shunt set, accurate to within 0.01 percent. Voltages were measured with a Hewlett Packard 3465A digital multimeter with a stated accuracy within 0.03 percent of the readout. Resistivity and Hall coefficient measurements were made in accordance with ASTM standard procedures [72].

The impurity dopant density was obtained by use of two different structures: an MOS capacitor, and a base-collector diode. The MOS capacitor over collector consists of a main gate which is surrounded by a field plate that overlaps a channel stop which also serves as top side collector contact [68]. This structure (see Appendix A) is used to measure the collector dopant density ($N_A + N_D$) from the high frequency C-V deep depletion method [73]. The collector dopant density is determined by obtaining a dopant profile from C-V measurements by means of

$$N(x) = \frac{2}{e\varepsilon_S A'^2} \frac{\Delta V}{\Delta C^{-2}} \tag{6.6}$$

where ΔV is an incremental change in the gate voltage, and the measured capacitance is due to both the oxide and the semiconductor. A self-consistent check was made on the measurements of collector dopant density by using the base-collector diode. This structure (see Appendix A) consists of a base diffused into a collector and a metal field plate to control the periphery. The field plate overlaps both the base and a diffused emitter channel stop which also serves as topside collector [68]. To obtain a correct density profile the field plate is biased at the flat-band potential [74]. Capacitance-voltage measurements were taken with a Princeton Applied Research 410 C-V Plotter and a Hewlett Packard 7010A X-Y Recorder.

From each silicon wafer, eight four-probe resistors, eight Hall resistors, and eight capacitor-diode chips were selected for encapsulation. These were chosen on the basis of low leakage currents and good contacts at the metal bonding pads. Measurements were made on each of the devices and data from the five to eight devices closest to the mean value of the measurements were then averaged. In this manner we arrived at representative values of resistivity, Hall coefficient, and dopant density for each sample. The results of these measurements and comparisons with the theory of Chapters III through V are presented in the next chapter.

CHAPTER VII

COMPARISON OF THEORETICAL AND EXPERIMENTAL RESULTS

7.1 Conductivity Mobility

Conductivity mobility was evaluated by substituting the measured resistivities into equation (4.7). Figure 7.1 shows the hole mobility plotted as a function of hole density at 300 K for boron-doped silicon. Curve 1 represents the theoretical results of equation (3.23), and curve 2 was reproduced from the work of Wagner [8]. Our calculated values are within six percent of the values reported by Wagner for $N_A \leq 3\text{x}10^{17}$ cm^{-3}. For higher values of hole density our calculated values are substantially higher than those of Wagner. As previously explained by Li [17], this discrepancy is due to Wagner's assumption of complete ionization of boron impurities. This assumption is valid only at low dopant densities or at high temperatures where full ionization of boron atoms prevails. The theoretical calculation is in excellent agreement (within three percent) with experimental data reported by Thurber et al [12]. This gives support to the validity of ionization calculations based on equations (4.2) through (4.6). Mobility values reported by Horn [13] are also in reasonable agreement with our theoretical results. The data points shown in Figure 7.1 were corrected for deionization effects via equations (4.2) through (4.6).

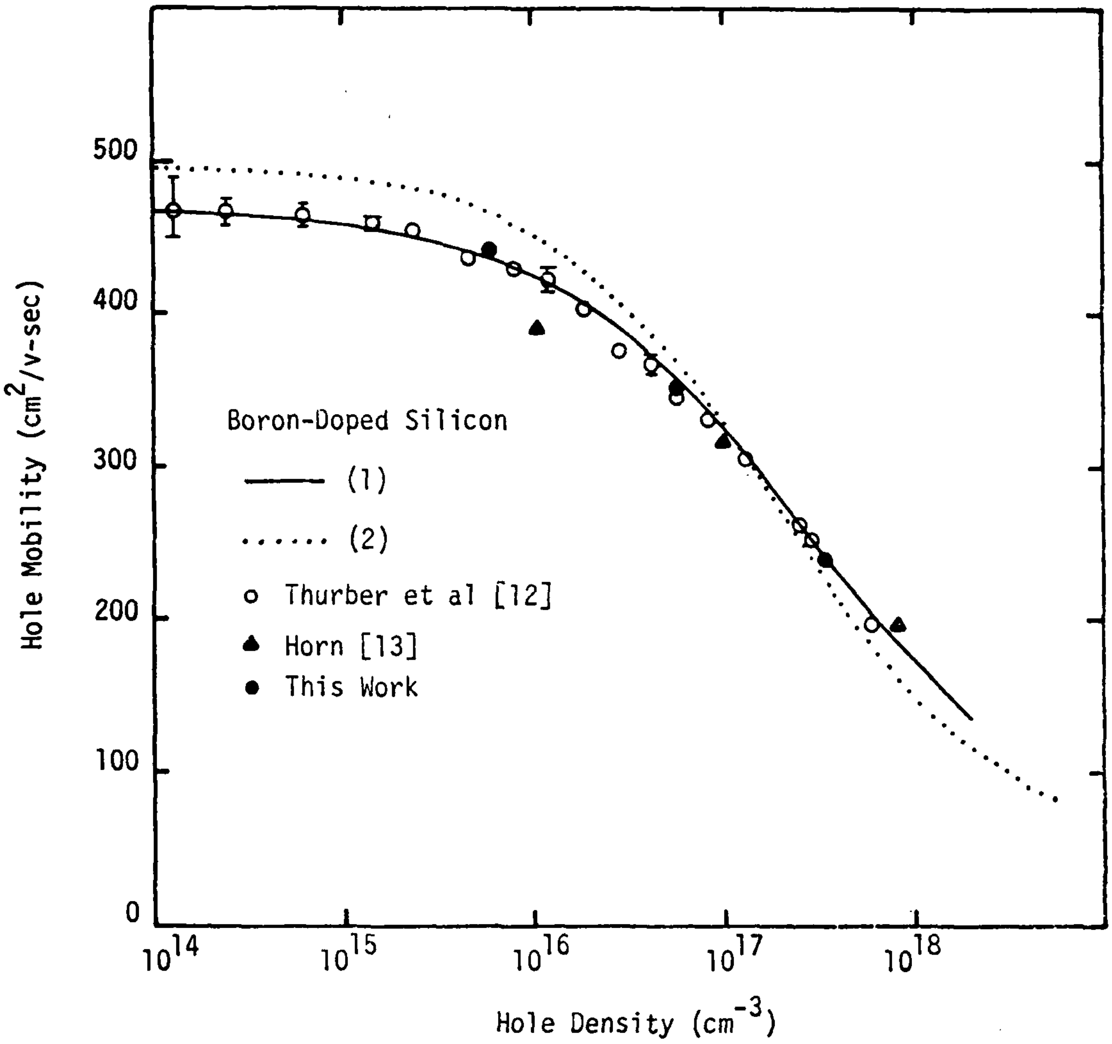

Figure 7.1. Hole mobility vs hole density for boron-doped silicon at 300 K. Curve 1 is the theoretical calculation from equation (3.23), and curve 2 is reproduced from Wagner [8]. Shown also are the experimental results of this work, Horn [13], and Thurber et al [12]. All data points have been corrected for deionization effects.

7.2 Resistivity

The resistivity vs dopant density relationship for boron-doped silicon at 300 K is shown in Figure 7.2. The solid line represents theoretical calculations using equation (4.7). Wagner's [8] resistivity curve and the theoretical line coincide over most of the boron density range. Our theoretical calculations agree with Wagner's resistivity data within six percent over the entire range of boron densities considered at T = 300 K. Excellent agreement exists between our experimental data and the theoretical calculations at 300 K. Figure 7.2 also shows excellent agreement between our theoretical calculations and the data of Thurber et al [12]. Good agreement was obtained with the data of Thurber and Carpenter [75] where total boron density was obtained by the nuclear track technique.

Figure 7.3 shows the resistivity of gallium- and indium-doped silicon as a function of total dopant density for T = 300 K. As expected, because of the deeper ionization energy of indium as compared to gallium, values of resistivity for gallium doped silicon are lower than values of resistivity for indium-doped silicon at the same total dopant density. Figure 7.3 does not show this at low dopant densities because of the assumed values of background boron impurity densities. Excellent agreement was obtained between our experimental data and that obtained from Wolfstirn [15] for gallium-doped silicon, and our theoretical calculations at T = 300 K. Data obtained from the two indium-doped samples showed good agreement with the theoretical calculations, but the same was not true for the data of Schroder et al [64], and Backenstoss [16]. As seen in Figure 7.3, for each value of measured resistivity, Schroder et al [64] report two different values of measured indium density. The

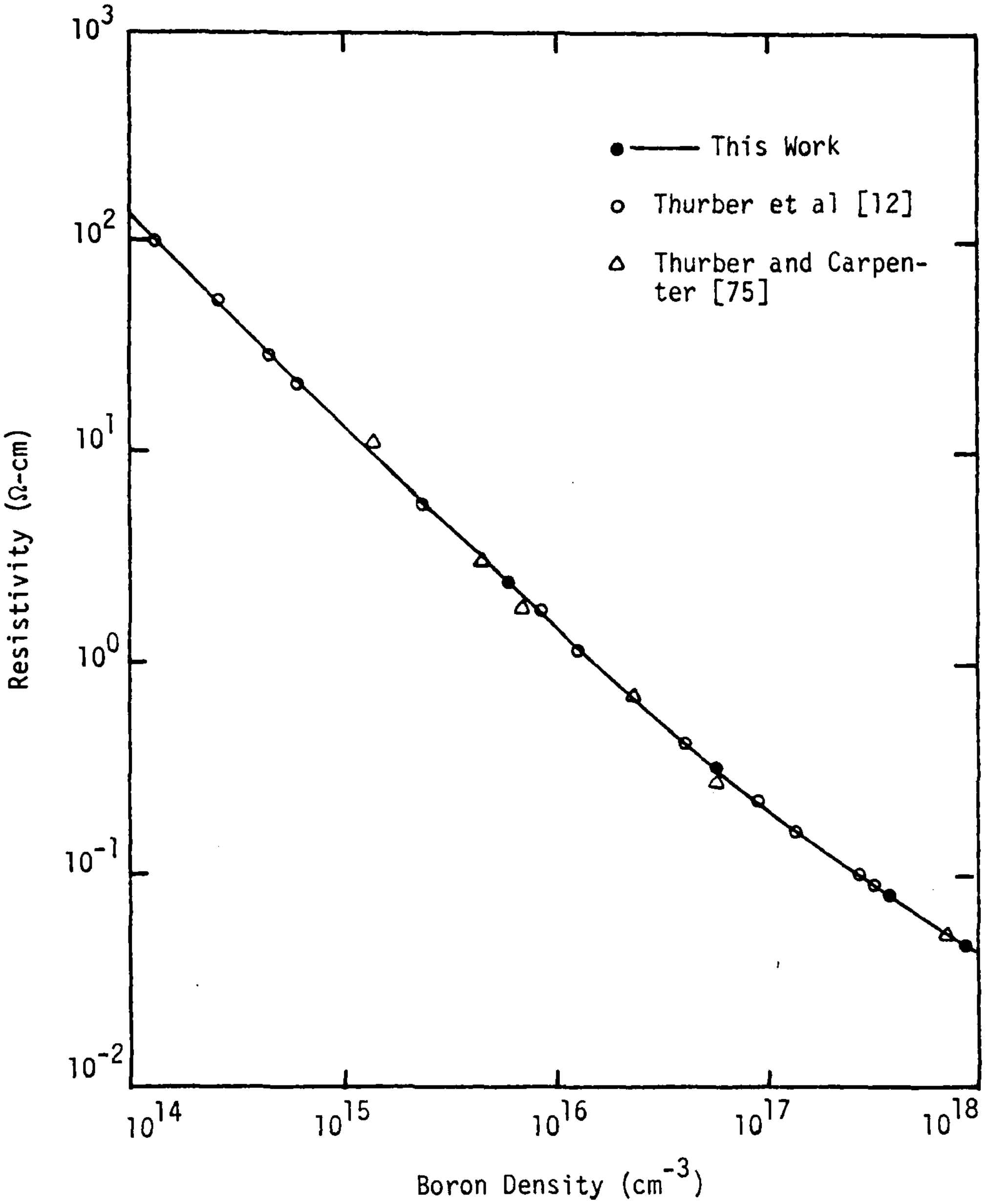

Figure 7.2. Resistivity vs dopant density for boron-doped silicon at 300 K. Shown are the theoretical calculations from equation (4.7) and the experimental results of this work, Thurber and Carpenter [75], and Thurber et al [12].

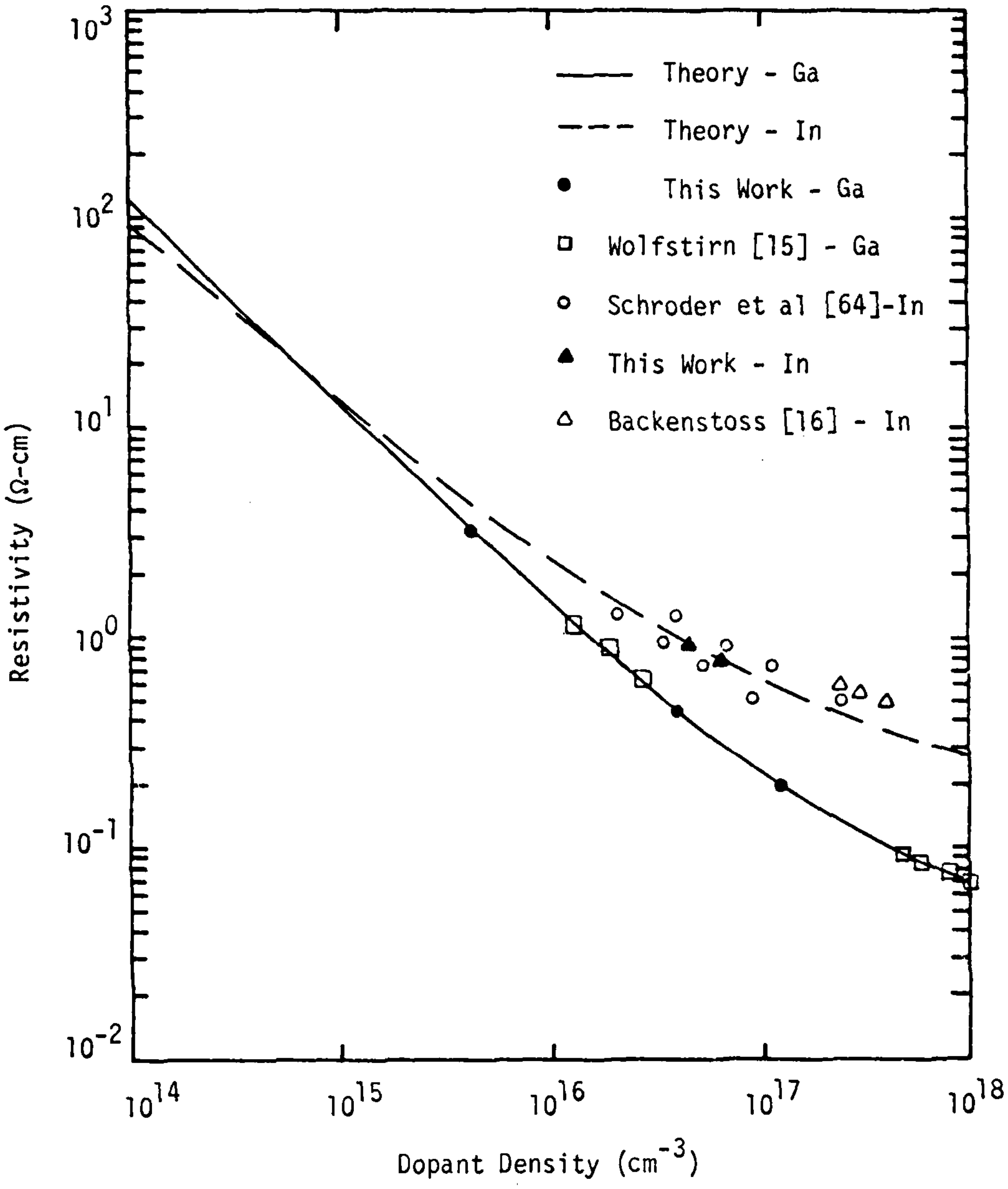

Figure 7.3. Resistivity vs dopant density for gallium- and indium-doped silicon at 300 K. Shown are theoretical calculations from equation (4.7) and the experimental results of this work, Wolfstirn [15], Schroder et al [64], and Backenstoss [16].

lower value of indium density was obtained by C-V and junction breakdown methods, while the higher value was obtained by Hall measurements and curve fitting. Because of uncertainties in the value of the Hall scattering factor, Schroder et al consider the lower value of density more reliable. Note that our theoretical calculation falls between the two values of dopant density reported by Schroder et al [64]. Values of resistivity of indium-doped silicon reported by Backenstoss [16] are about 25 percent higher than our calculated values. The work of Backenstoss [16], however, was done in the high doping region where dopant densities approach the limit of solid solubility. Backenstoss found that for dopant densities greater than 4×10^{17} cm^{-3} there was a considerable amount of indium precipitation. Thus it is possible that part of the discrepancy between our theoretical calculations and the data of Backenstoss is due to the low solid solubility limit of indium in silicon. Recent theoretical results of Sclar [14] for In-doped silicon also agree very closely with our theoretical calculations at 300 K.

To find out the adequacy of our theoretical model for temperatures other than 300 K, we compared the calculated and measured values of resistivity for silicon samples doped with boron, gallium and indium for temperatures ranging from 100 to 400 K. Figure 7.4 shows the comparison between the theoretical and measured resistivities for boron-doped silicon. Except for a couple of data points, agreement between the theoretical and measured values was within 8 percent over the entire range of temperatures. Figures 7.5 and 7.6 show the comparison between theoretical and measured resistivities for gallium- and indium-doped silicon respectively. Agreement here was not as good as in the boron-doped case, but except for a couple of data points, agreement between

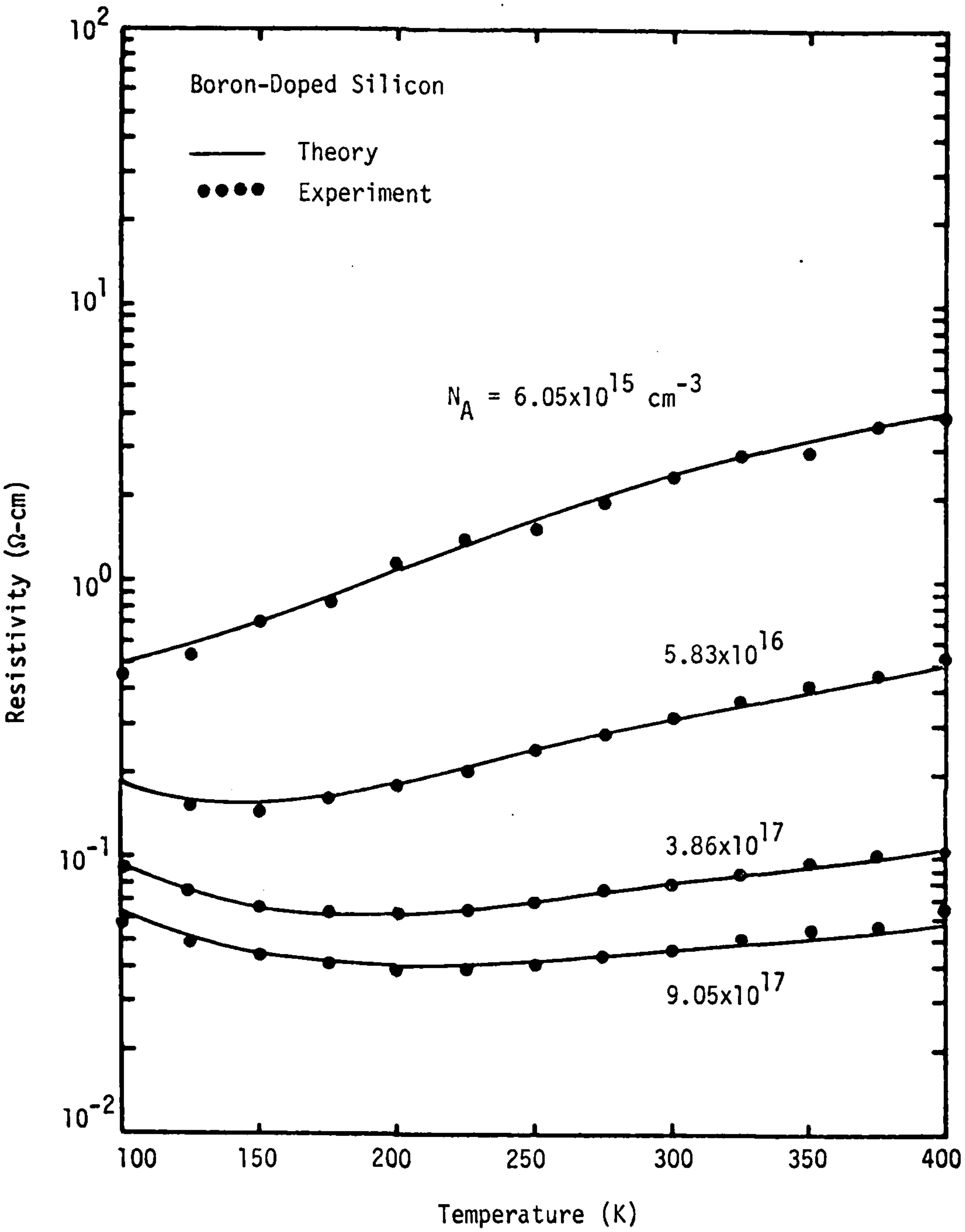

Figure 7.4. Resistivity vs temperature for the boron-doped silicon samples. Solid lines are the theoretical calculations and solid dots are the experimental data.

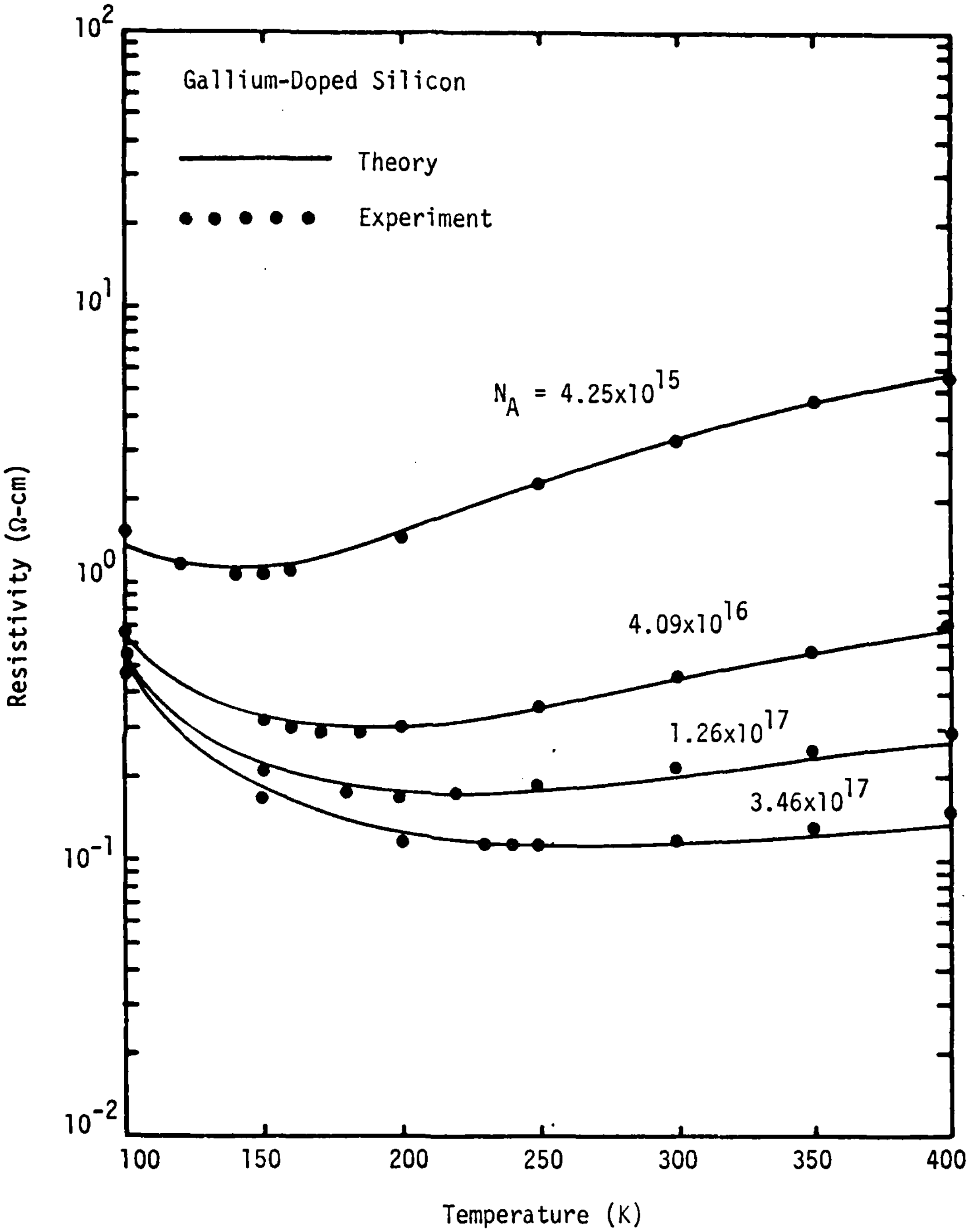

Figure 7.5. Resistivity vs temperature for the gallium-doped silicon samples. Solid lines are the theoretical calculations and solid sots are the experimental data.

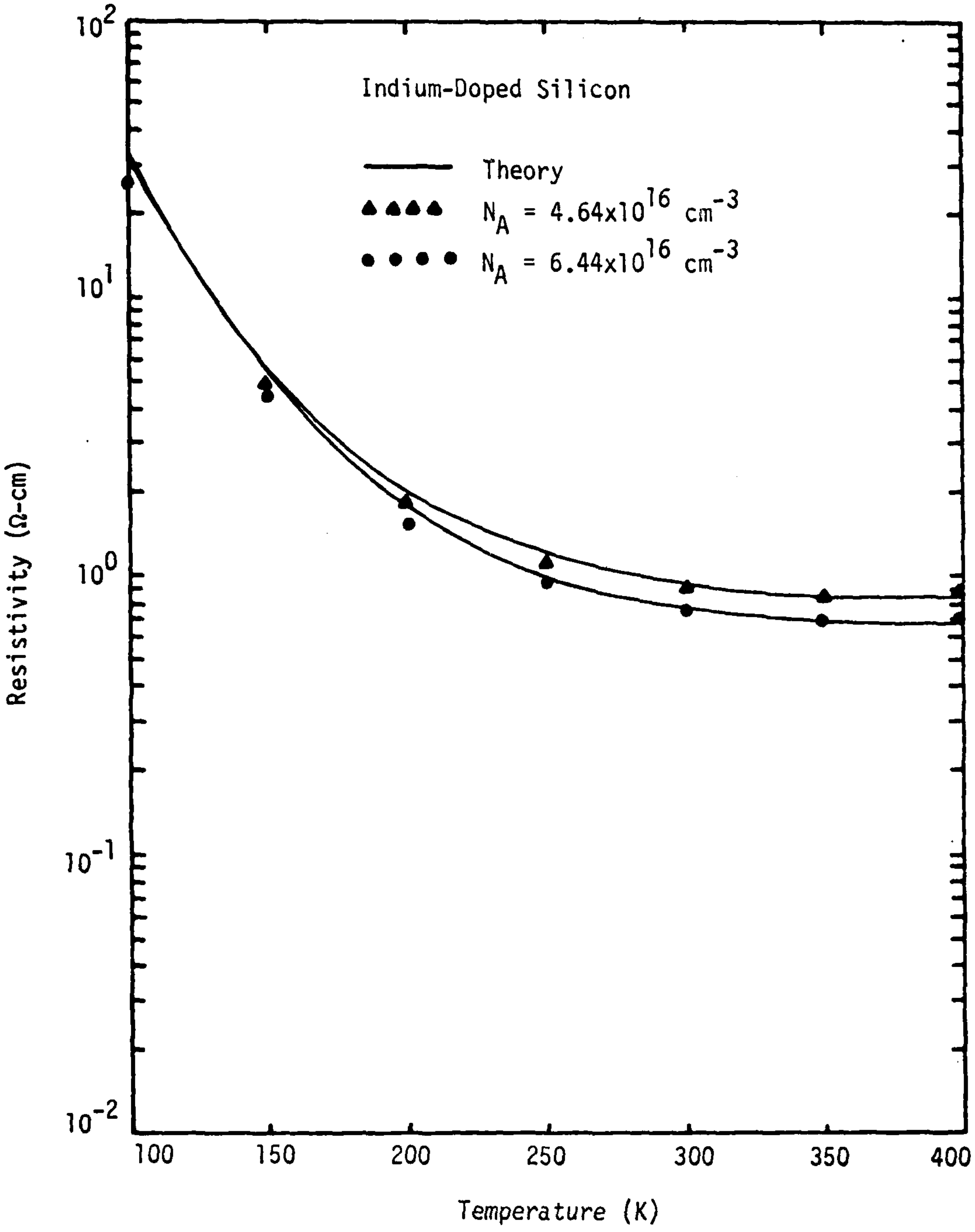

Figure 7.6. Resistivity vs temperature for the indium-doped silicon samples.

theory and experiment was within 10 percent. For the indium-doped samples, the largest discrepancies occurred at low temperatures. This is suggestive of some degree of compensation in the samples. An experimental estimate of percentage of compensation was not made for any of the silicon samples studied in this work.

7.3 Hall Mobility

Figures 7.7 through 7.12 show the experimentally determined Hall mobility for silicon slices doped with gallium and indium. Agreement between theory and experiment is good for temperatures above 150 K for the gallium-doped samples. However, for temperatures of 150 K and below some points differ from the theoretical prediction by as much as 38 percent. The measured Hall mobility of the indium-doped samples is well within 15 percent of the calculated value except for one data point at $T = 100$ K. Our control over the temperature of the samples was better for the $T \geq 200$ K range, but the main source of the discrepancy between theoretical and experimental values of Hall mobility is the Hall factor. This will be discussed in the next section. The magnetic field was rated accurate to within 1 percent. Data points representing a Hall mobility-dopant density pair are estimated to have a total error of around 8 percent.

7.4 Hall Factor

The Hall factor in the case of p-type silicon, is plotted as a function of dopant density for $T = 300$ K in Figure 7.13. With the exception of the points deduced from Morin and Maita's [5] data for boron-doped silicon, agreement between the Hall factor-dopant density data and the theoretical calculation is within 15 percent for

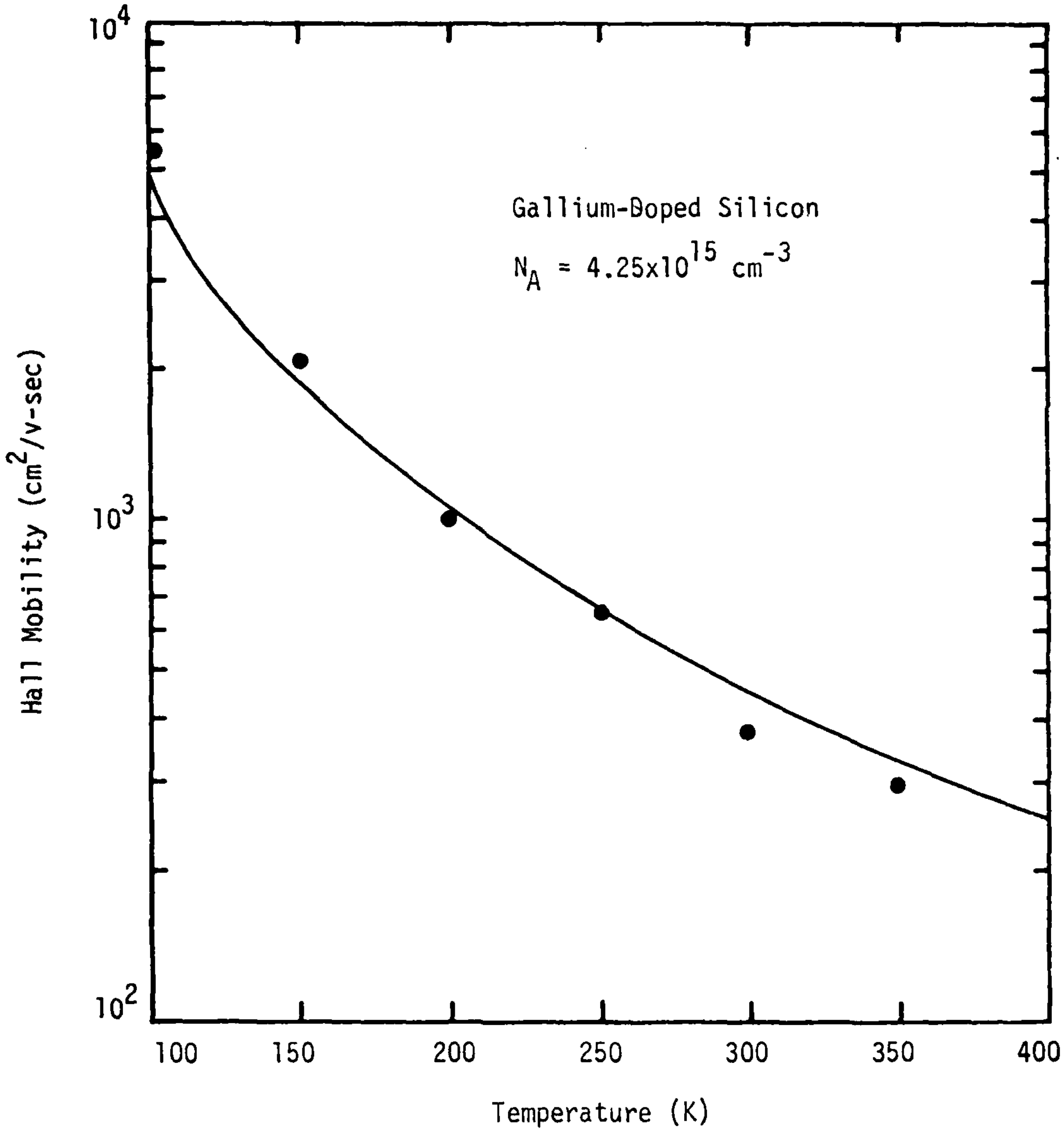

Figure 7.7. Hall mobility vs temperature for gallium-doped sample. $N_A = 4.25\times10^{15}$ cm^{-3}.

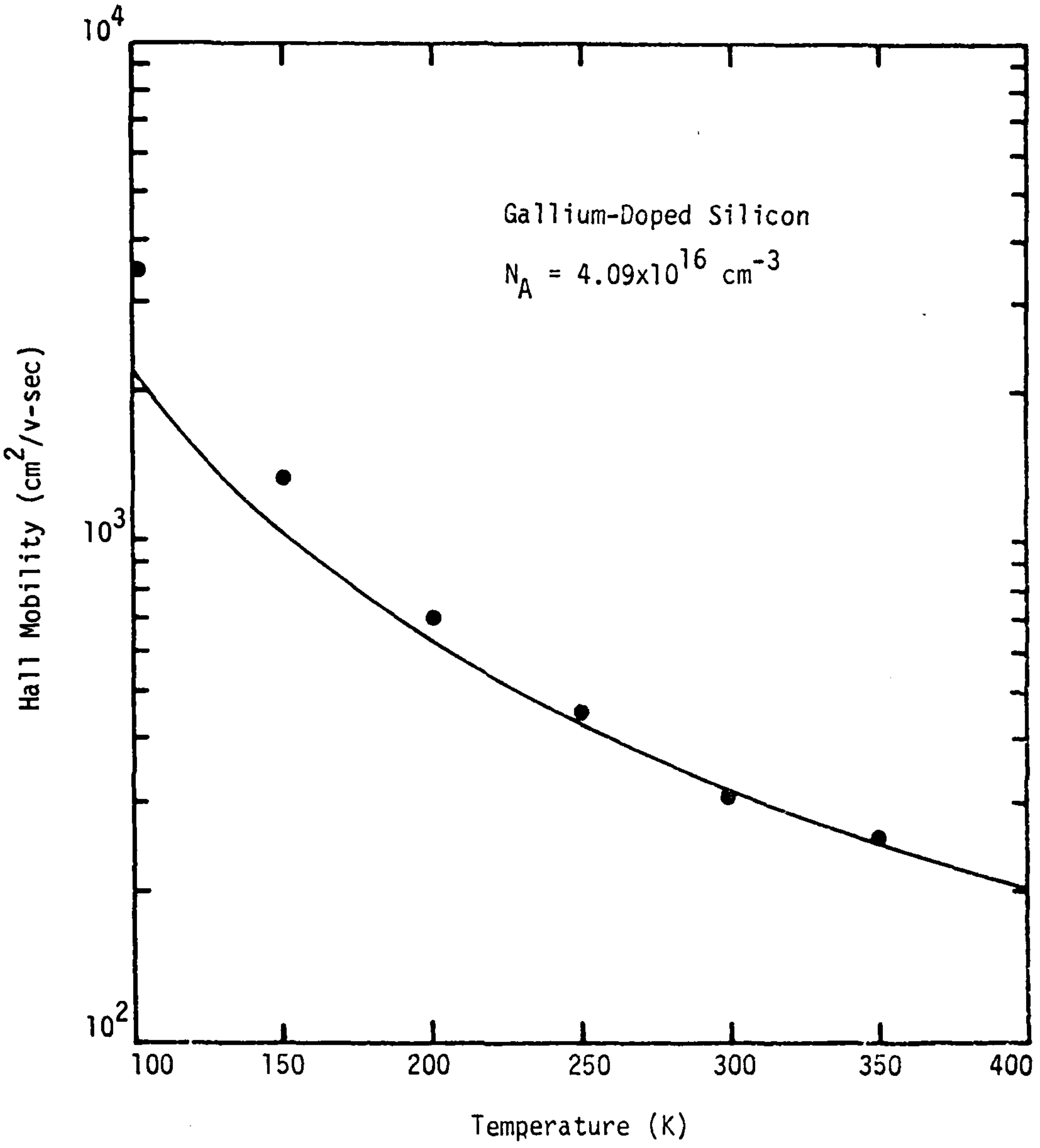

Figure 7.8. Hall mobility vs temperature for gallium-doped sample. $N_A = 4.09 \times 10^{16}$ cm^{-3}.

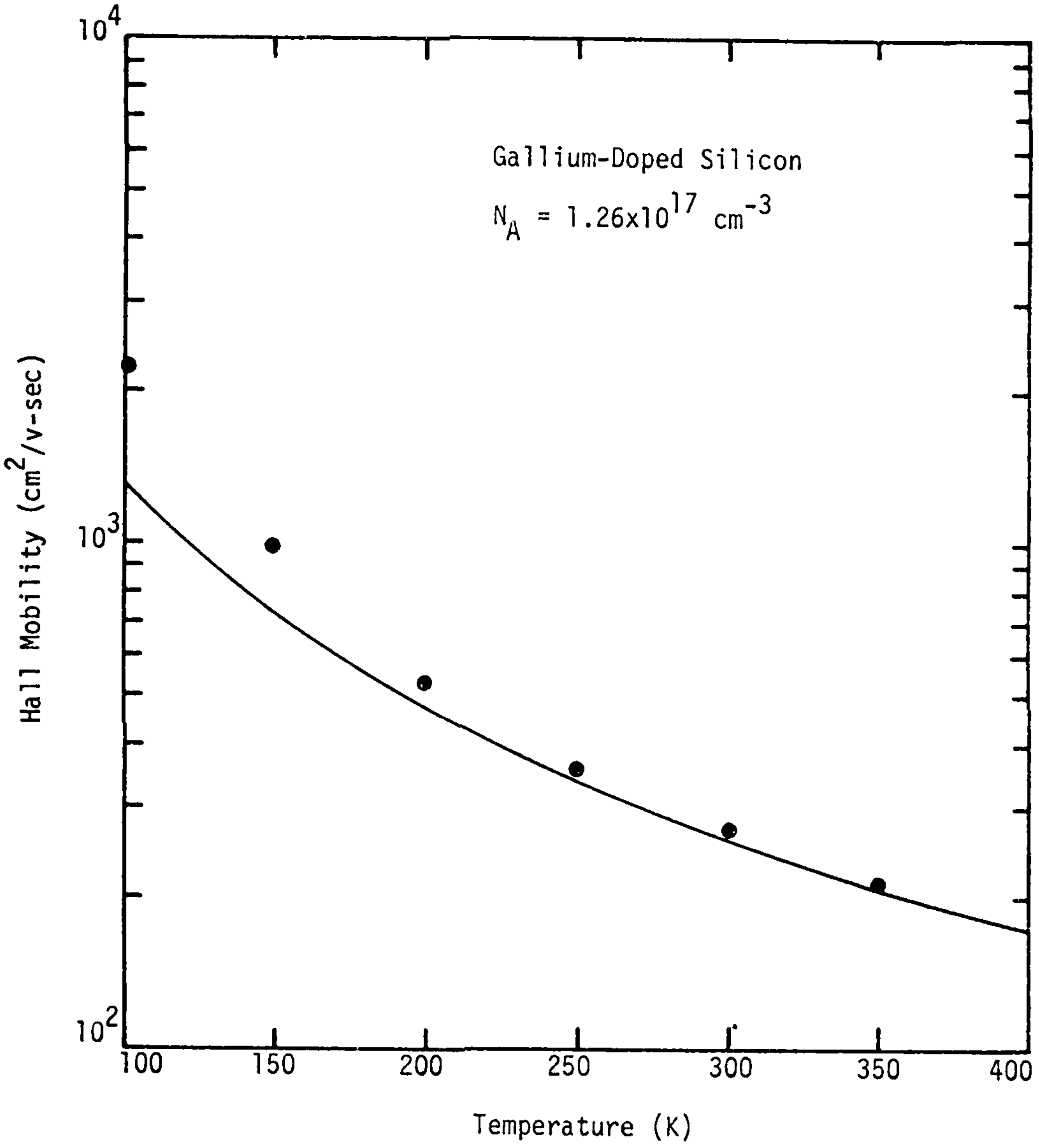

Figure 7.9. Hall mobility vs temperature for gallium-doped sample. $N_A = 1.26\times10^{17}$ cm^{-3}.

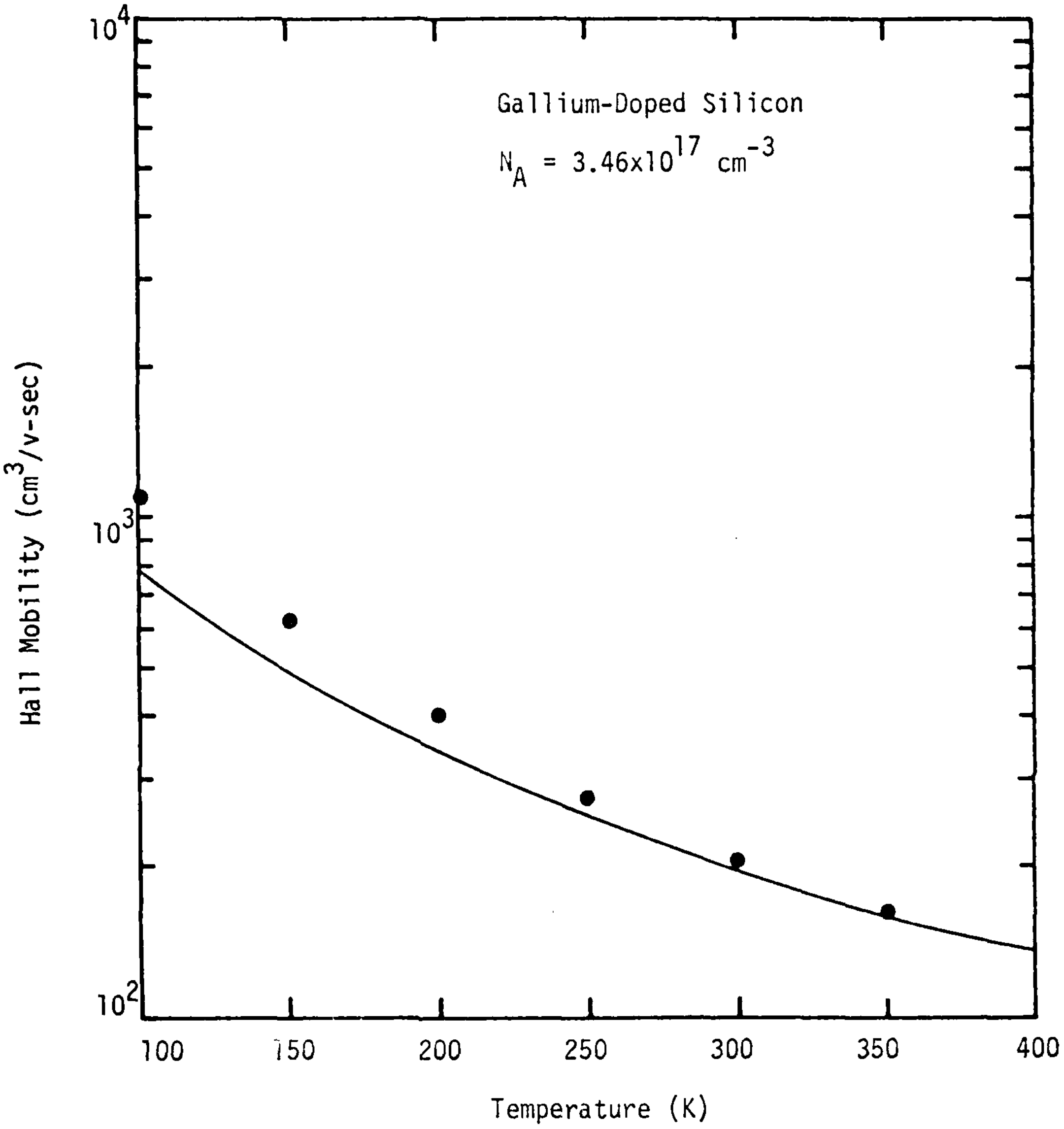

Figure 7.10. Hall mobility vs temperature for gallium-doped sample. $N_A = 3.46\text{x}10^{17}$ cm^{-3}.

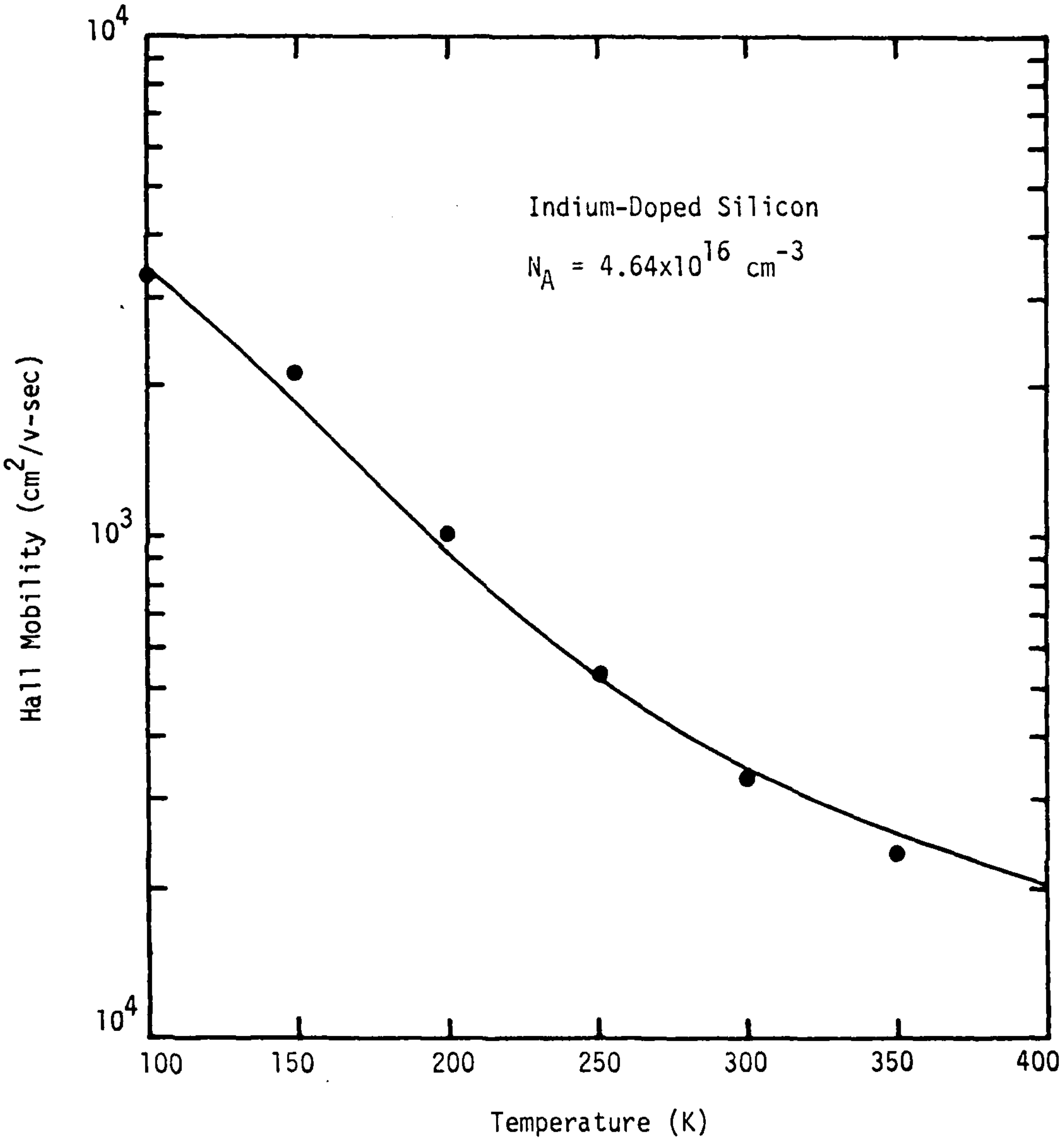

Figure 7.11. Hall mobility vs temperature for indium-doped sample. $N_A = 4.64x10^{16}$ cm^{-3}.

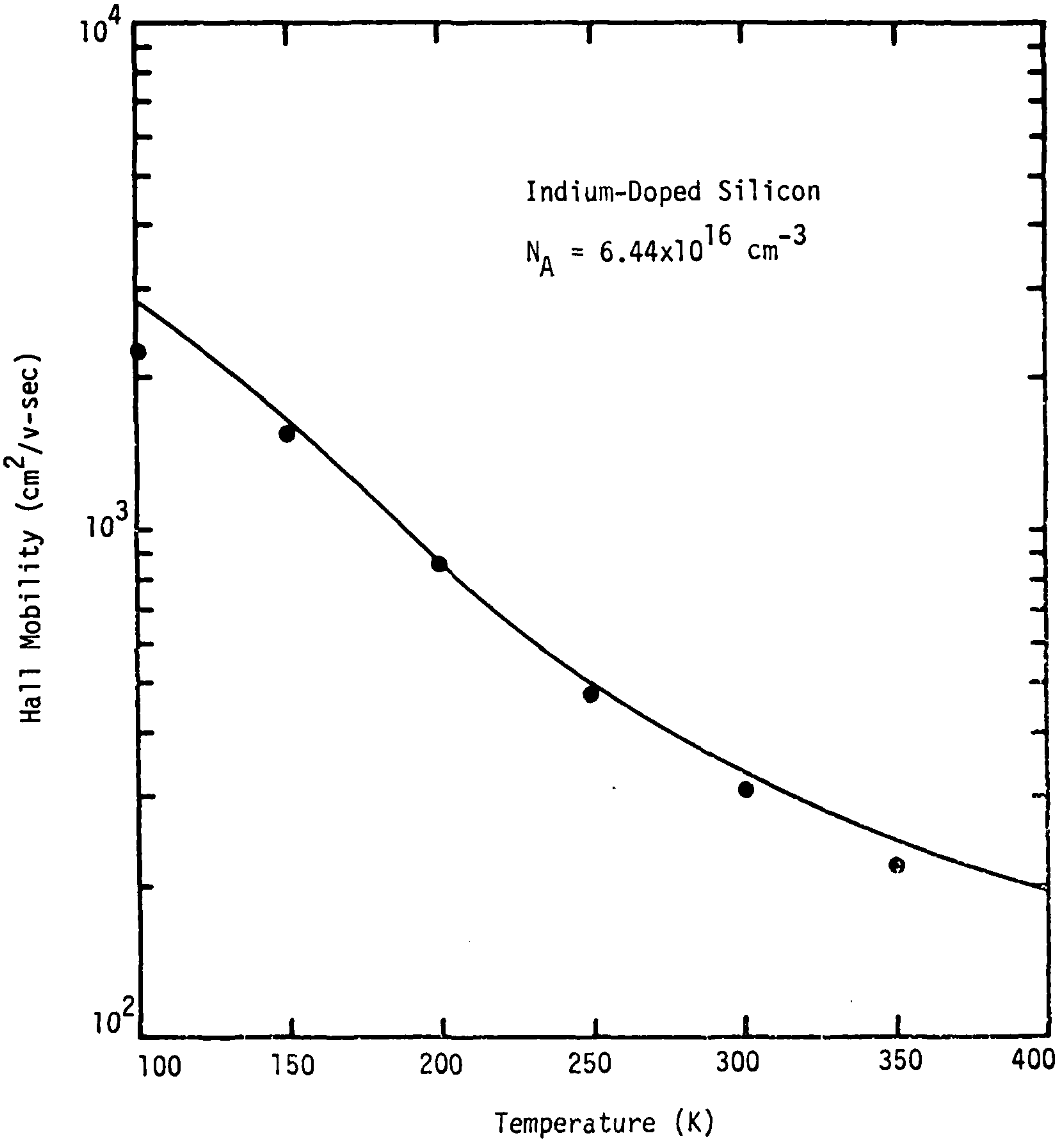

Figure 7.12. Hall mobility vs temperature for indium-doped sample. $N_A = 6.44 \times 10^{16}$ cm^{-3}.

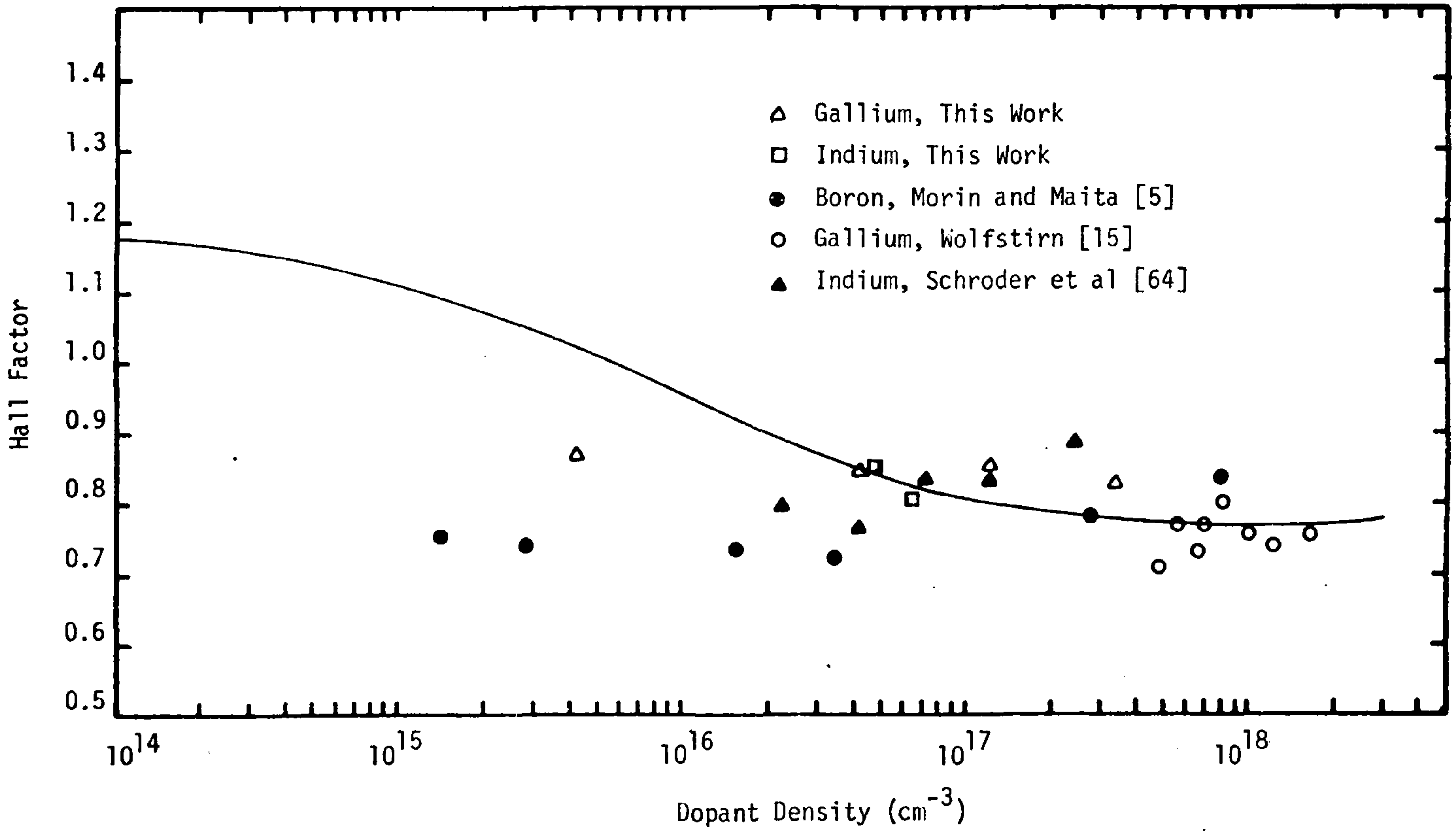

Figure 7.13. Hall factor vs dopant density for p-type silicon at 300 K. Shown are the theoretical calculations from equation (5.13) and the experimental results of this work, Wolfstirn [15], Morin and Maita [5], and Schroder et al [64].

$N_A > 5\text{x}10^{15}$ cm^{-3}. While in general, agreement between theory and experiment in this region of dopant density is only within 15 percent, the bulk of the experimental data is within 10 percent of the theoretical prediction. The samples used by Morin and Maita [5] showed a considerable degree of compensation; in their lower-doped samples, the compensation was as high as 20 percent. This fact may have contributed to the low values of measured Hall mobility, and the large discrepancy between these data points and the calculation. This model neglects the effects of compensation, and the combined presence of acceptor impurities of varying ionization energies. The overall effect of adding impurities of both signs is one of increased ionization of the excess N_A or N_D [15]. It would be necessary to know the percentages of compensation of the experimentally measured crystals to accurately determine the adequacy of the theory at low dopant densities. An experimental estimate of percentage of compensation was not made for any of the silicon samples studied in this work. Long [38] has noted that the low measurements of Hall mobility for p-type silicon may not be due entirely to compensation and the quality of the crystals. For reasonably pure silicon samples (ρ = 35 ohm-cm, $N_A = 4.4\text{x}10^{15}$ cm^{-3}) Long [38] obtained Hall mobilities between 360 and 390 cm^2/volt-sec. Hall mobilities as great as 450 cm^2/volt-sec have also been reported [76]. While higher than the Hall mobilities of Morin and Maita, these measurements [38,76] still indicate a value of Hall factor for low-doped p-type silicon at 300 K less than unity. It is still doubtful that a Hall mobility smaller than a conductivity mobility at 300 K is really an intrinsic property of p-type silicon [38]. It is possible that the Hall factor may be greater than unity in a crystal of exceptionally high perfection. However, calculations involving an exact model of the valence band of silicon [77] indicate that the anisotropy of the bands, while not important in the interpretation of mobility and resistivity data, plays an important role in the evaluation of the Hall factor. Our model averages out the anisotropy of the bands and thus our values of the mass anisotropy factor, r_A, are larger than an exact model would predict. A calculation based on the exact model, applicable over the entire range of interest of temperatures and dopant densities, is beyond the scope of this work. At the higher dopant densities there is fair agreement between the theoretical prediction and values of Hall factor deduced from our experimental work and the data of Wolfstirn [15]. Data points from Wolfstirn's work showing ionization energies greater than 0.065 eV were not included in Figure 7.13 because of the high degree of compensation of these samples.

CHAPTER VIII

SUMMARY AND CONCLUSIONS

Theoretical expressions have been derived to compute the hole mobility, resistivity and Hall factor as functions of dopant density and temperature for silicon doped with boron, gallium and indium. The valence band of silicon was represented by a three-band model which takes into account the nonparabolic nature of the bands. This attribute of the valence band is included in the effective mass calculations. Contributions from scattering by acoustical and optical phonons, ionized impurities and neutral impurities were considered in the calculation of average relaxation time. In addition, our model also takes into account the effect of hole-hole scattering on both lattice and ionized impurity scattering relaxation times, and the effect of interband transitions on the acoustic phonon relaxation time. Thus the model developed in this study represents a more complete theoretical description of the conductivity mobility, Hall mobility, Hall factor and resistivity than previous theoretical models have acknowledged.

As stated in Chapter II, the model used for the valence band of silicon provides values of density-of-states effective mass which lead to values of intrinsic carrier density which are well within the limits of experimental error. The greatest deficiency this model has over an exact calculation is that the anisotropy of the bands has been averaged out. Thus while the temperature dependence of effective mass derived from the exact and approximate models of the valence band is similar, the magnitudes of the masses may be substantially different. This difference is not relevant in the study of mobility and resistivity in p-type silicon, but becomes important in the determination of the Hall factor. Since direct experimental verification of values of conductivity and Hall effective masses is not possible, the only way to assess the value of effective mass calculations is by using the theory in the development of directly measurable properties such as resistivity and Hall mobility.

The resistivity analysis for the boron-, gallium-, and indium-doped silicon samples showed agreement between experimental and theoretical results within 10 percent over the entire range of temperature, $100 \leq T \leq 400$ K. Note that best agreement between theory and experiment was obtained for boron-doped samples, followed by gallium- and indium-doped samples. This may be due to the fact that we neglect the compensation effect and the possible dependence of ionization energy on dopant density in the theoretical calculations for gallium- and indium-doped samples. An experimental estimate of degree of compensation was not made for any of the silicon samples studied here. Data points representing a resistivity-dopant density pair are estimated to have a total error of around 6 percent.

A comparison between our calculated mobility values with those of Wagner's [8] data on boron-doped silicon at 300 K shows that agreement is within ±6 percent for $N_A \leq 3\times10^{17}$ cm^{-3}. Discrepancies at higher dopant densities can be eliminated if the effect of deionization of boron impurities were included in Wagner's calculations [8]. Excellent agreement was found between our theoretical calculations of mobility in boron-doped silicon and the data of Thurber et al [12] at 300 K. We have obtained excellent agreement between theoretical values of resistivity and our experimental data for boron-, gallium-, and indium-doped silicon at 300 K; our theoretical calculations also agreed with the resistivity data by Thurber et al [12] for boron-doped silicon, and Wolfstirn [15] for gallium-doped silicon.

As shown in Chapter V, however, this theoretical model does not have the same kind of success in describing the Hall mobility and Hall factor for p-type silicon for low dopant densities, and low temperatures. For dopant densities lower than 5×10^{16} cm^{-3}, this model predicts a value of Hall factor much greater than has been experimentally determined [5,15,38]. A discrepancy like this for the case of p-type germanium was eliminated as the quality of germanium crystals improved. Thus it has been assumed that low values of Hall mobility for low-doped p-type germanium at T = 300 K were caused by compensation. However, compensation alone may not account for low values of Hall mobility in the case of p-type silicon [38]. Recent studies by Nakagawa and Zukotynski [77] indicate that the use of the exact model in the development of the Hall factor formulation yields results which agree in general with experimental data for the case of p-type silicon. Experimental data for the case of p-type germanium does not agree with the theoretical results of Nakagawa and Zukotynski [77].

From this study, we have found that the theoretical expressions derived in this work are adequate for mobility and resistivity calculations for p-type silicon in the temperature range $100 \le T \le 400$ K, and the dopant density range $10^{14} \le N_A \le 10^{18}$ cm^{-3}. The theoretical formulation is also adequate for description of the Hall factor and Hall mobility for dopant densities above 5×10^{16} cm^{-3} and temperatures above

200 K. The failure of this model in predicting Hall factor and Hall mobility at low temperatures and dopant densities is due to the omission of the proper anisotropy formulation in the model of the valence band of silicon. This weakness in the model would be remedied by use of the exact model in a manner similar to that of Nakagawa and Zukotynski [11,77].

Further improvements to this model would include the exact formulation of the valence band of silicon on Kane's [27] model, as prescribed by Nakagawa and Zukotynski [11,77]. Thus the proper nonparabolicity and anisotropy would be included. For better comparison with experimental results, the variation of ionization energy with dopant density should be included in the calculation of hole density for the deeper impurities. Also the effects of compensation and the presence of other p-type impurities in silicon samples must be considered. It would also be of great benefit to extend this study into the heavy doped region.

APPENDIX A

FABRICATION PROCEDURES AND TEST STRUCTURES

This appendix contains a list of the fabrication procedures followed to generate the test structures measured in this study. These test structures were part of NBS-4 [67] test pattern, and include a planar four-probe collector resistor, a 100 mil square Hall effect device, a gated base-collector diode, and a gated MOS capacitor over collector structure.

A.1 Initial SiO_2 Masking:

A.1a Initial Clean Up:

(1) Ultrasonic clean in hot DI water with small amount of 100 Tritonex solution for 10 minutes.

(2) Rinse in running DI water for 5 minutes.

(3) Place in solution of $1NH_4OH:1H_2O_2:2H_2O$ for 20 minutes at 50 degrees C.

(4) Rinse in DI water for 5 minutes.

(5) Dip in 10 percent HF for 10 seconds.

(6) Rinse in DI water for 5 minutes.

(7) Place in solution of $1HCl:1H_2O_2:2H_2O$ for 20 minutes at 50 degrees C.

(8) Rinse in DI water for 10 minutes and spin dry in N_2.

A.1b Initial Oxidation - 350 nm at 1100 degrees C

(1) Push-in 5 minutes N_2 at 1000 cc/minute

(2)	Dry O_2	5 minutes	O_2 at 800 cc/minute
(3)	Wet O_2	35 minutes	O_2 at 800 cc/minute
(4)	Dry O_2	5 minutes	O_2 at 800 cc/minute
(5)	N_2	15 minutes	N_2 at 1000 cc/minute
(6)	Pull-out	5 minutes	N_2 at 1000 cc/minute

A.2 Phosphorus Base Diffusion:

A.2a Photoresist (PR) Application with Base Mask (NBS-4-1AB):

(1) Bake at 200 degrees C for 30 minutes to completely dry the wafer.

(2) Apply Waycoat 200 negative PR (do this on both sides of the wafer, apply and spin PR on back side first).

(3) Spin at 5000 RPM for 20 seconds.

(4) Prebake in 65-degree C oven for 20 minutes.

(5) Align wafer and mask and expose for 4 seconds under UV light. (Both sides of the wafer must be exposed.)

(6) Develop for 20 seconds in spray of Waycoat developer (undiluted), then clean off developer with 15-second spray of Butyl Acetate.

(7) Dry with N_2 and inspect under the microscope.

(8) Post bake at 130 degrees C for 25 minutes in N_2 or air circulating oven.

A.2b Base Window Etch:

(1) Etch in buffered HF for 2 minutes, rinse in DI water, dry and inspect. Etch for 15 seconds more to see if the pattern changes color.

(2) When certain that all the oxide has been removed, place wafer in hot (90 degrees C) J-100 PR remover for 5 minutes.

(3) Quench/rinse in methanol for 5 minutes, then rinse with methanol from squirt bottle.

(4) Rinse in DI water for 5 minutes.

(5) Clean up - same as above A.1a except for ultrasonic clean.

A.2c Phosphorus Base Diffusion at 875 degrees C:

(1) Push-in	5 minutes	N_2 at 1250 cc/minute
(2) Phosphorus	16 minutes	N_2 at 1250 cc/minute O_2 at 100 cc/minute N_2 through source bubbler at 10 cc/minute T(source) = 4 to 7 degrees C
(3) Flush-out	2 minutes	O_2 at 800 cc/minute N_2 at 1250 cc/minute
(4) Pull-out	5 minutes	N_2 at 1250 cc/minute

A.2d Removal of Phosphosilicate Glass:

(1) Dip in 10 percent HF for 5 seconds.

(2) Rinse in DI water for 5 minutes and spin dry in N_2.

A.2e Drive-in Diffusion and Base Oxide - 350 nm at 1100 degrees C, base depth approximately 2μm:

(1) Push-in	5 minutes	N_2 at 1000 cc/minute
(2) Dry O_2	10 minutes	O_2 at 800 cc/minute

(3)	Wet O_2	45 minutes	O_2 at 800 cc/minute
(4)	Dry O_2	10 minutes	O_2 at 800 cc/minute
(5)	Drive-in	70 minutes	N_2 at 1000 cc/minute

A.3 Boron Emitter Diffusion:

A.3a PR with Emitter Mask NBS-4-2AB - Same as A.2a (front side PR only), with the following change: Before applying Waycoat PR, coat surface of the wafer with silazane (5 parts Hexamethyldisilizane: 95 parts Xylene), and spin at 4000 RPM for 20 seconds.

A.3b Emitter Window Etch:

(1) Etch in buffered HF for 2.5 minutes, rinse in DI water, dry and inspect. Etch for 15 seconds more to see if the pattern changes color.

(2) When certain that all oxide has been removed (oxide islands must be gone), strip PR and clean up same as A.2b (5).

A.3c Boron Nitride Diffusion at 1050 degrees C:

(1) Load wafers facing source.

(2)	Push-in	5 minutes	N_2 at 500 cc/minute
(3)	Pre-dep	30 minutes	N_2 at 500 cc/minute O_2 at 25 cc/minute
(4)	Oxide	10 minutes	O_2 at 1000 cc/minute
(5)	Pull-out	5 minutes	N_2 at 500 cc/minute

A.3d Removal of Borosilicate Glass:

(1) Dip in 10 percent HF for 10 seconds.

(2) Rinse in DI water for 5 minutes, spin dry in N_2.

A.3e Boron Drive-in and Emitter Oxide, T = 925 degrees C:

(1)	Push-in	5 minutes	N_2 at 1000 cc/minute
(2)	Dry O_2	5 minutes	O_2 at 1000 cc/minute
(3)	Wet O_2	65 minutes	O_2 at 1000 cc/minute
(4)	Dry O_2	5 minutes	O_2 at 1000 cc/minute
(5)	Passivation	5 minutes	N_2 at 1000 cc/minute
(6)	Pull-out	5 minutes	

A.4 Base Contact Diffusion:

A.4a PR with Contact Diffusion Mask NBS-4-5AB - Same as A.2a (PR on both sides - back side first). Back side must be exposed.

A.4b Base Contact Window Etch:

(1) Etch in buffered HF for 2 minutes, 45 seconds. Rinse dry, check for oxide removal.

(2) When all oxide has been removed strip PR and clean up same as A.2b (5).

A.4c Phosphorus Base Contact Diffusion at 875 degrees C:

(1)	Push-in	5 minutes	N_2 at 1250 cc/minute
(2)	Pre-dep	10 minutes	N_2 at 1250 cc/minute O_2 at 100 cc/minute N_2 through source bubbler at 10 cc/minute T(source) = 4 to 7 degrees C
(3)	Flush-out	2 minutes	O_2 at 800 cc/minute N_2 at 1250 cc/minute
(4)	Pull-out	5 minutes	N_2 at 1250 cc/minute

A.4d Removal of Phosphosilicate Glass:

(1) Dip in 10 percent HF for 5 seconds.

(2) Rinse in DI water for 5 minutes and spin dry in N_2.

A.4e Reoxidation at 95 degrees C:

(1)	Push-in	5 minutes	N_2 at 1000 cc/minute
(2)	Dry O_2	10 minutes	O_2 at 1000 cc/minute
(3)	Wet O_2	25 minutes	O_2 at 1000 cc/minute
(4)	Dry O_2	5 minutes	O_2 at 1000 cc/minute
(5)	Passivation	5 minutes	N_2 at 1000 cc/minute
(6)	Pull-out	5 minutes	

A.5 MOS Gate Oxide:

A.5a PR with Gate Oxide Mask NBS-4-6AB - Same as A.2a (PR on front side only, use silizane).

A.5b Etch in Buffered HF for 3 minutes, rinse, dry and check for oxide removal.

A.5c When all oxide has been removed strip PR and clean up same as A.2b (5).

A.5d Gate Oxide Growth - 12000Å at 950 degrees C:

(1)	Push-in	5 minutes	N_2 at 1000 cc/minute
(2)	Dry O_2	10 minutes	O_2 at 800 cc/minute
(3)	Wet O_2	40 minutes	O_2 at 800 cc/minute
(4)	Dry O_2	10 minutes	O_2 at 800 cc/minute
(5)	Passivation	10 minutes	N_2 at 1000 cc/minute
(6)	Pull-out	5 minutes	

A.6 Contact Windows:

A.6a PR with Contact Mask NBS-4-3AB. Same as A.2a (front side only, use silizane).

A.6b Contact Window Etch:

(1) Etch in buffered HF for 3 minutes, check for complete removal of oxide.

(2) Strip PR and clean up same as A.2b.

A.7 Front Side Metallization:

A.7a In the alloy furnace set at 450 degrees C, 5 minutes in N_2; 15 minutes in forming gas, 5 minutes in N_2. Gas flow = 800 cc/minute in all cases.

A.7b Evaporate 800 nm aluminum over the front surface of the wafer.

A.7c PR with Metal Mask NBS-4-4AB. Same as A.2a (front side only, use silizane).

A.7d Etch in Al etchant of 20 H_3PO_4;$5H_2O$:1HN heated to 50 degrees C until the etching is complete (about 2 minutes).

A.7e Rinse in DI water for 10 minutes.

A.7f Strip PR in J-100 and methyl as prescribed in A.2b (3 minutes in 80 degrees C J-100).

A.8 Back Side Contact:

A.8a Dry for 30 minutes in 200-degree C oven.

A.8b Spin PR on front side as prescribed in A.2a (no mask). Expose to U.V. light for 4 seconds.

A.8c Hard bake at 130 degrees C for 30 minutes.

A.8d Dip in 10 percent HF until oxide has been removed from the backside of the wafer.

A.8e Remove PR in J-100 and methyl as prescribed in A.2b (do not use cleaning procedure).

A.8f Scribe the wafer to separate the Hall devices.

A.8g Evaporate 400 nm aluminum over the back side of chips.

A.9 Post Evaporation Micro Alloy. Load chips in alloy furnace at 500 degrees C for 15 minutes. N_2 set for a flow rate of approximately 100 cc/minute.

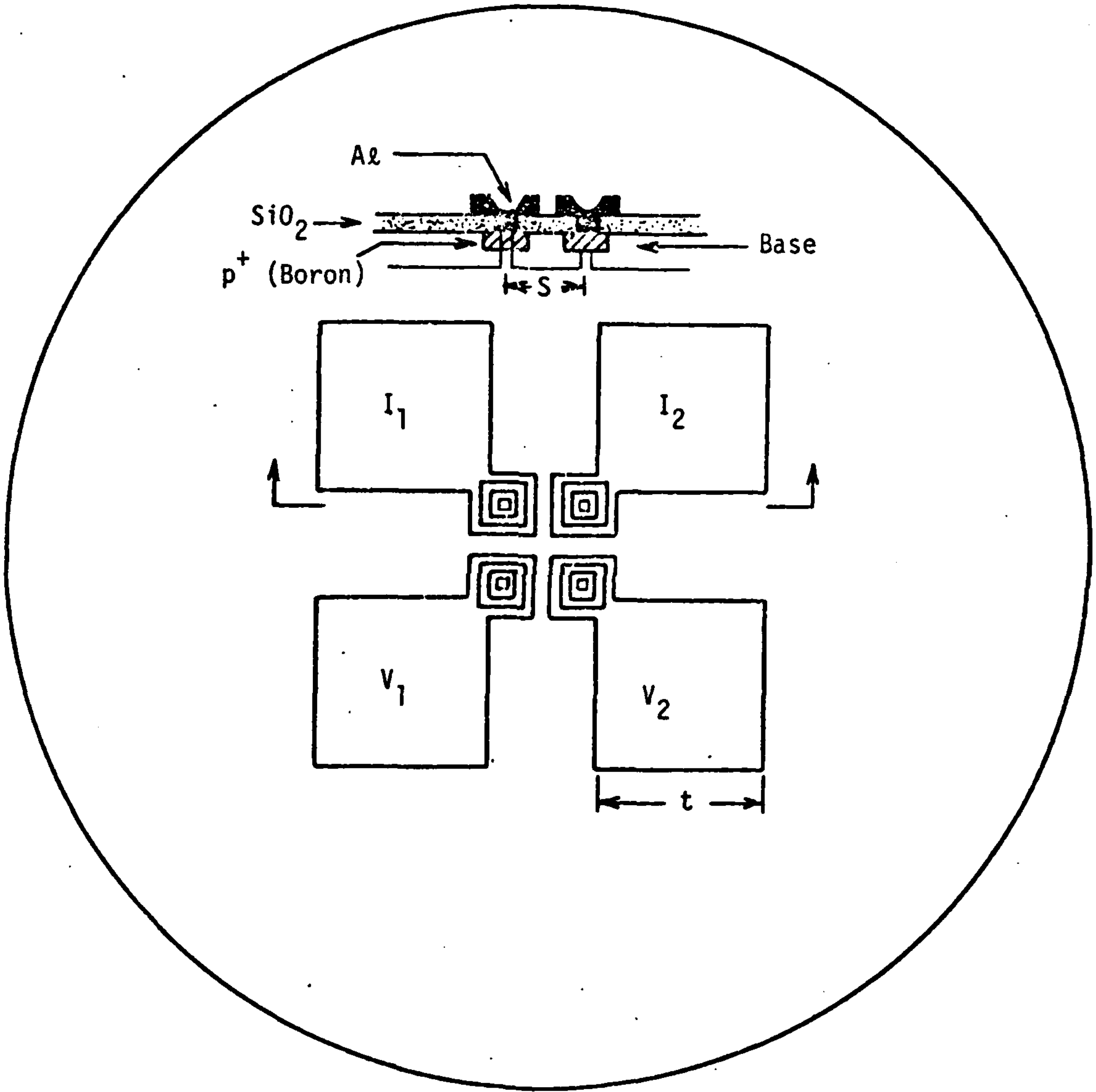

Figure A.1. Square array collector resistor. Pipe size = 0.40x0.40 mil, S = 2.25 mil (57.15 μm), t = 4.75 mil (121 μm), NBS - 4.7 [67].

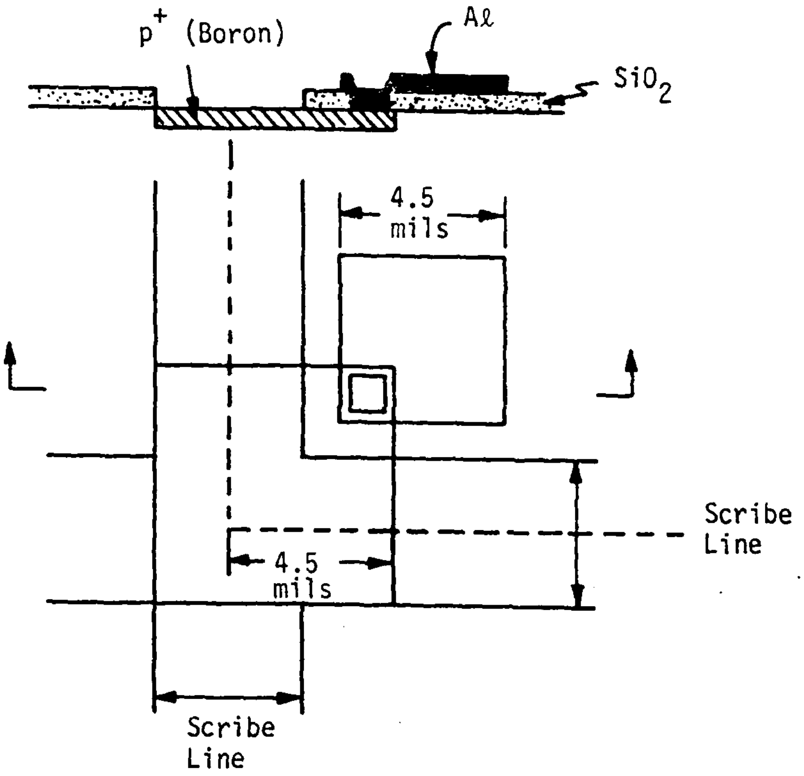

Figure A.2. Hall effect device. NBS - 4.31 [67].

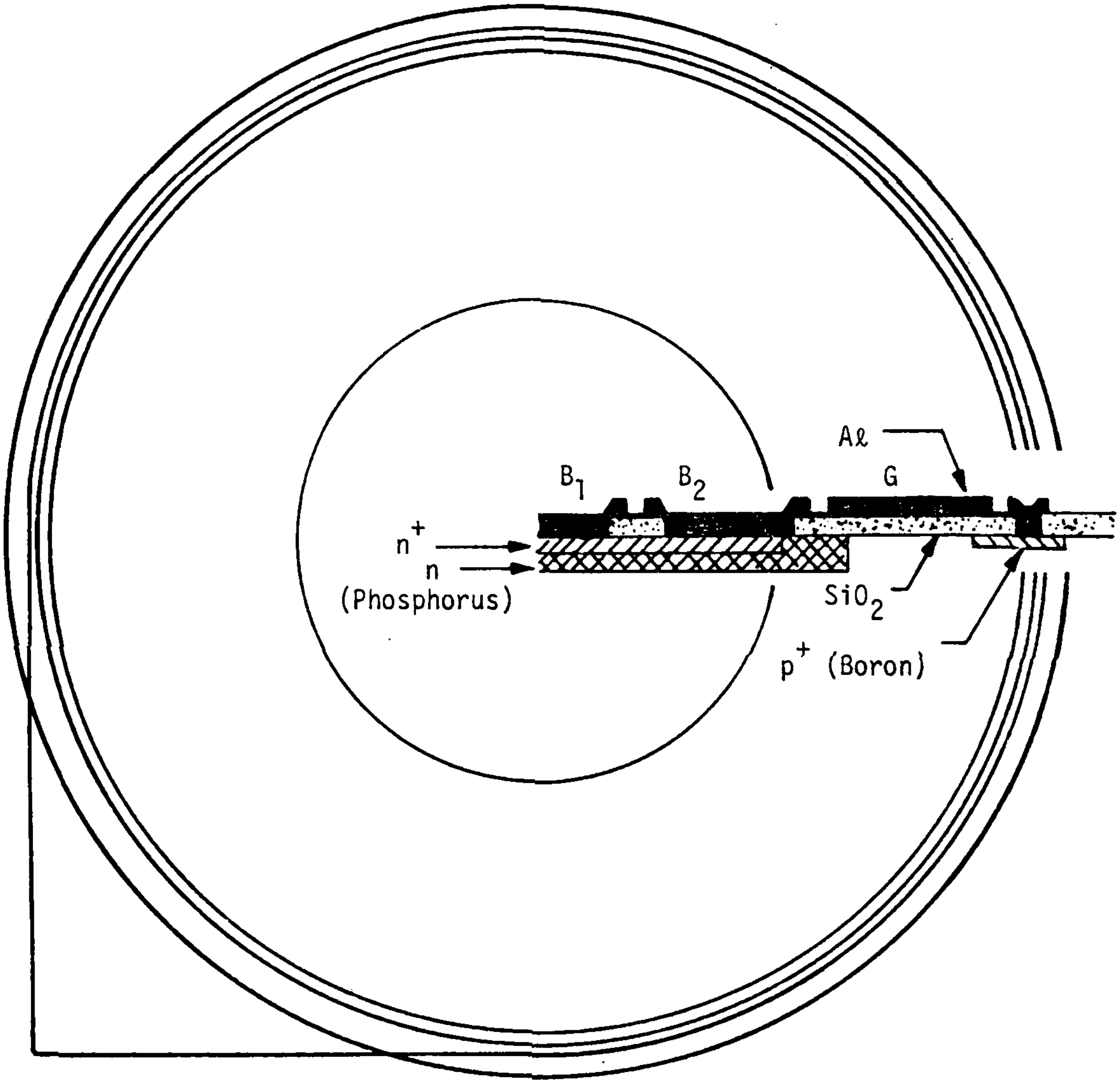

Figure A.3. Gated base-collector diode. Diameter = 17 mils (431.8 μm). NBS - 4.8 [67].

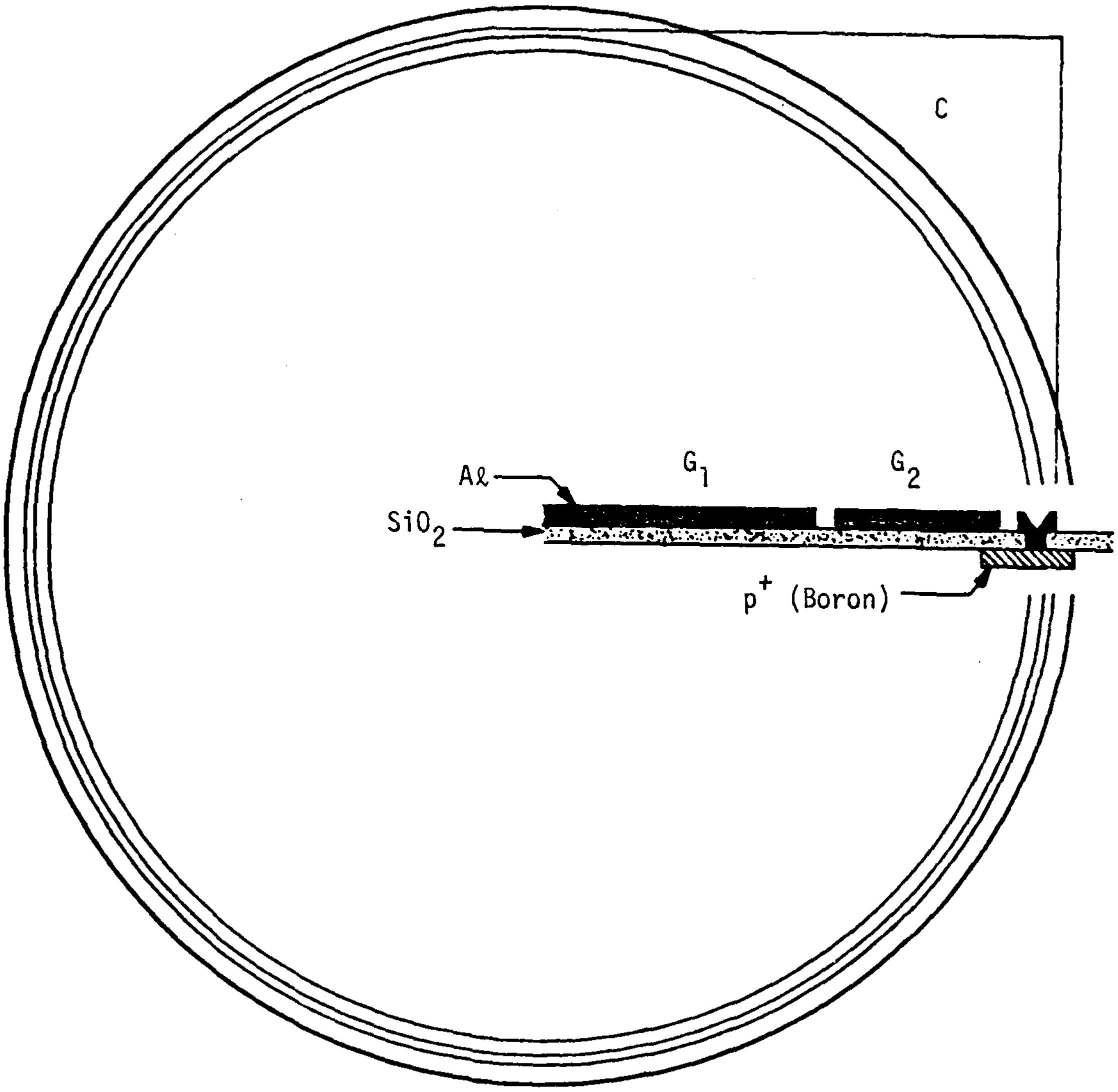

Figure A.4. Gated MOS capacitor over collector. Diameter = 15 mils (381 μm), NBS - 4.8 [67].

APPENDIX B

EXPERIMENTAL SETUP AND DATA

This appendix consists of a block diagram which shows the experimental setup and equipment used, and six tables which show the data taken on the test structures. In addition to measured values of resistivity, dopant density and Hall coefficient, Tables B-1 through B-6 also contain values of calculated Hall mobility.

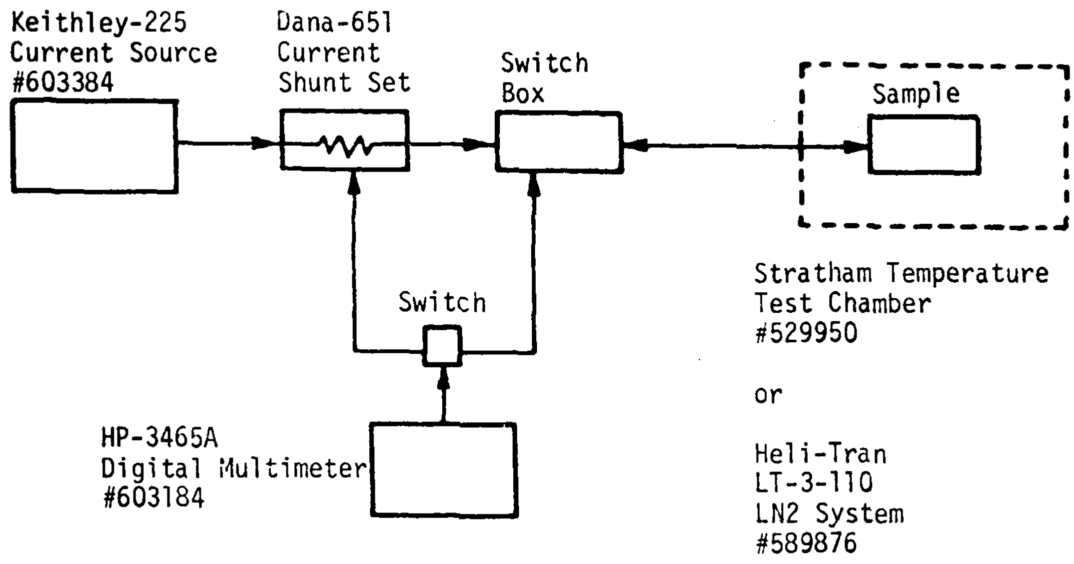

Figure B.1. Experimental Set-up. For Hall effect measurements the magnetic field was generated by a Varian Associates 6 in. Electromagnet System #544772. Capacitance measurements were taken with a Princeton Applied Research-410 C-V Plotter #601922 and a HP-7010A X-Y Recorder #602659.

Table B-1. Sample SGA 16-2 (Ga-Doped Si, $N_A = 4.25\times10^{15}$ cm^{-3})

Temperature T(K)	Resistivity (Ω-cm)	Hall Coefficient R_H(cm^3/coulomb)	Hall Mobility μ_H(cm^2/v-sec)
100	1.700	9381	5518
120	1.185		
140	1.066		
150	1.063	2239	2106
160	1.097		
200	1.434	1443	1006
250	2.230	1433	643
300	3.300	1263	383
350	4.410	1244	282
400	5.580		

Table B-2. Sample SGA 16-3 (Ga-Doped Si, $N_A = 4.09\times10^{16}\ cm^{-3}$)

Temperature T(K)	Resistivity (Ω-cm)	Hall Coefficient $R_H(cm^3/coulomb)$	Hall Mobility $\mu_H(cm^2/v\text{-}sec)$
100	0.660	2325	3523
150	0.308	413	1341
160	0.295		
180	0.286		
190	0.288		
200	0.294	206	701
250	0.361	163	452
300	0.469	149	318
350	0.593	147	248
400	0.735		

Table B-3. Sample SGA 17-2 (Ga-Doped Si, $N_A = 1.26 \times 10^{17}$ cm^{-3})

Temperature T(K)	Resistivity (Ω-cm)	Hall Coefficient R_H(cm^3/coulomb)	Hall Mobility μ_H(cm^2/v-sec)
100	0.464	1019	2196
150	0.204	199	975
180	0.176		
200	0.172	88	512
220	0.175		
250	0.188	65.7	349
300	0.216	57.8	268
350	0.253	52.1	206
400	0.294		

Table B-4. Sample SGA 18-2 (Ga-Doped Si, $N_A = 3.46 \times 10^{17}$ cm^{-3})

Temperature T(K)	Resistivity (Ω-cm)	Hall Coefficient R_H(cm^3/coulomb)	Hall Mobility μ_H(cm^2/v-sec)
100	0.550	605	1100
150	0.163	101	620
200	0.116	46.2	398
230	0.111		
240	0.111		
250	0.112	30.7	274
300	0.121	25.2	208
350	0.135	21.8	161
400	0.152		

Table B-5. Sample SIN 16-2 (In-Doped Si, $N_A = 4.64\times10^{16}$ cm^{-3})

Temperature T(K)	Resistivity (Ω-cm)	Hall Coefficient R_H(cm^3/coulomb)	Hall Mobility μ_H(cm^2/v-sec)
100	21.150	71571	3384
150	4.73	9899	2093
200	1.840	1855	1008
250	1.131	602	532
300	0.916	307	335
350	0.877	207	236
400	0.913		

Table B-6. Sample SIN 17-1 (In-Doped Si, $N_A = 6.44\times10^{16}$ cm^{-3})

Temperature T(K)	Resistivity (Ω-cm)	Hall Coefficient R_H(cm^3/coulomb)	Hall Mobility μ_H(cm^2/v-sec)
100	25.95	58958	2272
150	4.65	7268	1563
200	1.564	1345	860
250	0.952	458	481
300	0.766	237	309
350	0.721	158	219
400	0.740		

APPENDIX C

COMPUTER PROGRAM

This appendix contains the FORTRAN computer program used to generate values of conductivity and Hall effective mass, conductivity and Hall mobility, and Hall factor as functions of temperature and acceptor impurity density in silicon. Besides the main program, two subroutines are also listed. The first of these, DENSTY, calculates the hole density by iterating the Fermi energy level in the charge balance equation as explained in Chapter IV; the second, INTBND, computes the coefficients (functions L_{ij} and T_{ij} of equations (3.7) through (3.9)) used in the calculations of acoustic phonon scattering based on the work of Bir et al [43].

31 MAY 1979

```
10C
20C  CONDUCTIVITY EFFECTIVE MASS, HALL EFFECTIVE MASS,
30C  CONDUCTIVITY MOBILITY, HALL MOBILITY,AND
40C  HALL FACTOR AS FUNCTIONS OF TEMPERATURE AND
45C  ACCEPTOR IMPURITY DENSITY IN SILICON
50C  DOPED WITH BORON
60C
70        REAL MD1,MD2,MD3,MD,NN,NAI,NA,LIM1
80        REAL M1,M2,M3,M1T,M2T,M3T,K,K0,M0,KT
90        REAL MH,MH1,MH2,MH3,MC,MC1,MC2,MC3
100        REAL MOB1,MOB2,MOB3,MOB,MOBH
110        REAL MOBZ
120C
130        DIMENSION CROP(10),PCTG(50),T(10)
140        DIMENSION NN(50),NAI(50),PP(50),NA(50)
150        DIMENSION MD1(10),MD2(10),MD3(10),MD(10)
160C
170        F5(X)=(X-C3)**1.5*EXP(C3-X)
180        F6(X)=X**1.5*EXP(-X)
190        F7(X)=(X-C2)**1.5*EXP(-X)
200C
210        DATA K,A,B,C/8.62E-5,4.27,0.63,4.93/
220        DATA DELTA,M0,K0/0.044,9.10956E-31,1.38062E-23/
230        DATA HBAR,H,PI/1.05459E-34,6.6252E-34,3.14159/
240        DATA E0,ES/8.854185E-12,11.7/
250        DATA TAU0,WW/6.960E-10,0.244/
260        DATA Q/1.60219E-19/
270        DATA THETA,M1,M2,M3/735.0,0.537,0.153,0.234/
280C
290C  READ IN TEMPERATURES AND
300C  DENSITY OF STATES EFFECTIVE MASSES
310C  READ IN THE H-H SCATTERING CORRECTION
315C  FACTOR TO OPTICAL PHONON SCATTERING
320C
330        READ(5,10)(T(J), J=1,10)
340#10      FORMAT(10F6.0)
350        READ(5,11)(MD1(L),L=1,10)
360        READ(5,11)(MD2(L),L=1,10)
370        READ(5,11)(MD3(L),L=1,10)
380        READ(5,11)(MD(L),L=1,10)
390#11      FORMAT(10(F7.5,1X))
400        READ(5,12)(CROP(L),L=1,10)
410#12      FORMAT(10(F6.4,1X))
420C
430C  READ IN DOPANT CONCENTRATIONS
```

31 MAY 1979

```
440C
450         READ (5,13)(NA(L),L=1,40)
460#13       FORMAT(5(E8.2,1X))
470C
480C  COMPUTE F(GAMMA)'S AND ASSOCIATED CONSTANTS
490C  FOR THE DETERMINATION OF EFFECTIVE MASSES
500C
510         BP=SQRT(B**2.+(C**2./6.0))
520         APB=A+BP
525         AMB=A-BP
530         GM=C**2./(2.*BP*AMB)
540         GP=(C**2./(2.*BP*APB))*(-1.)
550         F0M=1.0+.05*GM+.01635*GM**2.+.000908*GM**3.
560         F2M=1.+.01667*GM+.041359*GM**2.+.00090679*GM**3.+
570        1.00091959*GM**4.0+.00002106*GM**5.
580         F2P=1.+.01667*GP+.041359*GP**2+.00090679*GP**3+
590        1.00091959*GP**4+.00002106*GP**5
600         F3M=1.-0.01667*GM+0.017956*GM**2.-
602        &0.0069857*GM**3.+.001261*GM**4
610         F3P=1.-0.01667*GP+0.017956*GP**2
612        &-0.0069857*GP**3+.0012510*GP**4
620C
630C  COMPUTE SCATTERING LIFETIME CONSTANTS
640C
650         TOP11=WW*THETA/TAU0
660         TOP22=TOP11
670         TOP33=TOP11
680         TIA=Q**2./SQRT(M0)
690         TIB=Q**2./(4.0*PI*ES*E0)**2.
700         TIC=TIA*TIB/(K0**1.5*4.50158E-7)
710         GA=7.539822E-5*M0/Q**2.
720         GB=((ES*E0*4.0*PI)/H)*(K0**2./H)
730         GC=GA*GB
740         TNE=1.136E-19/ES**2.
750         TNF=8.88576E6*HBAR**2.0/(M0**1.5*SQRT(K0))
760C
770C  THIS LOOP CHANGES THE TEMPERATURE
780C
790         DO 200 J=1,8
800         KT=K*T(J)
810         C2=DELTA/(3.*KT)
820         C3=DELTA/KT
830         C4=THETA/T(J)
840         C5=C3+C4
850         C6=C3-C4
```

31 MAY 1979

```
860           R8=(MD1(J)/MD(J))**1.5
870           R9=(MD2(J)/MD(J))**1.5
880           R10=(MD3(J)/MD(J))**1.5*EXP(-C3)
890           EG=1.205-2.8E-4*T(J)
900           CROGAP=(1.205/EG)**0.66667
910           M3T=M3*CROGAP
920           WRITE(6.30)
930#30        FORMAT(1H1////8X.'CONDUCTIVITY AND HALL EFFECTIVE
931          &MASS. CONDUCTIVITY AND HALL MOBILITY.'/8X.'AND
940          &HALL FACTOR AS FUNCTIONS OF DOPANT CONCENTRATION.
950          &  BORON DOPED SILICON'///)
960           WRITE(6.40)T(J)
970#40         FORMAT(/40X.'T='.F4.0////)
980C
990C   COMPUTE INTERBAND SCATTERING PARAMETERS
1000C
1010           Y1=MD1(J)
1020           Y2=MD2(J)
1030           CALL INTBND(Y1.Y2.C11.C22.C12.C21.CI12)
1040C
1050C    INTRODUCE TEMPERATURE AND MASS PARAMETERS
1060C    TO THE CALCULATION OF SCATTERING RELAXATION TIMES
1070C
1080           AC11T=(C11/TAU0)*MD1(J)**1.5*T(J)**1.5
1090           AC22T=(C22/TAU0)*MD2(J)**1.5*T(J)**1.5
1100           AC12T=(C12/TAU0)*MD1(J)**1.5*T(J)**1.5*
1101          &(MD2(J)/MD1(J))**2.5
1110           AC21T=(C21/TAU0)*MD2(J)**1.5*T(J)**1.5
1120           TAC33=1.0/TAU0
1130           AC33T=TAC33*T(J)**1.5
1140           PDIST=1./(EXP(C4)-1.)
1150           PDIST1=PDIST+1.
1160           OP11T=TOP11*SQRT(T(J))*MD1(J)**1.5
1170           OP22T =TOP22*SQRT(T(J))*MD2(J)**1.5
1180           OP33T=TOP33*SQRT(T(J))*M3T**1.5
1190           TI11T=TIC/(T(J)**1.5*MD1(J)**0.5)
1200           TI22T =TIC/(T(J)**1.5*MD2(J)**0.5)
1210           TI33T=TIC/(T(J)**1.5*M3T**0.5)
1220           B1T=GC*T(J)**2.*MD1(J)
1230           B2T=GC*T(J)**2.*MD2(J)
1240           B3T=GC*T(J)**2.*M3T
1250           TNG=TNE*MD(J)/(K0*T(J))
1260           TNH1=TNF/(SQRT(T(J))*MD1(J)**1.5)
1270           TNH2=TNF/(SQRT(T(J))*MD2(J)**1.5)
1280           TNH3=TNF/(SQRT(T(J))*MD3(J)**1.5)
```

31 MAY 1979

```
1290C
1300C  COMPUTE SCATTERING LIFETIMES
1310C  THIS LOOP ALSO CHANGES THE CONCENTRATION
1320C
1330       DO 100 L=1,40,2
1340C
1350C  CALL SUBROUTINE TO CALCULATE IONIZED DOPANT DENSITIES
1360C
1370       Q1=T(J)
1380       Q2=NA(L)
1390       Q3=MD(J)
1400       CALL DENSTY(Q1,Q2,Q3,Q4,Q5,Q6,Q7,Q8)
1410       NAI(L)=Q4
1420       PP(L)=Q5
1430       NN(L)=Q6
1440       PCTG(L)=Q7
1450       ETA=Q8
1460C
1470C  COMPUTE CORRECTION FACTORS FOR HOLE-HOLE SCATTERING
1480C
1490       IF(NA(L) .LT. 1.0E15)GO TO 44
1500       IF(NA(L) .LT. 3.0E17)GO TO 46
1510       CRAC=0.88
1520       GO TO 48
1530#44     CRAC=1.0
1540       GO TO 48
1550#46     CRAC=1.0004-(4.013378E-19*NA(L))
1560#48     CRI=(NAI(L)/PP(L))*(1.-EXP(-PP(L)/NAI(L)))
1570C
1580C  INTRODUCE CONCENTRATIONS AND H-H SCATTERING
1581C  CORRECTIONS INTO RELAXATION TIME CALCULATIONS
1600C
1610       AC11S=AC11T/CRAC
1620       AC22S=AC22T/CRAC
1630       AC12S=AC12T/CRAC
1640       AC21S=AC21T/CRAC
1650       AC33S=AC33T/CRAC
1660       OP11S=OP11T/CROP(J)
1670       OP22S =OP22T /CROP(J)
1680       OP33S=OP33T/CROP(J)
1690       G1=B1T/PP(L)
1700       G2=B2T/PP(L)
1710       G3=B3T/PP(L)
1720       GB1=ALOG(G1+1.)-G1/(G1+1.)
1730       GB2=ALOG(G2+1.)-G2/(G2+1.)
```

```
1740        GB3=ALOG(G3+1.)-G3/(G3+1.)
1750        TI11S=TI11T*NAI(L)*GB1/CRI
1760        TI22S =TI22T *NAI(L)*GB2/CRI
1770        TI33S=TI33T*NAI(L)*GB3/CRI
1780        TNI1=TNH1*NN(L)
1790        TNI2=TNH2*NN(L)
1800        TNI3=TNH3*NN(L)
1810C
1820C   COMPUTE AVERAGE RELAXATION TIMES BY SIMPSON'S RULE
1830C   INTEGRATION.  FOR BAND 2, 100 ITERATIONS TO GET TO
1832C   THE 'KNEE' OF THE BAND, AND 200 TO CONTINUE BEYOND
1840C   THE 'KNEE'
1850C
1860        LIM1=0.02/(K*T(J))
1870        END=50
1880        N1=100
1890        N2=200
1900        N3=300
1910        W=LIM1/(2 *N1)
1920        Z=(END-LIM1)/(2 *N2)
1930        SUM1=0.0
1940        SUM2=0.0
1950        SUM3=0.0
1960        SUM4=0.0
1970        SUM5=0.0
1980        SUM6=0.0
1990        SUM8=0.0
2000        SUM9=0.0
2010        SUM10=0.0
2020        SUM11=0.0
2030        SUM12=0.0
2040        SUM13=0.0
2050        SUM19=0.0
2060        SUM20=0.0
2070        SUM23=0.0
2080        TLA33 =0.0
2090        X3=0.0
2100        X4=0.0
2110        X5=0.0
2120        X6=0.0
2130        TI33=0.0
2140        V=0.0
2150C
2160C   SET UP SIMPSON'S RULE INCREMENTS
2170C
```

31 MAY 1979

```
2180        DO 70 KK=1.N3
2190        IF(KK .GT. N1)GO TO 101
2200        GO TO 102
2210#101     XL=V+2.*(KK-N1-1)*Z
2220        XR=V+2.*(KK-N1)*Z
2230        XM=(XL+XR)/2.
2240        W=Z
2250        GO TO 103
2260#102     XL=2.*(KK-1)*W
2270        XR=2.*KK*W
2280        XM=(XL+XR)/2.
2290        IF(KK .EQ. N1)V=XR
2300#103     IF(XL .EQ. 0.0)XL=XM/1000.0
2310        DO 65 JJ=1.3
2320        IF (JJ .EQ. 1) X=XL
2330        IF (JJ .EQ. 2) X=XR
2340        IF (JJ .EQ. 3) X=XM
2350C
2360C  ACOUSTIC PHONON SCATTERING RELAXATION TIMES
2370C
2380        X1 =SQRT(X )
2390        TLA11 =AC11S*X1
2400        TLA12 =AC12S*X1
2410        TLA22 =AC22S*X1
2420        TLA21 =AC21S*X1
2430        TA33 =AC33S*X1
2440        IF(XL .LT. C3)GO TO 54
2450        TLA33 =AC33S*SQRT(X -C3)
2460#54      CONTINUE
2470C
2480C  OPTICAL PHONON SCATTERING RELAXATION TIMES
2490C
2500        IF(XL .LT. C4)GO TO 57
2510        X3 =SQRT(X -C4)
2520#57      X4 =SQRT(X +C4)
2530        TLO11 =OP11S*(PDIST1*X3 +PDIST*X4 )
2540        TL33 =OP33S*(PDIST1*X3 +PDIST*X4 )
2550        IF (XL .LT. C5)GO TO 58
2560        X5 =SQRT(X -C5)
2570#58      IF(XL .LT. C6)GO TO 59
2580        X6 =SQRT(X -C6)
2590#59      TLO33 =OP33S*(PDIST1*X5 +PDIST*X6 )
2600        TLO22=OP22S*(PDIST1*X3+PDIST*X4)
2610C
2620C  IONIZED IMPURITY SCATTERING RELAXATION TIMES
```

31 MAY 1979

```
2630C
2640      X8 =1.0/X **1.5
2650      TI11 =TI11S*X8
2660      TI33P =TI33S*X8
2670      IF(XL .LT. C3)GO TO 63
2680      TI33 =TI33S/(X -C3)**1.5
2690#63    TI22 =TI22S *X8
2700C
2710C  NEUTRAL IMPURITY SCATTERING RELAXATION TIME
2720C
2730      X9=X1+TNG/X1
2740      TN1=TNI1/X9
2750      TN2=TNI2/X9
2760      TN3=TNI3/X9
2770C
2780C  TOTAL RELAXATION TIMES IN EACH BAND
2790C  INTRABAND SCATTERING TIMES
2800C
2810      T1 =1.0/(TLA11 +TLO11 +TI11 +TN1)
2820      T2 =1.0/(TLA22 +TLO22 +TI22 +TN2)
2830      T3 =1.0/(TA33 +TL33 +TI33P +TN3)
2840      TAU3 =1.0/(TLA33 +TLO33 +TI33 +TN3)
2850C
2860      D =1.0-T1 *T2 /(TLA12 *TLA21 )
2870      CR1 =1.0+(T2 *MD1(J))/(TLA12 *MD2(J))
2880      CR2 =1.0+(T1 *MD2(J))/(TLA21 *MD1(J))
2890      TAU1 =CR1 *T1 /D
2900      TAU2 =CR2 *T2 /D
2910      TZ=1.0/(R8/TAU1+R9/TAU2+R10/TAU3)
2920      GO TO (1,2,3),JJ
2930#1     TAU1L=TAU1
2940      TAU2L=TAU2
2950      T3L=T3
2960      TAU3L=TAU3
2970      TZL=TZ
2980      GO TO 4
2990#2     TAU1R=TAU1
3000      TAU2R=TAU2
3010      T3R=T3
3020      TAU3R=TAU3
3030      TZR=TZ
3040      GO TO 4
3050#3     TAU1M=TAU1
3060      TAU2M=TAU2
3070      T3M=T3
```

```
3080         TAU3M=TAU3
3090         TZM=TZ
3100#4        CONTINUE
3110#65       CONTINUE
3120C
3130C   TOTAL LIFETIMES IN EACH BAND SQUARED
3140C
3150         T1SQL=TAU1L**2.0
3160         T1SQM=TAU1M**2.0
3170         T1SQR=TAU1R**2.0
3180         T2SQL=TAU2L**2.0
3190         T2SQM=TAU2M**2.0
3200         T2SQR=TAU2R**2.0
3210         T33SQL=T3L**2.0
3220         T33SQM=T3M**2.0
3230         T33SQR=T3R**2.0
3240         T3SQL=TAU3L**2.0
3250         T3SQM=TAU3M**2.0
3260         T3SQR=TAU3R**2.0
3270         TSQZL=TZL**2.0
3280         TSQZM=TZM**2.0
3290         TSQZR=TZR**2.0
3300C
3310C   SUMMATIONS FOR THE INTEGRALS
3320C
3330         SUM1=SUM1+(W/3.)*(T3L*F6(XL)+4.*T3M*F6(XM)+
3335        &T3R*F6(XR))
3340         SUM3=SUM3+(W/3.)*(TAU2L*F6(XL)+
3345        &4.*TAU2M*F6(XM)+TAU2R*F6(XR))
3350         SUM6=SUM6+(W/3.)*(TAU1L*F6(XL)+
3355        &4.*TAU1M*F6(XM)+TAU1R*F6(XR))
3360         SUM8=SUM8+(W/3.)*(T33SQL*F6(XL)+
3365        &4.*T33SQM*F6(XM)+T33SQR*F6(XR))
3370         SUM10=SUM10+(W/3.)*(T2SQL*F6(XL)+
3375        &4.*T2SQM*F6(XM)+T2SQR*F6(XR))
3380         SUM13=SUM13+(W/3.)*(T1SQL*F6(XL)+
3385        &4.*T1SQM*F6(XM)+T1SQR*F6(XR))
3390         SUM19=SUM19+(W/3.)*(TZL*F6(XL)+
3395        &4.*TZM*F6(XM)+TZR*F6(XR))
3400         SUM20=SUM20+(W/3.)*(TSQZL*F6(XL)+
3405        &4.*TSQZM*F6(XM)+TSQZR*F6(XR))
3410         IF(XL .LT. C3)GO TO 66
3420         SUM2=SUM2+(W/3.)*(TAU3L*F5(XL)+
3425        &4.*TAU3M*F5(XM)+TAU3R*F5(XR))
3430         SUM9=SUM9+(W/3.)*(T3SQL*F5(XL)+
```

```
3435      &4.*T3SQM*F5(XM)+T3SQR*F5(XR))
3440       SUM23=SUM23+(W/3.)*(F5(XL)+4.*F5(XM)+F5(XR))
3450#66     CONTINUE
3460       IF(KK .GT. N1)GO TO 67
3470       SUM4=SUM4+(W/3.)*(TAU2L*F6(XL)+
3475      &4.*TAU2M*F6(XM)+TAU2R*F6(XR))
3480       SUM11=SUM11+(W/3.)*(T2SQL*F6(XL)+
3485      &4.*T2SQM*F6(XM)+T2SQR*F6(XR))
3490       GO TO 68
3500#67     CONTINUE
3510       SUM5=SUM5+(W/3.)*(TAU2L*F7(XL)+
3515      &4.*TAU2M*F7(XM)+TAU2R*F7(XR))
3520       SUM12=SUM12+(W/3.)*(T2SQL*F7(XL)+
3525      &4.*T2SQM*F7(XM)+T2SQR*F7(XR))
3530#68     CONTINUE
3540#70     CONTINUE
3550C
3560C  AVERAGE LIFETIMES
3570C
3580       SUM21=1.32934
3590       TAV1=SUM6/SUM21
3600       TAV2 =SUM3/SUM21
3610       TAV3=SUM2/SUM23
3620       TAVZ=SUM19/SUM21
3630       TSQV1=SUM13/SUM21
3640       TSQV2 =SUM10/SUM21
3650       TSQV3=SUM9/SUM23
3660       TSQVZ=SUM20/SUM21
3670       TRAT1=TSQV1/TAV1**2.0
3680       TRAT2=TSQV2/TAV2**2.0
3690       TRAT3=TSQV3/TAV3**2.0
3700       TRATZ=TSQVZ/TAVZ**2.0
3710C
3720C  THE INTEGRALS HAVE BEEN CALCULATED
3730C  NOW COMPUTE THE MASS
3740C
3750       R2=SUM1/SUM2
3760       R3=SUM3/((F2P*SUM4/SQRT(APB))+
3765      &(F2M*SUM5/SQRT(AMB)))
3770       R5=MD1(J)**1.5/(SQRT(AMB)*F3M)
3780       R6=MD3(J)**1.5*SUM8*EXP(C3)/(SQRT(A)*SUM9)
3790       R7=SUM10/(F3P*SQRT(APB)*SUM11+
3795      $F3M*SQRT(AMB)*SUM12)
3800       MC1=MD1(J)**1.5*SQRT(AMB)/F2M
3810       MC2=MD2(J)**1.5*R3
```

31 MAY 1979

```
3820         MC3=MD3(J)**1.5*SQRT(A)*EXP(C3)*R2
3830         MH1=SQRT(R5)
3840         MH2=SQRT(MD2(J)**1.5*R7)
3850         MH3=SQRT(R6)
3860C
3870C   CALCULATE MC,MH,HALL FACTOR, AND MOBILITY
3880C
3890         R11=TAV1/(TAVZ*MC1)
3900         R12=TAV2/(TAVZ*MC2)
3910         R13=TAV3/(TAVZ*MC3)
3920         R14=TSQV1/(TSQVZ*MH1**2.0)
3930         R15=TSQV2/(TSQVZ*MH2**2.0)
3940         R16=TSQV3/(TSQVZ*MH3**2.0)
3950         MC =1./((R11*R8)+(R12*R9)+(R13*R10))
3960         MH =1./SQRT((R8*R14)+(R9*R15)+(R10*R16))
3970         MOB1=1.0E4*TAV1*Q/(MC1*MO)
3980         MOB2=1.0E4*TAV2 *Q/(MC2*MO)
3990         MOB3=1.0E4*TAV3*Q/(MC3*MO)
4000         MOBZ=1.0E4*TAVZ*Q/(MC*MO)
4010         MOB=R8*MOB1+R9*MOB2+R10*MOB3
4020         RES=1.0/(Q*MOB*NAI(L))
4030         RHZ=TRATZ*(MC/MH)**2.0
4040         MOBH=MOB*RHZ
4240C
4250C   WRITE OUT COMPUTED VALUES OF MOBILITY, MASS
4255C   RESISTIVITY, ETC.
4260C
4270         WRITE(6,85)NA(L),NAI(L),PP(L),NN(L),PCTG(L)
4280#85      FORMAT(5X,'NA=',E10.4,3X,'P=',E10.4,
4285       &3X,'PP=',E10.4,3X,'NN=',E10.4,3X,'NAI/NA=',F6.4/)
4300         WRITE(6,92)MD1(J),MD2(J),MD3(J),MD(J)
4310#92      FORMAT(5X,'MD1=',F7.4,5X,'MD2=',F7.4,5X,
4315       &'MD3=',F7.4,5X,'MD=',F7.4/)
4330         WRITE(6,94)MC1,MC2,MC3,MC
4340#94      FORMAT(5X,'MC1=',F7.4,5X,'MC2=',F7.4,5X,
4350       &'MC3-=,F7.4,5X,'MC=',F7.4/)
4360         WRITE(6,96)MH1,MH2,MH3,MH
4370#96      FORMAT(5X,'MH1=',F7.4,5X,'MH2=',F7.4,5X,
4380       &'MH3=',F7.4,5X,'MH=',F7.4/)
4390         WRITE(6,88)TAV1,TAV2,TAV3,TAVZ
4400#88      FORMAT(5X,'TAV1=',E10.4,5X,'TAV2=',E10.4,5X,
4410       &'TAV3=',E10.4,5X,'TAV=',E10.4/)
4420         WRITE(6,89)TSQV1,TSQV2,TSQV3,TSQVZ
4430#89      FORMAT(5X,'TSQV1=',E10.4,5X,'TSQV2=',E10.4,5X,
4440       &'TSQV3=',E10.4,5X,'TSQV=',E10.4/)
```

31 MAY 1979

```
      WRITE(6,93)TRAT1,TRAT2,TRAT3,TRATZ
#93    FORMAT(5X,'TRAT1=',F6.3,5X,'TRAT2=',F6.3,5X,
     &'TRAT3=',F6.3,5X,'TRATZ=',F6.3/)
      WRITE(6,86)C11,C22,C12,C21
#86     FORMAT(5X,'C11=',F6.3,5X,'C22=',F6.3,5X,'C12=',
     1F6.3,5X,'C21=',F6.3/)
      WRITE(6,98)MOB1,MOB2,MOB3,MOBZ
#98    FORMAT(5X,'MOB1=',F8.2,5X,'MOB2=',F8.2,5X,
     &'MOB3=',F9.2,5X,'MOBZ=',F8.2/)
      WRITE(6,99)MOB,MOBH,RHZ,RES
#99     FORMAT(5X,'COND MOB=',F8.2,3X,'HALL MOB=',F8.2,3X,
     1'HALL FACTOR=',F7.4,3X,'RESISTIVITY=',F8.3///// )
C
C
#100    CONTINUE
#200    CONTINUE
      WRITE(6,300)
#300    FORMAT(1H1)
      STOP
      END
```

31 MAY 1979

```
4790          SUBROUTINE DENSTY (Q1,Q2,Q3,Q4,Q5,Q6,Q7,Q8)
4700C
4710C      SUBROUTINE TO CALCULATE IONIZED AND NEUTRAL
4715C      IMPURITY DENSITY
4720C
4730C      NV=EFFECTIVE DENSITY OF BAND STATES
4740C      EA=DOPANT IONIZATION ENERGY
4750C      NA=DOPANT IMPURITY CONCENTRATION
4760C      EG=ENERGY GAP
4770C      EF=FERMI ENERGY
4780C
4800          REAL NV,NA,K,KT,MD
4810          REAL NAI,NN
4820          DATA K/8.6173E-5/
4830          DATA DELTA/0.044/
4840          T=Q1
4850          NA=Q2
4860          MD=Q3
4870C
4880C      CALCULATE EG,NV,AND EA DIVIDED BY KT
4890C
4900          EG=(((-3.80977E-13*T    +9.95402E-10)*T
4910        --8.701100E-7)*T    +.000032374l)*T    +1.155556
4920          KT=K*T
4930          EAP=(0.0438-3.037E-8*NA**0.3333)/KT
4940          NV=4.82907E15*MD**1.5*T**1.5
4950          ADD=0.0
4960C
4970C      ITERATION TO FIND A VALUE FOR EF SO THAT P=NA-
4980C      IT FINDS EF FOR (P-NA-) < 0.0001
4990C
5000          EF=0.43
5010          DO 12 LI=1,1000
5020          ETA=(EF-EG)/KT
5030          P=NV*EXP(ETA)
5040          IF(ETA .GE. 1.)P=NV*.75225*((ETA**2+1.7)**.75)
5050          NAI=NA/(1.+(4.+2.*EXP(-DELTA/KT)))*EXP(ETA
5055        &+EAP))+ADD
5060          TEST=ABS(P-NAI)
5070          DIF=P/2.
5080          IF(TEST .LE. DIF) GO TO 14
5090          EF=EF+.001
5100#12        CONTINUE
5110          WRITE(6,13)
5120#13        FORMAT(//5X,'WE FELL THROUGH LOOP 0'/)
```

```
31 MAY 1979

      5130#14     EF=EF-.001+.00005
      5140       DO 15 LI=1,400
      5150       ETA=(EF-EG)/KT
      5160       P=NV*EXP(ETA)
      5170       IF(ETA .GE. 1.)P=NV*.75225*((ETA**2+1.7)**.75)
      5180       NAI=NA/(1.+(4.+2.*EXP(-DELTA/KT)))*EXP(ETA+
      5185      &EAP))+ADD
      5190       TEST=ABS(P-NAI)
      5200       DIF=P/10.
      5210       IF(TEST .LE. DIF) GO TO 30
      5220       EF=EF+.0001
      5230#15     CONTINUE
      5240       WRITE(6,20)
      5250#20     FORMAT(//5X,'WE FELL THROUGH LOOP 1'/)
      5260#30     EF=EF-.0001+.00001
      5270       DO 40 LI=1,400
      5280       ETA=(EF-EG)/KT
      5290       P=NV*EXP(ETA)
      5300       IF(ETA .GE. 1.)P=NV*.75225*((ETA**2+1.7)**.75)
      5310       NAI=NA/(1.+(4.+2.*EXP(-DELTA/KT)))*EXP(ETA+
      5315      &EAP))+ADD
      5320       TEST=ABS(P-NAI)
      5330       DIF=P/100.0
      5340       IF(TEST .LE. DIF)GO TO 60
      5350       EF=EF+0.00001
      5360#40     CONTINUE
      5370       WRITE(6,50)
      5380#50     FORMAT(//5X,'WE FELL THROUGH LOOP 2'/)
      5390#60     EF=EF-.00001+.000001
      5400       DO 70 LI=1,500
      5410       ETA=(EF-EG)/KT
      5420       P=NV*EXP(ETA)
      5430       IF(ETA .GE. 1.)P=NV*.75225*((ETA**2+1.7)**.75)
      5440       NAI=NA/(1.+(4.+2.*EXP(-DELTA/KT)))*EXP(ETA+
      5445      &EAP))+ADD
      5450       TEST=ABS(P-NAI)
      5460       DIF=P/1000.
      5470       IF(TEST .LE. DIF )GO TO 90
      5480       EF=EF+0.000001
      5490#70     CONTINUE
      5500       WRITE(6,80)
      5510#80     FORMAT(//5X,'WE FELL THROUGH LOOP 3'/)
      5520#90     ETA=(EF-EG)/KT
      5530C
      5540       PP=NAI+NAI*(1.-NAI/NA)
```

31 MAY 1979

```
5550        NN=ABS(NA-NAI+ADD)
5560        PION=(NAI-ADD)/NA
5570        Q4=NAI
5580        Q5=PP
5590        Q6=NN
5600        Q7=PION
5610        Q8=ETA
5620C
5630        RETURN
5640        END
```

31 MAY 1979

```
5650C
5710        SUBROUTINE INTBND  (Y1.Y2.C11.C22.C12.C21.C112)
5660C
5670C   SUBROUTINE TO CALCULATE INTERBAND RELAXATION TIME
5680C   PARAMETERS FOR ACOUSTICAL PHONON SCATTERING.
5690C   BOTH LONGITUDINAL AND TRANSVERSE VIBRATIONS
5695C   ARE CONSIDERED
5700C
5720        REAL L211.L111.L222.L122.L212
5730C
5740        ETA=0.2125
5750        ETAM=-ETA
5760        ETAS=ETA**2
5770        ETAMS=ETAM**2
5780        G1=SQRT(Y2/Y1)
5790        G2=G1**2.
5800        G3=G1**3.
5810        G4=G1**4.
5820        A=ALOG((1.+G1)/(1.-G1))
5830        BP=(1.+G2)
5840        BPS=(1.+G2)**2.
5850        BMS=(1.-G2)**2.
5860C
5870        P1=(3./(8.*G2))*(1.+G2-(BMS*A)/(2.*G1))
5880        P2=(3./(8.*G4))*((3.*G4-2.*G2+3.)/3.
5884       &-(BP*BMS*A)/(2.*G1))
5890        P3=(3./(4.*G2))*(BP*(15.*G4-22.*G2+15.)/(48.*G4)-
5900       1(1.+(BPS*(5.*G4-14.*G2+5.)/(16.*G4))*A/(2.*G1)))
5910        P4=-BMS*(1.-BP*A/(2.*G1))/(4.*G2)
5920        P5=-BMS*(3.*BP-(3.+2.*G2+3.*G4)*A/(2.*G1))/(4.*G4)
5930C
5940        L211=1.-ETAS-2.*ETA*(1.-ETA)*P1
5945       &+ETA*G2*(2.*(1.+ETA)*P1-3.*ETA*P2)
5950        L111=(1.+ETA)**2 +3.*ETAS/4.
5960        L222=(1.+ETAM)**2.+3.*ETAMS/4.
5970        L122=1.-ETAMS-2.*ETAM*(1.-ETAM)*P1+
5980       1ETAM*G2*(2.*(1.+ETAM)*P1-3.*ETAM*P2)
5990        L212=-ETA*(1.-ETA)*P2+G2*ETA*((1.+ETA)*P2
5995       &-3.*ETA*P3)
6000C
6010        T111=0.75
6020        T222=0.75
6030        T122=9.*(1.-P4)/4.
6040        T211=T122
6050        T212=-9.*P5/16.
```

31 MAY 1979

```
6060C
6070        C11=L222+G3*L122+2.09*ETAS*(T222+G3*T122)
6080        C22=L211+G3*L111+2.09*ETAS*(T211
6085       &+G3*T111)*(Y1**1.5/Y2**1.5)
6090        C12=L212+2.09*ETAS*T212*(Y1**1.5/Y2**1.3)
6100        C21=L212+2.09*ETAS*T212
6110C
6120        P7=3.*G1*P5/(1.-G2)**2.
6130        CI12=P7
6140C
6150        RETURN
6160        END
```

REFERENCES

1. T. T. Braggins, Ph.D. Dissertation (Syracuse University, 1975).
2. J. C. Irvin, Bell Sys. Tech. J., 16, 387 (1962).
3. S. M. Sze and J. C. Irvin, Solid State Electronics, 11, 599 (1968).
4. M. Costato and L. Reggiani, Il Nuovo Cimento, 68, 64 (1970).
5. F. J. Morin and J. P. Maita, Phys. Rev., 96, 28 (1954).
6. M. Prince, Phys. Rev., 93, 1204 (1954).
7. G. W. Ludwig and R. L. Watters, Phys. Rev., 101, 1699 (1956).
8. S. Wagner, J. Electrochem. Soc., 119, 1570 (1972).
9. G. L. Pearson and J. Bardeen, Phys. Rev., 75, 865 (1949).
10. M. Asche and J. Von Borzeszkowshi, Phys. Stat. Sol., 37, 433 (1970).
11. H. Nakagawa and S. Zukotynski, Can. J. Phys., 55, 1485 (1977).
12. W. R. Thurber, R. L. Mathis and Y. M. Liu, Proceedings of the ECS, 78-3, 81 (1978).
13. F. W. Horn, Phys. Rev., 97, 1521 (1955).
14. N. Sclar, IEEE Trans. Electron Devices, ED-24, 709 (1977).
15. K. B. Wolfstirn, J. Phys. Chem. Solids, 16, 279 (1960).
16. G. Backenstoss, Phys. Rev., 108, 1416 (1957).
17. S. S. Li, Solid State Electronics, 21, 1109 (1978).
18. J. M. Radcliffe, Proc. Phys. Soc. London, A68, 675 (1955).
19. R. Barrie, Proc. Phys. Soc. London, B69, 553 (1956).
20. B. Lax and J. G. Mavroides, Phys. Rev., 101, 1650 (1955).
21. M. Cardona, W. Paul and H. Brooks, Helv. Phys. Acta, 33, 329 (1960).
22. J. C. Hensel and G. Feher, Phys. Rev., 129, 1041 (1963).

23. D. B. Armstrong and K. S. Champlin, J. Appl. Phys., 37, 911 (1966).

24. J. I. Nathan, W. Paul, and H. Brooks, Am. Phys. Soc. Bull., 3, 14 (1958).

25. H. D. Barber, Solid State Electronics, 10, 1039 (1967).

26. M. Costato and E. Reggiani, Lettere al Nuovo Cimento, 3, 239 (1970).

27. E. O. Kane, J. Phys. Chem. Solids, 1, 82 (1956).

28. G. Dresselhaus, A. F. Kip, and C. Kittel, Phys. Rev., 95, 568 (1954).

29. I. Balslev and P. Lewaetz, Physics Letters, 19, 6 (1965).

30. J. D. Wiley, Semiconductors and Semimetals, R. K. Willardson and A. C. Beer, Ed., 10, 91 (Academic Press, New York, 1975).

31. M. Cardona and F. H. Pollak, Phys. Rev., 142, 530 (1966).

32. S. Zwerdling, K. J. Button, B. Lax, and L. M. Roth, Phys. Rev. Lett., 4, 173 (1960).

33. G. Gagliani and L. Reggiani, Il Nuovo Cimento, 30, 207 (1975).

34. H. Miyazawa, K. Suzuki and H. Maeda, Phys. Rev., 131, 2442 (1963).

35. I. Balslev, Phys. Rev., 143, 636 (1966).

36. E. Adler and E. Erlbach, Phys. Rev. Letters, 16, 87 (1966).

37. K. Seeger, Semiconductor Physics (Springer-Verlag, New York, 1973).

38. D. Long, Phys. Rev., 107, 672 (1957).

39. D. Geist, Naturwissenschaften, 45, 33 (1958).

40. P. H. Keeson and G. Seidel, Phys. Rev., 113, 33 (1959).

41. P. Hauge, Ph.D. Dissertation (The University of Minnesota, 1967).

42. R. H. Bube, Electronic Properties of Crystalline Solids (Academic Press, New York, 1974).

43. G. H. Bir, E. Normantas, and G. E. Pikus, Soviet Phys. Solid State, 4, 867 (1962).

44. G. E. Pikus and G. H. Bir, Soviet Phys. Solid State, 1, 136 (1959).

45. H. Ehrenreich and A. W. Overhauser, Phys. Rev., 104, 649 (1956).

46. E. M. Conwell, J. Phys. Chem. Solids, 8, 234 (1959).

47. E. M. Conwell and V. F. Weisskopf, *Phys. Rev.*, 77, 388 (1950).

48. H. Brooks, *Advances in Electronics and Electron Physics*, L. Marton, Ed., 7, 85 (Academic Press, New York, 1955).

49. C. Herring, *Bell Syst. Tech. J.*, 36, 237 (1955).

50. C. Erginsoy, *Phys. Rev.*, 104, 1559 (1956).

51. N. Sclar, *Phys. Rev.*, 104, 1548 (1956).

52. N. Sclar, Phys. Rev., 104, 1559 (1956).

53. S. S. Li, *NBS Special Publication*, 400-33, March (1977).

54. R. W. Keyes, *J. Phys. Chem. Solids*, 6, 1 (1958).

55. M. Luong and A. W. Shaw, *Phys. Rev.*, B4, 2436 (1971).

56. J. S. Blakemore, *Semiconductor Statistics* (Pergamon Press, New York, 1962).

57. N. A. Penin, B. G. Zhurkin, and B. A. Volkov, *Sov. Phys. Solid State*, 7, 2580 (1966).

58. W. Scott, Presented at IRIS Specialty Group on IR Detectors, Colorado Springs, CO, 21-23 March 1977.

59. F. J. Blatt, *Physics of Electronic Conduction in Solids* (McGraw-Hill, New York, 1968).

60. R. Willardson, T. Harman, and A. Beer, *Phys. Rev.*, 96, 1512 (1954).

61. J. Swanson, *Phys. Rev.*, 99, 1799 (1955).

62. Y. Yafet, R. W. Keyes, and E. N. Adams, *J. Phys. Chem. Solids*, 1, 137 (1956).

63. P. P. Debye and T. Kohane, *Phys. Rev.*, 724, (1954).

64. D. K. Schroder, T. T. Braggins, and H. M. Hobgood, *J. Appl. Phys.*, 49, 5256 (1978).

65. E. H. Putley, *The Hall Effect and Related Phenomena* (Butterworth Scientific Publications, London, 1960).

66. E. H. Putley, *The Hall Effect and Semiconductor Physics* (Dover, London, 1968).

67. W. R. Thurber and M. G. Buehler, *NBS Special Publication*, 400-32, (April, 1978).

68. M. G. Buehler, *NBS Special Publications*, 400-22 (June, 1976).

69. A. Uhlir, Jr., Bell Syst. Tech. J., 34, 105 (1955).

70. M. Buehler and W. R. Thurber, IEEE Trans. Electron Devices, ED-23, 968 (1976).

71. L. J. van der Pauw, Philips Research Reports, 13, 1 (1958).

72. ASTM Method F76, Annual Book of ASTM Standards, Part 43 (November, 1977).

73. W. van Gelder and E. H. Nicollian, J. Electrochem. Soc.: Solid State Science, 118, 138 (1971).

74. A. S. Grove, Physics and Technology of Semiconductor Devices (John Wiley and Sons, New York, 1967).

75. W. R. Thurber and B. S. Carpenter, J. Electrochem. Soc., 125, 654 (1978).

76. M. Green, Bull. Am. Phys. Soc. Ser. II, 2, 158, (1957).

77. H. Nakagawa and S. Zukotynski, Can. J. Phys., 56, 364 (1978).

BIOGRAPHICAL SKETCH

Luis Carlos Linares was born August 1944 in Bogota, Colombia, and became a United States citizen on December 18, 1964. Raised in Miami, Florida, he attended Miami Central High School, and Miami-Dade Junior College. He received the degree of Bachelor of Science in Electrical Engineering in June 1969, and the degree of Master of Science in Electrical Engineering in December 1970, both from the University of Florida. In March 1971 he entered active service with the United States Air Force and worked until May 1975 as a Computer System Analyst for the Strategic Air Command at Offutt AFB, Nebraska. In June 1975 he was selected by the Air Force Institute of Technology to attend the University of Florida and work toward the degree of Doctor of Philosophy. He is presently a captain in the Air Force, working as an Advanced Communications Requirements Officer, stationed at Scott AFB, Illinois.

Luis Carlos Linares is a member of Eta Kappa Nu and the Institute of Electrical and Electronics Engineers. He is married to the former Diane Hermann, and has three sons, Luis Carlos Jr., John Michael, and Christopher Lee.

I certify that I have read this study and that in my opinion it conforms to acceptable standards of scholarly presentation and is fully adequate, in scope and quality, as a dissertation for the degree of Doctor of Philosophy.

Sheng San Li

Sheng-San Li, Chairman
Professor of
Electrical Engineering

I certify that I have read this study and that in my opinion it conforms to acceptable standards of scholarly presentation and is fully adequate, in scope and quality, as a dissertation for the degree of Doctor of Philosophy.

FA Lindholm

Fredrik A. Lindholm
Professor of
Electrical Engineering

I certify that I have read this study and that in my opinion it conforms to acceptable standards of scholarly presentation and is fully adequate, in scope and quality, as a dissertation for the degree of Doctor of Philosophy.

Ulrich H. Kurzweg

Ulrich H. Kurzweg
Professor of
Engineering Sciences

This dissertation was submitted to the Graduate Faculty of the College of Engineering and to the Graduate Council, and was accepted as partial fulfillment of the requirements for the degree of Doctor of Philosophy.

August 1979

Dean, College of Engineering

Dean, Graduate School

FILMED

2-8